PORTUGALIAE PHYSICA

VOLUME 18
FASCÍCULO 1-2
1987

SOCIEDADE PORTUGUESA DE FÍSICA

PORTUGALIAE PHYSICA

Fundada em 1943 por A. Cyrillo Soares, M. Telles Antunes, A. Marques da Silva e M. Valadares

Publicação subsidiada pelo INSTITUTO NACIONAL DE INVESTIGAÇÃO CIENTÍFICA

ISSN 0048 - 4903

PORTUGALIAE PHYSICA

VOLUME 18
FASCÍCULO 1-2
1987

LETTER FROM THE EDITOR

Prof. J. Araújo has ceased to be the Editor of Portugaliae Physica to which he has devoted himself with intelligence and great expertise. All of his colleagues have tried to dissuade him from leaving the editorship but more recent duties made it impossible for him to continue.

The Portuguese Physical Society and the new Editor would like to testify their great appreciation to Prof. J. Araújo and wish him all the success as Chairman of the Publications Committee of the European Physical Society.

K_α X-RAY SATELLITES EXCITED BY PHOTONS IN S AND ITS COMPOUNDS

M. V. R. MURTI and K. S. RAO

Centre of Studies in Resources Engineering, Indian Institute of Technology
Bombay 400 076, India

V. GOPALAKRISHNA, M. L. N. RAJU and K. PARTHASARADHI

Departament of Nuclear Physics, Andhra University
Visakhapatnam 530 003, India

V. RADHA KRISHNA MURTY

Department of Engineering Physics, Andhra University
Visakhapatnam 530 003, India

(Received 14 November 1986, revised version 22 May 1987

ABSTRACT — The K_α X-ray satellite spectra of S and some of its compounds, excited by Rh tube X-rays, are studied with a plane crystal spectrometer. The $K_\alpha L^1 / K_\alpha L^0$ intensity ratios based on the assumption of a free Ne core are found to be somewhat higher than our experimental values.

1 — INTRODUCTION

Studies on K_α X-ray satellites arising from single K plus multiple L vacancy states have been a subject of much experimental and theoretical interest. The absence of L shell electrons in addition to one K electron reduces the screening of the nuclear potential felt by the remaining electrons and increases their binding energies. A K_α X-ray emitted from such a state will be at a higher energy than the normal diagram or $K_{\alpha 1\,\alpha 2}$ X-ray line (i. e. K_α X-rays emitted when there are no holes in the L shell). Depending on the number (n) of L shell vacancies, the emitted K_α X-ray multiplets are designated $K_\alpha L^n$ satellites. Correspondly, the X-rays emitted in the absence of one, two, three, etc, L electrons in addition to one K electron are designated as $K_\alpha L^1$, $K_\alpha L^2$,

K_α L^3, etc. satellite groups, respectively, and the ordinary X-ray, which is emitted when there are no L vacancies, is designated as $K_\alpha L^0$. Most of the studies on satellites have been carried out using heavy-ion excitation [1]. However, the first one or two satelites can be studied [2]-[7] by electron or photon excitation. But not much experimental data of satellite relative intensities are available for $Z > 14$ in the case of photon excitation. In the present investigation, an attempt has been made in this direction: K_α X-ray satellites in S and some of its compounds have been studied by photon excitation.

2 – EXPERIMENT

The general experimental setup and the principle of measurement are the same as those reported previously [3]-[7] for photon

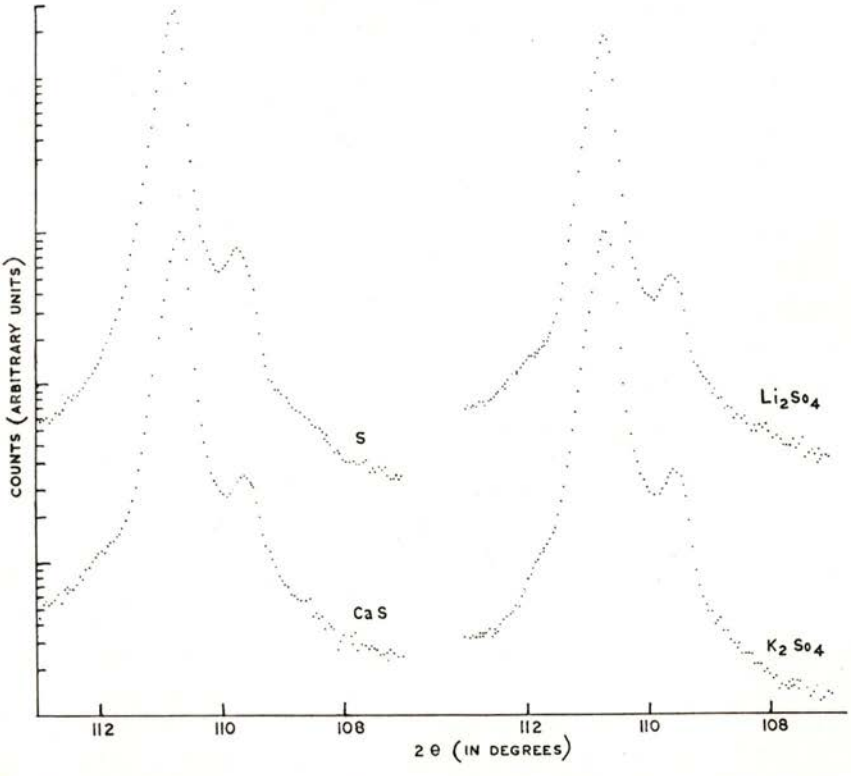

K_α X-ray Satellite Spectra in S and some compounds, excited by photons.

excitation. In the present investigation, a Philips 1410 wavelength dispersive spectrometer is used. This, in brief, consists of a Rh X-ray tube, a plane crystal spectrometer and a continuous P-10 (90 % Argon and 10 % methane) gas flow proportional counter. The X-ray tube is operated at 40 kV and 40 mA. Two fine collimators (0.01°), one at the target and the other at the detector are used. Pure powders of S, Li_2SO_4, K_2SO_4 and CaS pressed into pellets 5 mm thick and 50 mm in diameter are used. The spectra are scanned in 2θ steps of 0.05°, with a Ge (111) [2d = 6.532 Å] plane crystal. Typical K_α X-ray satellite spectra of S and its compounds are shown in Fig. 1.

3 – RESULTS AND DISCUSSION

It can be seen from the figure that the spectra exhibit two distinct groups, the diagram line ($K_\alpha L^0$) and the first satellite ($K_\alpha L^1$), in all cases. The spectra are analysed by fitting the groups individually on a computer and the intensity ratios $K_\alpha L^1 / K_\alpha L^0$ are estimated in each case. These ratios are then corrected for i) crystal reflectivity, ii) self absorption in the target, iii) absorption in the detector window and iv) efficiency of the detector. Since the energy difference between the $K_\alpha L^1$ and $K_\alpha L^0$ groups is small, the relative total correction due to the above factors is small. The experimental procedure is repeated in each case for six trials and the average values of the intensities are estimated. The error associated with the ratios mainly include the statistical error.

The estimated $K_\alpha L^1 / K_\alpha L^0$ ratios, together with the ratios measured by electron excitation [5], [6] and the theoretical value of Aberg [2] are given in Table 1. The theory of Aberg [2] is based on the sudden approximation (shake-off). This theory is formulated on the assumption that the formation of an inner hole occurs so quickly that a rapid change in the Coulomb field experienced by the electrons (other than photoelectrons) gives rise to anomalous states, i. e. excitation of a double hole state occurs independently of the excitation mode. In that case, the K_α satellite relative intensities should be same in both X-ray and electron excitation modes. Thus Aberg [2] reported $K_\alpha L^1 / K_\alpha L^0$

ratios for Ne like atoms from F to Ca. The values of the ratio for S and one typical gaseous compound (H_2S) are also given in Table 1. It can be seen from the table that Aberg's theoretical ratio as well as the electron excitation ratios of Baun and Fischer are definitely higher than our experimental values. It is evident from the table that the heavy-ion excitation value of the ratios are very much higher than the present value or the experimental value of Baun and Fischer. This is probably due to the increase

TABLE 1 — $K_\alpha L^1 / K_\alpha L^0$ Intensity Ratios (in percent)

Material	Present work (Photon Excitation)	Baun & Fischer (Electron Excitation)	Parrat (Electron Excitation)	Demarest et al. (Heavy-ion Excitation)	Aberg (Theory)
S	4.6 ± 0.4	5.6 ± 0.4*	4.8	311.4	5.7
K_2SO_4	4.5 ± 0.4	—	—	—	—
CaS	4.5 ± 0.4	—	—	—	—
Li_2SO_4	4.8 ± 0.4	—	—	—	—
H_2S	—	—	—	527.3	—

* Value taken Ref. [2].

of the multiple ionization probability for L shell in the case of heavy-ion excitation; in such a case the sudden approximation theory is no longer valid. The higher value in the case of the gaseous compound (H_2S) may be attributed to the decrease of the electron rearrangement probability by the electron transfer process which is possible in view of the larger interatomic or molecular distances in gases.

The authors are thankful to Professor R. K. Katti, Head, Centre of Studies in Resources Engineering, Indian Institute of Technology, Bombay, India for providing the experimental facilities and for his encouragement.

REFERENCES

[1] DEMAREST, J. A. and WATSON, R. L., *Phys. Rev.*, **17A**, 1302 (1978).

[2] ABERG, T., *Phys. Letts.*, **26A**, 515 (1968).

[3] UTRIAINEN, J., LINKOAHO, M., ABERG, T. and GRAEFFE, G., *Z Naturf.*, **23A**, 1178 (1968).

[4] MIKKOLA, E., KESKI-RAHKONEN, O., LATINEN, J. and REINKAINEN, R., *Physica Scripta*, **28**, 188 (1983).

[5] PARRAT, L. G., *Phys. Rev.*, **50**, 1 (1936).

[6] FISCHER, D. W., and BAUN, W. L., *Spectrochimica Acta*, **21**, 443 (1965); *J. Appl. Phys.*, **36**, 534 (1965); *J. Chem. Phys.*, **42**, 3614 (1965).

[7] RAMESH BABU, G., PARTHASARADHI, K., RADHA KRISHNA MURTY, V., MURTI, M. V. R. and RAO, K. S., *Physica*, **138C**, 201 (1986).

ELECTRICAL BEHAVIOUR OF THE CERAMIC γ-AlON

A. R. FERREIRA, J. M. PERDIGÃO

Centro de Electrotecnia da Universidade de Coimbra (L3 — INIC)
Largo Marquês de Pombal — 3000 Coimbra

(Received 16 January 1987; revised version 22 June 1987)

ABSTRACT — In this paper some measurements on the impedance of aluminium oxynitride samples, using a Fourier technique, are presented and discussed.

1 — INTRODUCTION

A solid electrolyte is a real crystal showing defects like its surface, dislocations or point defects [1-3].

Usually, a solid electrolyte is presented as a material where the electrical conductivity is mainly assured by the ions [4]. In many solid electrolytes a single species is responsible for the electric current; among its most important features one might mention an electric conductivity lower than in metals or semiconductors, an exponential temperature dependence, no convection problems and a temperature-dependent defect concentration [5].

Ionic mobility may be derived from measured impedance spectra; in solid electrolytes this is more convenient than conventional electrochemical methods. Due to inhomogeneities, a solid electrolyte may show a frequency-dependent impedance behaviour with two main contributions: one corresponding to polarization effects inside the grain and the other to a conduction blocking effect at the grain junction. Care must be taken in the choice of the measuring technique in order to evaluate the different contributions involved (bulk and stray ones).

2 – EXPERIMENTAL METHOD AND RESULTS

2.1 – *Measurement technique*

The impedance spectrum $Z(\omega)$ is obtained by sweeping the frequency of the applied electrical potential; for solid electrolytes, one often uses the range 1-100 kHz.

Solid electrolytes appear mainly as compressed powders, ceramics, or solidified melts; their bulk conductivity can not be considered equivalent to a single resistor [6].

The measured current depends on the sample impedance but is also affected by a number of other contributions:

– the electrode/electrolyte interfacial impedances
– the measuring leads impedance
– the empty cell impedance

The electrical behaviour of the solid cell is due to the overall bulk (grain and intergrain) contribution of the sample and the interfacial sample/electrode contribution. This may be described using a series or parallel arrangement of different RC circuits [7-9].

A considerable number of electrical measuring techniques may be used for experimental characterization of the sample [10-12]. However, a Fourier technique allows a rapid analysis by means of the extended frequency spectrum of a d. c. pulsed regime as well as a better elimination of the noise from the measured signal.

In the Fourier technique, which we have employed, instead of scanning the impedance spectrum of a solid cell by using one frequency at a time, a square wave or a train of pulses is used. Pulsed measurements are performed either by imposing the current and measuring the potential difference across the sample (or vice versa) providing the same information with a better elimination of the noise. The data are collected by means of a transient recorder (see Fig. 1). This is a gated device, Solatron Model 1170; it generates an output signal with a frequency lying within the range 10^{-4} - 10^{6} Hz and measures the incoming voltage signal, the potential difference across the sample, during a triggering time Δt. The averaged values are analog/digital converted and stored in a microprocessor. By triggering at the start

of each new pulse (or each new wave) and adding the signal response of a large number of wave periods, the noise effects are averaged out.

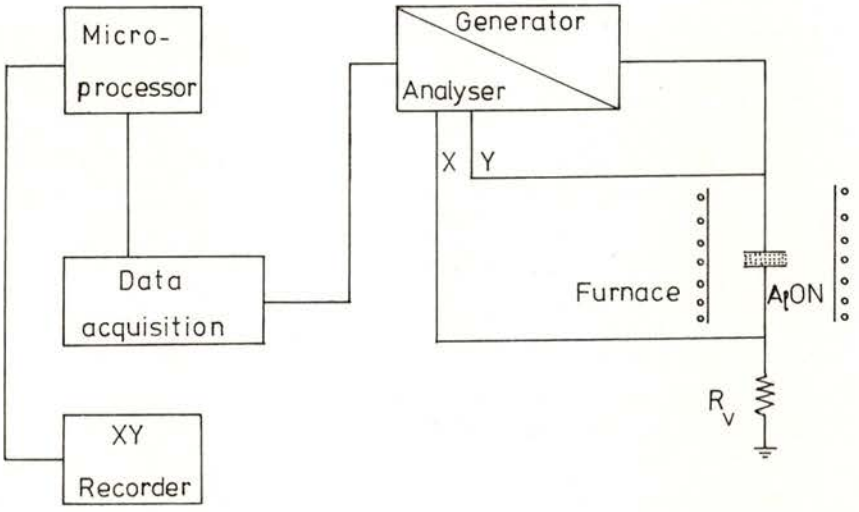

Fig. 1 — Measuring system

The system response is processed using the Fourier technique by an Hewlett Packard microprocessor H80. The results are presented in terms of X/Y ratio with $Z = (Y/X - 1)\ R_v$, where R_v is a calibrated resistance.

A tubular furnace, with two different thermocouples (one close to the heating elements and the other to the sample), is used. The samples are placed inside an aluminium oxyde chamber filled with N_2 gas. To prevent contamination, the chamber is previously pumped down to a vacuum better than 10^{-4} torr.

2.2 — *Experimental results*

2.2.1 — Sample preparation

The AlON used is obtained by alumina nitration in the presence of carbon (carbon black). The first step leads to the formation of aluminium nitride AlN

$$Al_2O_3 + N_2 + 3\ C \rightarrow 2\ AlN + 3\ CO\ ;$$

this, in a second step, reacts with the alumina excess and originates the AlON :

$$Al_2O_3 + AlN \rightarrow AlON$$

This reaction is non-stoichiometric and once the involved component ratios are deffined, the reaction will proceed until total decay of the alumina [13-14].

The powder of AlON obtained by the described process, with an average size of 6 μm, is then hot-pressed at 40 MPa for 4 hours at 1800°C; afterwards it is submitted to a grain growith thermal treatment in a N_2 atmosphere (24 hours, 1950°C).

2.2.2 – Impedance spectrum

The experimental results are shown in Fig. 2. We can see that the impedance spectrum includes a single contribution, in this case [7-9] the one due to the microstructure of the sample.

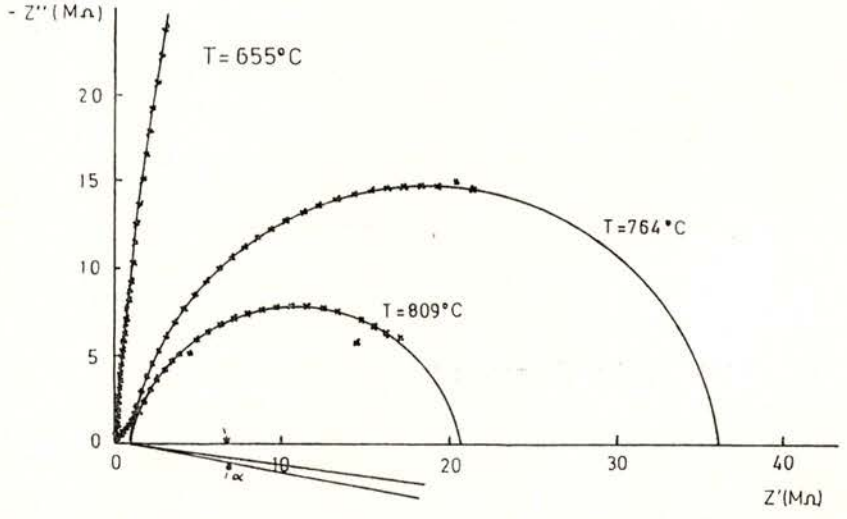

Fig. 2 — Experimental results obtained using the temperature as a parameter

The dielectric behaviour of the AlON sample, with a relative dielectric constant, ε_r, equal to 10-13 and a loss tangent, tgδ, in the range 0.01-0.03 can be obtained from an equivalent circuit like the one shown in Fig. 3. There the r C parallel arrangement (r = 20-40 MΩ represents the intergranular resistance and

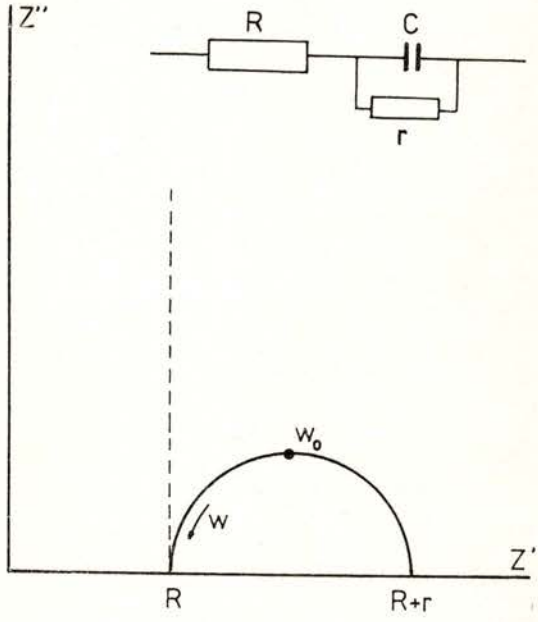

Fig. 3 — Simplified equivalent circuit for an AlON sample

C = 20-35 pF represents a double layer capacitance corresponding to the polarization effects at the grain junction) characterizes the intergranular zone and R = 1 MΩ the bulk (grain) contribution.

2.2.3 – Activation energy

From the Arrhénius representation of Fig. 4 we infer that the sample shows a poor conductivity, even at high temperatures, which is confirmed by the large value of the activation energy. An activation energy, E_a, equal to 1.27 eV, was obtained and

this value agrees well with other experimental values in the literature [15].

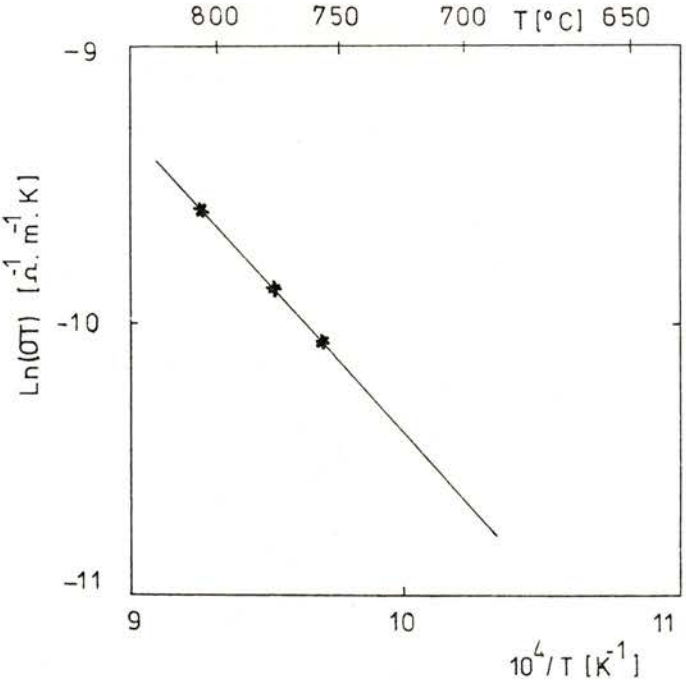

Fig. 4 — Arrhénius representation

3 – DISCUSSION

In this paper we present some experimental results obtained for the ceramic AlON using a Fourier technique. Usually in sintered electrolyte, the interface electrolyte/electrolyte near the grain junction and the non-homogeneous electric field zones originate an impedance spectrum with two main contributions. In this situation, one corresponds to the polarization efects inside the grain and the other to the conduction blocking efect at the grain junction. In our case this is not observed. The absence of the second contribution may be easily understood; it is due to the low porosity of well compact samples, like our own. In fact, similar behaviour has been found in other sintered materials with porosity

ratios less than 10 %; there again the impedance spectra show a single contribution and the angle between the real axis and the half-circle diammeter is almost temperature-independent (in our case $\alpha \simeq 12^{\circ}$) [16]. Therefore the spectrum contribution may be correlated with the sample bulk properties; this represents a first step to the understanding of the electrical behaviour of this type of solid electrolytes.

REFERENCES

[1] KROGER, F. A., *The Chemistry of imperfect crystals*, North Holland Publ. Co (1974).

[2] GOOL, W. V., *Principles of defect Chemistry of crystaline solids*, Academic Press (1968).

[3] HAMMOU, A., *Les electrolytes solides*, Act. Chimique (1978).

[4] GOOL, W. V., *Fast ion transport in solids*, North Holland Publ. co (1973).

[5] HLADLIK, J., *Physics of electrolytes*, Academic Press (1974).

[6] TALLAN, N. M., *Electrical conductivity in ceramics and glass*, Marcell Decker Ed. (1974).

[7] KLEITZ, M. and DUPUY, J., *Electrode Processes in solid state ionics*, Ed. Reidel Publ. Co (1976).

[8] BAUERLE, J. E., *J. Phys. Chem. Solids*, **30** (1969), 2657.

[9] TALLAN, N. M., GRAHAM, H. C. and WIMMER, J. M., *Mater. Sci. Res.*, **3** (1966), 111-130.

[10] ARMSTRONG, R. D., RACE, W. P. and THIRSK, H. R., *Electrochim. Acta*, **13** (1968), pp. 215-219.

[11] MAGRAB, E. B. and BLOMQUIST, D. S., *The measurement of time-varying phenomena*, Wiley (1971).

[12] BOTTELBERGS, P. H. and BROEDERS, G. H. J., *J. Electroanal. Chem.*, **67** (1975), pp. 155-167.

[13] GUILLO, P., *Rapport Lab. Ceram. Nouv. Limoges* (1983).

[14] ADO, G., *Thesis Lab. Ceram. Nouv. Limoges* (1984).

[15] IL-UNG KIM et al., *J. Am. Ceram. Soc.*, **68** (8) (1985).

[16] ZIADI, A., *3eme Cycle Thesis Limoges* (1983).

MODIFIED EWALD SUM AND N, V, T ENSEMBLE IN MOLECULAR DYNAMICS OF AN IONIC SYSTEM

FERNANDO M. S. SILVA FERNANDES

Faculdade de Ciências de Lisboa — Departamento de Química e C.E.C.U.L. (INIC)
Rua Ernesto Vasconcelos, Bloco C1 - 5.º Piso — 1700 Lisbon — Portugal

BENEDITO J. COSTA CABRAL

Faculdade de Ciências de Lisboa — Departamento de Química e C.E.C.U.L. (INIC)
Rua Ernesto Vasconcelos, Bloco C1 - 5.º Piso — 1700 Lisbon — Portugal
Centro de Física da Matéria Condensada — C.F.M.C. IFM/INIC
Av. Gama Pinto, 2 — 1600 Lisbon — Portugal

(Received 25 September 1987, revised version 15 December 1987)

ABSTRACT — A molecular dynamics simulation of an ionic system has been done using a method recently suggested by Adams and Dubey for performing Ewald's summation. The damped force method of Hoover and Evans for simulation in the N, V, T ensemble has also been used. The results show that static and dynamic properties are in good agreement with experiment and N, V, E molecular dynamics simulation.

1 — INTRODUCTION

The molecular dynamics method (MD) [1] which enables the numerical solution of the Newton's equations for interacting many-body systems is now a well established approach in the study of classical fluids, and in particular, of ionic systems [2]. For these systems the truncation of the electrostatic energy contribution is not allowed and a crucial problem is to evaluate the electrostatic potential of a system of charges in a periodic cell. The classical method for calculating this potential was proposed by Ewald [3], but the expression obtained is rather complex, requiring two infinite summations, one in real space and the other in reciprocal lattice space. Nevertheless, it has been the method used so far, routinely, in molecular dynamics and Monte Carlo

simulations of ionic systems, although there exist other alternatives [4] used in the study of the One Component Plasma (OCP).

Recently, Adams and Dubey [5, 6] derived a modified expression for the Ewald's summation which enables the potential of a periodic system of charges to be obtained in a very simple and efficient way. In this approach, the electrostatic energy for a system of N interacting charges in a periodic cell is written in terms of an effective pair potential ψ_l (r) :

$$\phi^{\text{Coul}} = 1/2 \sum_{i}^{N} q_i^2 \, S + \sum_{i}^{N-1} q_i \sum_{j>i}^{N} q_j \, \psi_l \, (r_{ij}) \qquad (1)$$

The term $q_i^2 S$ is the energy due to the interaction between charge i and all its own periodic images. It is known as the self term and a neutral system it makes no contribution; r_{ij} is a nearest image vector and $\psi_l(r)$ is expanded according to:

$$\psi_l(r) = 1/r + A_2 r^2 + \sum_{n=4,6,..}^{l} (A_n \, KH_n \, (r) + B_n \, KHb_n \, (r)) \qquad (2)$$

where $1/r$ is the interaction between the charges in the basic cell, $A_2 r^2$ is the unique term which does not satisfy Laplace's equation; it is the solution of Poisson's equation and represents the contribution of the uniform neutralizing charge distribution that the Ewald summation puts around each charge. Finally the last terms is an expansion in Kubic Harmonics, which are polynomials of even order $n \geqslant 4$. For some values of n there are more than a single Kubic Harmonic. Adams and Dubey tabulated the Kubic Harmonics up to $l = 20$ and the degeneracy occurs for $n = 12$, 16, 18 and 20, i. e., $B_n = 0$ except for these values of n.

The coefficients A_n, B_n for the expansion in Kubic Harmonics KH_n, KHb_n [7], for simple cubic (SC) and truncated octahedral (TO) boundary conditions, were optimized by Adams and Dubey for several approximations ψ_l [5, 6]. The optimization was made to give the best fit of ψ_l to the true Ewald ψ (r). For molecular dynamics simulation ψ_l and its gradient are easily obtained since the Kubic Harmonics are simple known analytic functions.

In the present work we have employed SC periodic boundary conditions and ψ_l was expanded up to the tenth term. This choice

was determined by the results of the OCP study where ψ_6 is a very good approximation [6].

Most of the simulations of ionic systems by molecular dynamics have been done using the N, V, E ensemble. This makes the comparison with Monte Carlo and experimental results rather difficult. Following the pioneering work of Woodcock [8] on isothermal molecular dynamics, other methods have been proposed to perform MD at constant mean temperature [9-13]. We have employed the damped force method of Hoover [11] and Evans [12] since it has been shown [9] that the method gives results identical to those of the N, Z, E ensemble.

The corresponding algorithm in the framework of the "leapfrog" form of the Verlet scheme has been given by Brown and Clarke [9]:

$$\mathbf{v}_i'(t) = \mathbf{v}_i(t - \Delta t/2) + \mathbf{F}_i(t)\ \Delta t/2m \tag{3}$$

$$\beta^2 = (3\ (N-1)\ K_B T_D) / \Sigma\ m_i v_i'^2\ (t) \tag{4}$$

$$\mathbf{v}_i(t + \Delta t/2) = \mathbf{v}_i(t - \Delta t/2)\ (2\beta - 1) + \mathbf{F}_i(t)\ \beta\ \Delta t/m \tag{5}$$

$$\mathbf{r}_i(t + \Delta t) = \mathbf{r}_i(t) + \mathbf{v}_i(t + \Delta t/2)\ \Delta t \tag{6}$$

$$\mathbf{v}_i(t) = [\mathbf{v}_i(t + \Delta t/2) + \mathbf{v}_i(t - \Delta t/2)]/2 \tag{7}$$

where $\mathbf{v}_i'(t)$ is a projected velocity, i. e., a velocity in the absence of a damped force. T_D is the pre-defined temperature and K_B the Boltzmann constant. The damped force method reduces to simple scaling of the velocities and forces at each integration step.

2 – MODEL

Computations based on the above procedures have been carried out for molten NaCl at 1224.5 K and molar volume 39.5 $cm^3\ mol^{-1}$ with 64 and 216 rigid ions in the basic MD cube. The same system was studied by Lantelme et al. [14], but they used the N, V, E ensemble and the classical Ewald's summation.

The pair potential was the Born-Mayer-Huggins potential with parameters for NaCl reported by Adams and MacDonald [15]:

$$\phi_{ij} = q_i\, q_j/r + B_{ij}\, \exp(-\alpha_{ij}\, r) - C_{ij}/r^6 - D_{ij}/r^8 \qquad (8)$$

or

$$\phi_{ij} = \phi_{ij}^{Coul} + \phi_{ij}^{Rep} + \phi_{ij}^{DD} + \phi_{ij}^{DQ} \qquad (9)$$

The simulation started from a face centred cubic lattice with randomly distributed velocities and the constraint of total zero momentum. The time step was 0.8×10^{-14} sec. Thermal equilibration was attained after 1400 time steps. For 64 ions 2000 time steps were generated for averages, while for 216 ions they were based on 5000 additional configurations (10 runs of 500 configurations). The calculations were done on a VAX 11/730 system using double precision arithmetic.

3 — RESULTS AND CONCLUSIONS

(a) *Thermodynamics*

Thermodynamical results are presented in the table I and compared with those of Lantelme et al. [14] and also with experiment. Comparison between the two molecular dynamics simulations shows a very good agreement. Identical Coulombic energies support the equivalence of both classical and modified Ewald summation methods. Furthermore, the results of a preliminary study with 64 particles (Table I) put into evidence a size independence of the method within the present approximation. The value of C_v, calculated by the usual canonical energy fluctuation formula [16] is in good agreement with the N, V, E and experimental results. The pressure, calculated from the virial expression, is about 1.3 kbar.

(b) *Structure*

The radial distribution functions are shown in the Fig. 1. For unlike ions (g_{+-}) this function presents a first peak with

TABLE I — Thermodynamical data for NaCl

V (cm^3/mol) = 39.5 T = 1224.5 K				
	N = 216	N = 216	N = 64	
	MD(N,V,E)[14]	MD(N,V,T)	MD(N,V,T)	Exp.
U (kJ/mol) (*a*)	− 680.2	− 682.7 ± 1.6	− 681.4 ± 1.8	− 692.7[17]
ϕ^{Total} (kJ/mol)	− 710.3	− 713.3 ± 1.6	− 712.0 ± 1.8	
ϕ^{Coul} (kJ/mol)	− 797.0	− 799.5	− 797.4	
ϕ^{DD} (kJ/mol)	− 14.2	− 15.5	− 14.7	
ϕ^{DQ} (kJ/mol)	− 2.1	− 2.1	− 2.1	
ϕ^{Rep} (kJ/mol)	103.0	103.8	102.2	
C_v (J/Kmol)	56.9	53.1 ± 4		48.5[18]
P (kbar)		1.3 ± 0.8		
D_+ (10^{-4} cm^2 s^{-1})	1.08	1.02 (*b*) 1.22 (*c*)		1.31[19]
D_- (10^{-4} cm^2 s^{-1})	0.988	0.94 (*b*) 0.90 (*c*)		0.959[19]

(*a*) $U = E_k + \phi$; E_k is the kinetic energy.

(*b*) From the mean square displacement

$$D_\alpha = \lim_{t \to \infty} <|(\mathbf{r}_\alpha(t) - \mathbf{r}_\alpha(0)|^2>/6t \; ; \alpha = +, -$$

(*c*) From the velocity self-correlation function

$$D_\alpha = \lim_{t \to \infty} \int_0^t <\mathbf{v}_\alpha(t) \cdot \mathbf{v}_\alpha(0)> (1\text{-}s/t) \; ds \; ; \alpha = +, -$$

height 3.6 at 2.64 Å and a second maximum with height 1.33 at 6.1 Å. The radial distribution functions for like ions (g_{--} and g^{++}) are very similar as it is usual for the rigid ions model [2]. They present both a first maximum with values 1.76 and 1.66 at 4.0 Å and are identical after 5 Å, reflecting equivalent long range interactions for anions-anions and cations-cations.

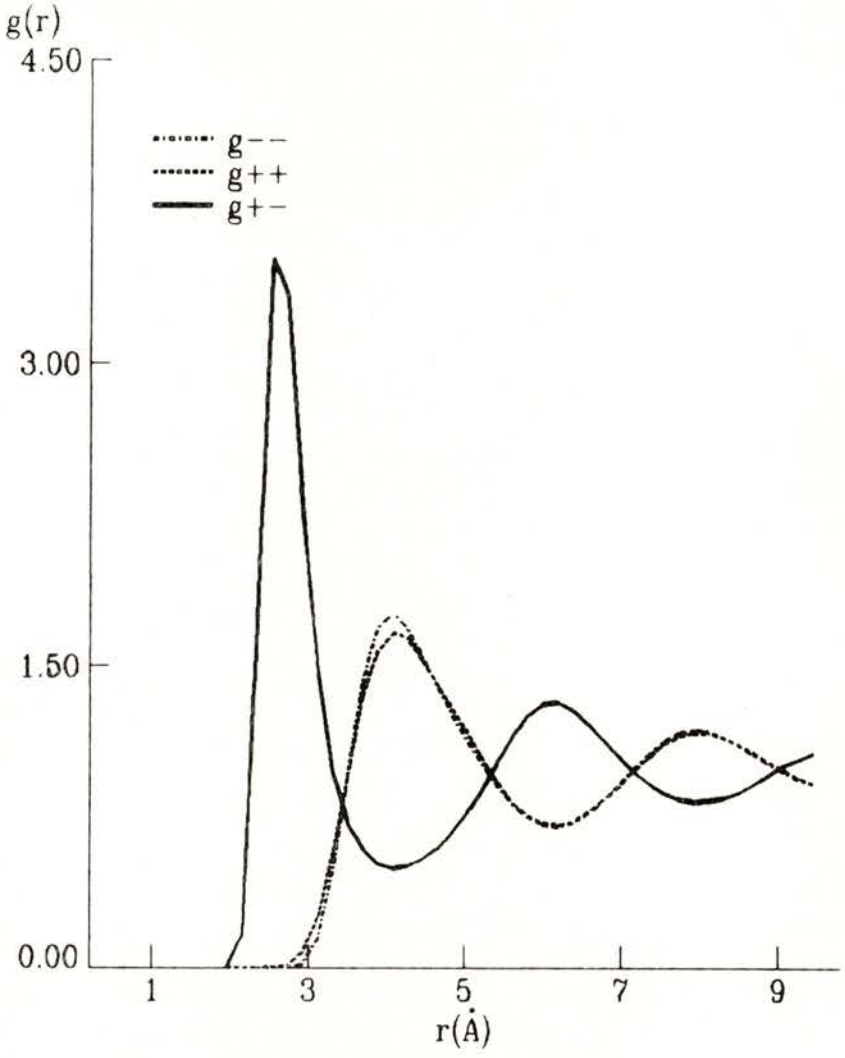

Fig. 1 — Radial distribution functions for NaCl at 1224.5 K

(c) *Time dependent-properties*

Results for the mean square displacement, velocity and force self-correlation functions are presented in the figures 2, 3 and 4. These quantities were evaluated during the simulation and each curve is the average of nine. The self-diffusion coefficient can be

evaluated either from the mean square displacement of the ions, or from the integration of the velocity self-correlation function. However, it is known [14] that in the simulation of a finite size system, during a limited time, the two methods may give different results. A difference of 19 % was obtained in the present work as shown in the Table I.

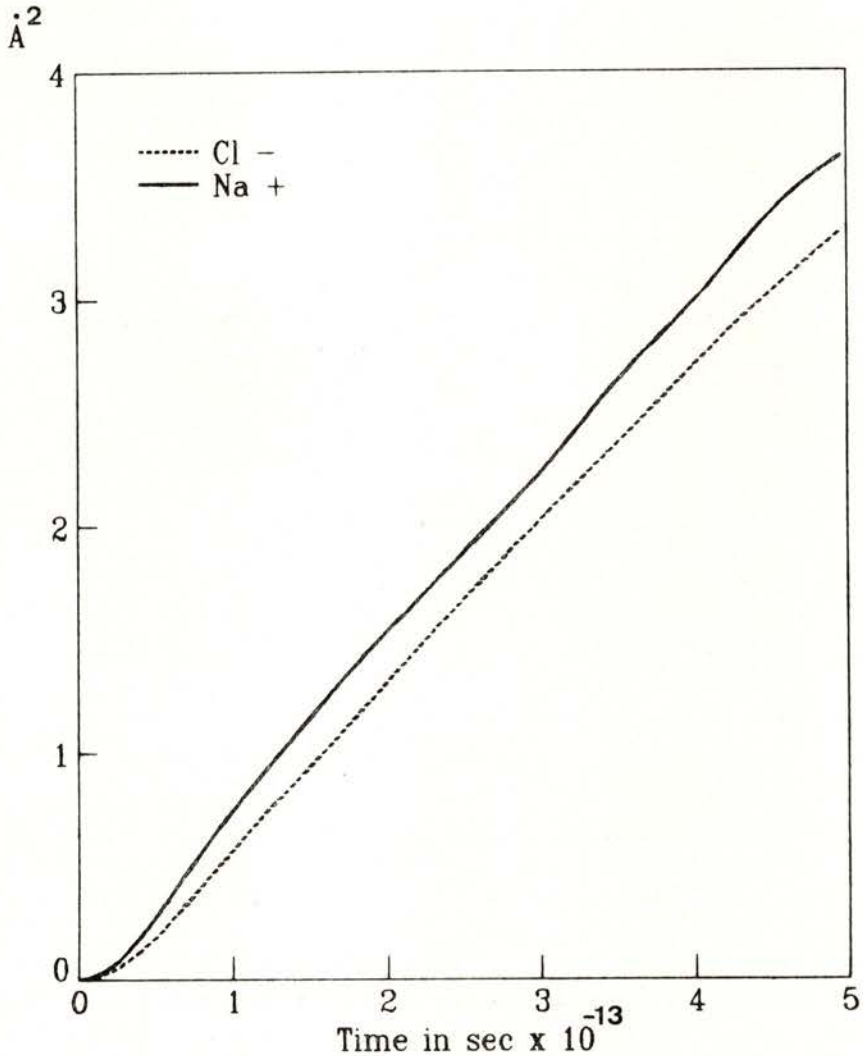

Fig. 2 — Mean square displacements of the ions in Å^2

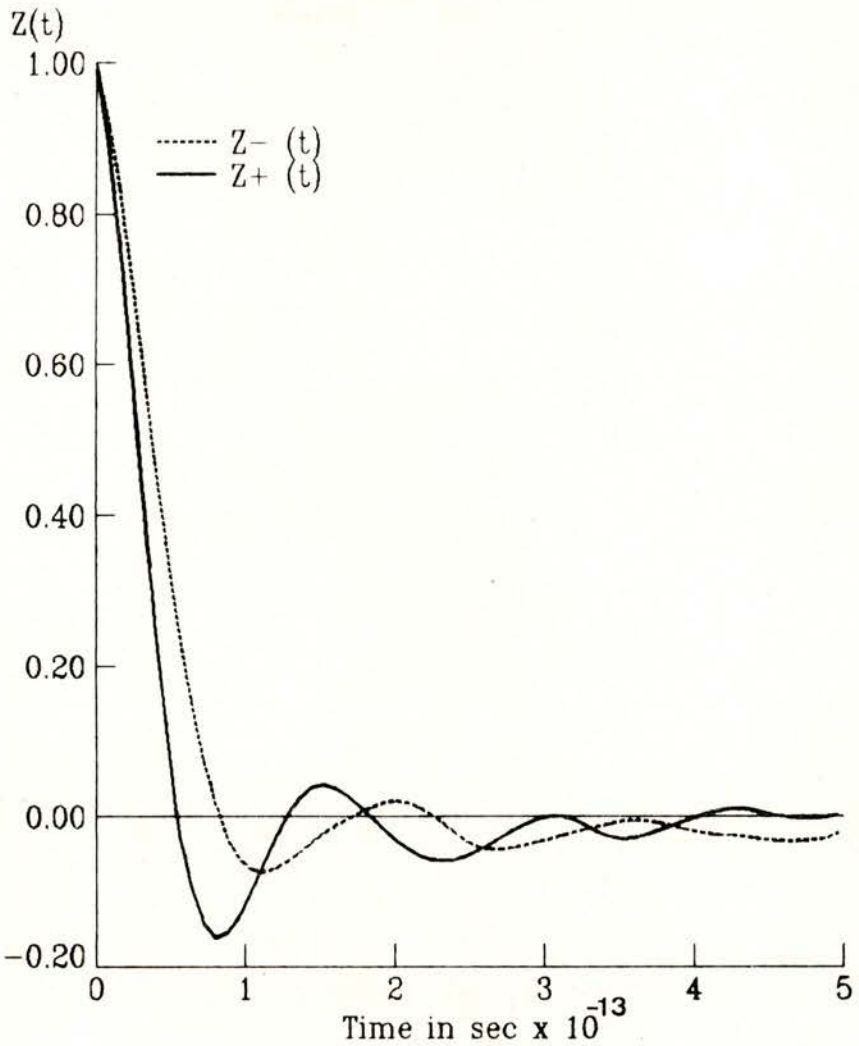

Fig. 3 — Velocity self-correlation functions for NaCl at 1224.5 K.
$z_\alpha(t) = \langle \mathbf{v}_\alpha(t) \cdot \mathbf{v}_\alpha(0) \rangle / \langle \mathbf{v}_\alpha(0) \cdot \mathbf{v}_\alpha(0) \rangle ; \alpha = +, -$

From this study it appears that the modified Ewald sum proposed by Adams and Dubey [5, 6] is a pratical and efficient method to take into account long-range electrostatic interactions in the simulation of ionic systems. The agreement of our N, V, T

simulation with N, V, E molecular dynamics simulation shows the equivalence of these ensembles for finite size ionic systems.

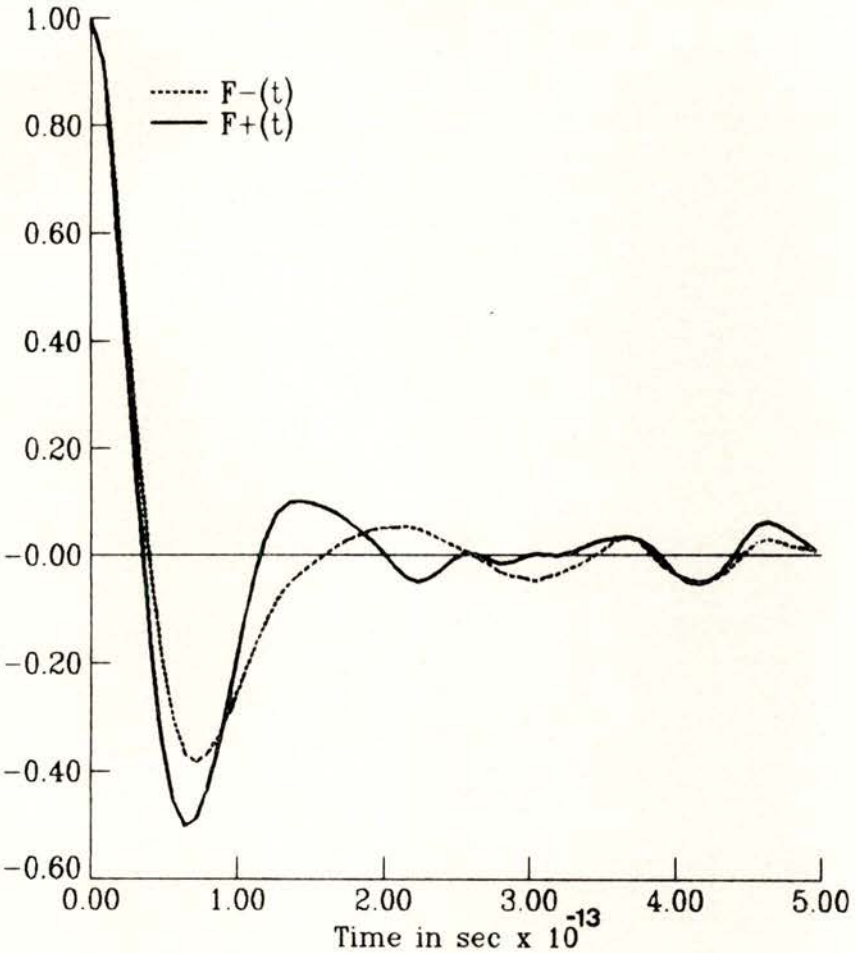

Fig. 4 — Force self-correlation functions for NaCl at 1224.5 K. $F_\alpha(t) = \langle \mathbf{a}_\alpha(t) \cdot \mathbf{a}_\alpha(0) \rangle / \langle \mathbf{a}_\alpha(0) \cdot \mathbf{a}_\alpha(0) \rangle$ where a (t) is the acceleration of the ions; $\alpha = +, -$

One of us (F. Fernandes) is grateful to Dr. David Adams of Southampton University, England, for helpful discussions on the modified Ewald sum and for providing us with copies of his papers prior to publication.

REFERENCES

[1] W. G. HOOVER, *Molecular Dynamics, Lectures Notes in Physics* n.° 258 (Springer-Verlag, 1986).

[2] M. J. L. SANGSTER and M. DIXON, *Adv. Phys.*, **25** (1976), 247; M. ROVERE and P. TOSI, *Rep. Prog. Phys.*, **49** (1986), 1001.

[3] P. P. EWALD, *Ann. Physyk* (Leipzig), **64** (1921), 253.

[4] J. P. HANSEN, *Phys. Rev.*, **A8** (1973), 3096; W. L. SLATTERY, G. D. DOOLEN and H. E. DE WITT, *Phys. Rev.*, **A21** (1980), 2087.

[5] D. ADAMS and G. DUBEY, *CCP5 Newsletter*, **22** (1986), 39.

[6] D. ADAMS and G. DUBEY, *J. Comp. Phys.*, **72** (1987), 156.

[7] F. C. VON DER LAGE and H. A. BETHE, *Phys. Rev.*, **71** (1947), 612.

[8] L. V. WOODCOCK, *Chem. Phys. Lett.*, **10** (1971), 257.

[9] D. BROWN and J. H. R. CLARKE, *Mol. Phys.*, **51** (1984), 1243.

[10] L. WOODCK, *CCP5 Newsletter*, **24** (1987), 29.

[11] W. G. HOOVER, *Physica*, **A18** (1983), 111; W. G. HOOVER, A. J. C. LADD and B. MORAN, *Phys. Rev. Lett.*, **84** (1982), 1818.

[12] D. J. EVANS, *J. Chem. Phys.*, **78** (1983), 3279.

[13] S. NOSÉ, *Mol. Phys.*, **52** (1984), 255.

[14] F. LANTELME, P. TURQ, B. QUENTREC and J. W. E. LEWIS, *Mol. Phys.*, **28** (1974), 1537.

[15] D. J. ADAMS and I. R. MACDONALD, *J. Phys.*, **C7** (1974), 2761.

[16] P. S. Y. CHEUNG, *Mol. Phys.*, **33** (1977), 519.

[17] M. P. TOSI, *J. Phys. Chem. Solids*, **24** (1963), 965.

[18] J. O. M. BOCKRIS and N. E. RICHARDS, *Proc. Roy. Soc.*, **A241** (1957), 49.

[19] J. O. M. BOCKRIS, S. NANIS and N. E. RICHARDS, *J. Phys. Chem.*, **69** (1965), 1627.

SPIN REORIENTATION TRANSITIONS AND INTRINSIC DOMAIN NUCLEATION IN UNIAXIAL MAGNETS

D. MELVILLE
Lancashire Polytechnic, Preston, England

J. M. MACHADO DA SILVA and J. F. D. MONTENEGRO
Centro de Física (INIC), Universidade do Porto, 4000 Porto, Portugal

(Received 10 October 1987)

ABSTRACT — The nature of anisotropy-energy driven spin-reorientation transitions in uniaxial materials has been studied. A simple phenomenological model is developed to describe first and second order transitions for situations where the first two anisotropy constants vary linearly with temperature. The mechanism whereby first order transitions take place is studied and calculations made of the domain wall structure. It is shown that an intrinsic nucleation mechanism exists for 90° domain walls and that in multidomain samples the existence of domains always leads to the conversion of first order transitions to those of second order. It is shown that this analysis gives a satisfactory account of the spin reorientation transition in $Pr_2 (Co_{0.8} Fe_{0.2})_{17}$.

1 – INTRODUCTION

A wide range of spin re-orientation transitions in uniaxial orthoferrites and metallic rare earth compounds (Belov et al. [1], Melville et al. [2]) take place because of the particular temperature dependence of their magnetocrystalline anisotropy constants. Transitions are from an axial ($\Theta = 0$) phase to a planar phase ($\Theta = \pi/2$) and in principle take place either continuously via two second order transitions through an intermediate easy cone situation if $K_2 > 0$, or as a single first order transition if $K_2 < 0$.

In such transitions the relevant term in the free energy is to second order in the anisotropy constants

$$F = K_1 (T) \sin^2\Theta + K_2 (T) \sin^4\Theta . \qquad (1)$$

The change in heat capacity at spin reorientation transitions with $K_2 > 0$ has been considered in a simple model with K_2 constant by Horner and Varma [3]. In the present work we extend their approach to more general situations and then examine the means by which spin reorientations take place. In particular we look at the role of domain walls in first order spin reorientation transitions in uniaxial systems.

2 – THERMODYNAMICS OF SPIN REORIENTATION TRANSITIONS

We examine first a simple illustrative model which, after Horner and Varma [3] considers K_2 to be constant and K_1 to be linear in temperature

$$K_1 (T) = K_2 (A + BT) \tag{2}$$

where A and B are constante whose magnitude and sign are determined by the conditions $K_2 \gtrless 0$ and $dK_1/dT \gtrless 0$.

Fig. 1 shows the trajectories considered, with the arrows indicating direction of changing K_1 with increasing temperature. Substitution of (2) into (1) leads to the following results.

$K_2 > 0$:

H parallel to	Axis	Cone	Plane
Θ	0	$\sin^{-1} [(A + BT)/2]^{1/2}$	$\pi/2$
Entropy $S(\Theta)$	0	$\frac{1}{2} K_2 B (A + BT)$	$-K_2 B$
Heath Capacity $C(\Theta)$	0	$\frac{1}{2} K_2 B^2 T$	0

Thus for temperature increasing the total entropy change is always $\Delta S = |K_2 B| = |dK_1/dT|$ and the heat capacity and entropy take the shape shown fig. 2a and 2b respectively.

$K_2 < 0$:

H parallel to	Axis	Plane
Θ	0	$\pi/2$
Entropy $S(\Theta)$	0	$-K_2B$
Heat capacity $C(\Theta)$	0	0

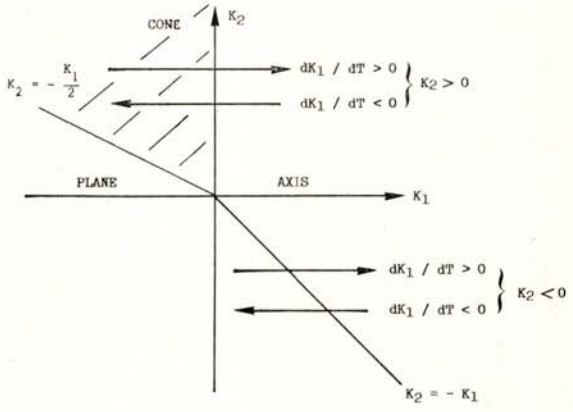

Fig. 1 — Spin reorientations in the K_2, K_1 plane

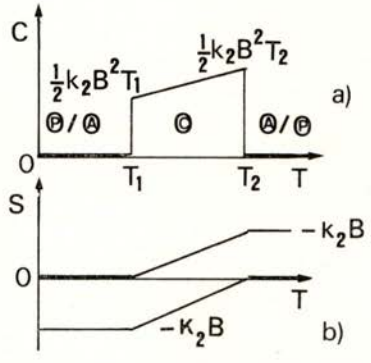

Fig. 2 — (a) Heat capacity for constant $K_2 > 0$, corresponding to $B > 0$ (plane stable for $T < T_1$) and $B < 0$ (axis for $T < T_1$)
(b) Entropy for constant $K_2 > 0$. Lower curve $B > 0$. Upper curve $B < 0$

In this case the transition from axis to place or vice versa takes place at $T = T_0$ with entropy increase $-K_2B = |dK_1/dT|$ and a positive singularity in the heat capacity. The heat capacity and entropy are as shown in Figs. 3a and 3b respectively.

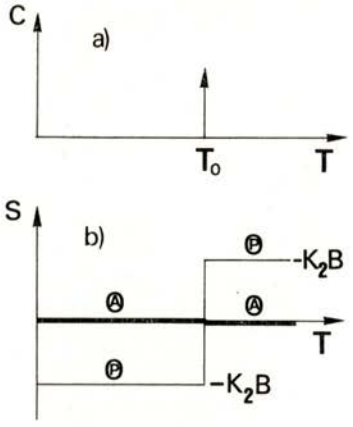

Fig. 3 — (a) Heat capacity for constant $K_2 < 0$, corresponding to $B > 0$ (plane stable at $T < T_0$) and $B < 0$ axis stable for $T < T_0$
(b) Entropy for constant $K_2 < 0$. Lower curve $B > 0$. Upper curve $B < 0$

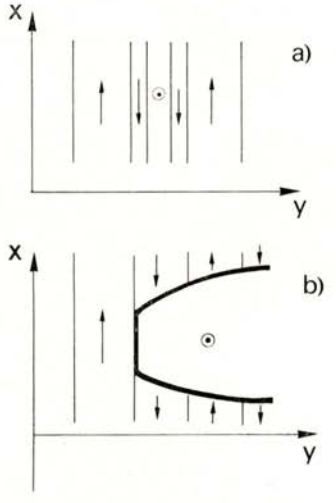

Fig. 4a, b — Schematic domain structures as T_0 is approached. The heavy lines correspond to $\pi/2$ domain walls

This illustrative model can readily be extended to the situation often observed experimentally where both K_1 and K_2 are temperature dependent. Thus we can write in general

$$K_1(T) = \alpha + \beta T$$
$$K_2(T) = \gamma + \varepsilon T \qquad (3)$$

In this case for $K_2 > 0$ we have

H parallel to	Axis	Cone	Plane
Θ	0	$\sin^{-1}\left(\frac{-(\alpha+\beta T)}{2(\gamma+T)}\right)^{1/2}$	$\pi/2$
Entropy $S(\Theta)$	0	$\frac{1}{4}\frac{[2\alpha\beta\gamma + 2\beta^2\gamma T + \beta^2 T^2 - \alpha^2\varepsilon]}{(\gamma+T)^2}$	$-(\beta+\varepsilon)$
Heat Capacity $C(\Theta)$	0	$\frac{T(\alpha\varepsilon-\beta\gamma)^2}{2(\gamma+\varepsilon T)^3}$	0

where the easy cone region is defined by temperatures $T_1 = -\alpha/\beta$ and $T_2 = -(\alpha + 2\gamma)/(\beta + 2\varepsilon)$ corresponding to $\Theta = 0$ and $\Theta = \pi/2$ respectively.

For $K_2 < 0$ we have.

H parralel to	Axis	Plane
Θ	0	$\pi/2$
Entropy $S(\Theta)$	0	$-(\varepsilon+\beta)$
Heat capacity $C(\Theta)$	0	0

The form of the entropy and heat capacity is exactly as in Figs. 3a and 3b but with $-K_2B$ replaced by $-(\varepsilon + \beta)$.

3 – DOMAIN NUCLEATION NEAR SPIN REORIENTATION TRANSITIONS

The discussion above does not attempt to address the problem of how the thermodynamically stable state at the end of a transition is reached.

We consider this question now and concentrate on the $K_2 < 0$ case where thermodynamics predicts a first order reorientation at $T = T_0$. In a multidomain sample the situation is complicated by the existence in each phase of a part of the specimen (the domain wall) with spins whose angles differ from the easy direction for the phase considered ($\theta = 0$ or $\pi/2$). These domain walls act as nuclei for the formation of the new phase since at all temperatures they contain spins whose direction corresponds to that of the currently unstable phase.

This point has already been noted by Belov et al. [1] in considering antiferromagnetic to weak ferromagnetic phase transitions in orthoferrites, by Mitsek et al. [5] and Baryakhtar et al. [6] for uniaxial antiferromagnets and by Belov et al. [1] for spin-flip transitions in cubic ferrimagnets. We present here a detailed shape analysis for 180° domain walls in a uniaxial material when a first order phase transition in which $K_1 + K_2 = 0$ ($K_2 < 0$) is approached.

We can write the total free energy of a single domain wall as

$$F = \int_{-\alpha}^{\alpha} \left[A \left(\frac{d\theta}{dy} \right)^2 + K_1 \sin^2\theta + K_2 \sin^4\theta \right] dy$$

where A is the exchange constant and y is a position coordinate across the wall. The corresponding Euler equation is [7].

$$A \frac{d}{d\theta} \left(\frac{d\theta}{dy} \right)^2 + 2K_1 \sin\theta \cos\theta + 4K_2 \sin^3\theta \cos\theta = 0$$

Thus with y measured from the wall centre we have (for 180° walls)

$$y_\pi(\theta) = \int_{\pi/2}^{\theta} [(K_1/A) \sin^2\theta + (K_2/A) \sin^4\theta]^{-1/2} d\theta \qquad (4)$$

Integration of (4) yield.

$$y_\pi(\Theta) = \sqrt{A/K_1}\ \log\ \tan\ (\tan^{-1}\ (\sqrt{1+K}\ \tan\ \Theta)/2) \qquad (4a)$$

with inverse relation

$$\Theta_\pi(y) = \tan^{-1}\ [\tan\ (2\ \tan^{-1}\ \exp(\sqrt{\frac{K_1}{A}}\ y))/(1+K)] \qquad (4b)$$

where $K = K_2/K_1$.

The domain wall thickness is given according to the usual approximation [7]

$$\delta_\pi \simeq \pi\ (\delta y/\delta\Theta)_{\Theta=\pi/2} \quad \text{as} \quad \delta_\pi \simeq \pi\sqrt{\frac{A}{K_1+K_2}} \qquad (5)$$

It is instructive to consider the approach to a spin reorientation transition with $K_2 < 0$ as K_1 decreases from a large positive value to the point where the transition takes place and $K_1(T_0) = -K_2(T_0)$. For $K_1 > -2K_2$ the axial phase has a minimum energy and the planar phase is a maximum and the sample will exist as a set of 180° domains parallel to the c axis. At a temperature T_1 where $K_1(T_1) = -2K_2(T_1)$ the planar direction also becomes an energy minimum, but not an absolute minimum. This will produce initially a tendency to pin the 180° domain wall at its centre. However as the point. $K_1(T_0) = -K_2(T_0)$ is approached it becomes more and more favourable for spins to lie in this metastable energy direction. This process is aided by the associated lowering of exchange energy which alignment brings. Thus the spins existing in the $\pi/2$ direction act as a nucleus for the creation of two or more 90° domain walls,. In terms of equation (5) the 180° domain wall width tends to infinity. This will lead to domain structures of the type schematically illustrated in Figs. 4a and 4b.

It is possible to study this process by calculating the domain wall structure as a function of K_2/K_1 using equation (4b). The results are shown in Fig. 5 where the calculation has been made at 300 points across the wall. It can be seen that as T_0 is

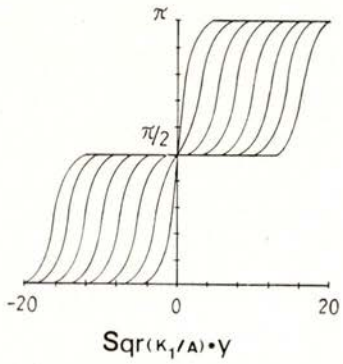

Fig. 5 — Variation of spin direction in a 180° domain wall as K_2/K_1 changes from 0 to close to -1. K_2/K_1 values: (a) 0; (b) $-(1\text{-}10^{-1})$; (c) $-(1\text{-}10^{-2})$; (d) $-(1\text{-}10^{-3})$; (e) $-(1\text{-}10^{-4})$; (f) $-(1\text{-}10^{-5})$; (g) $-(1\text{-}10^{-6}$; (h) $-(1\text{-}10^{-7})$

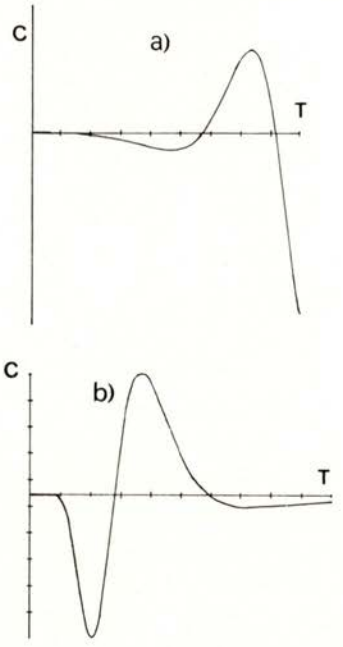

Fig. 6 — Heat capacity variation predicited for $Pr_2 (Co_{.8} Fe_{.2})_{17}$ by equation (8) using

(a) $\Theta(T) = \frac{\pi}{2}\left[1 - \left(\frac{T - T_1}{\Delta T}\right)^3\right]$ and

(b) $\Theta(T) = \frac{\pi}{2}\left[1 - \exp\text{-}(T - T_1)^{-2}\right]$

approached the 180° domain wall splits into two 90° domain walls leading to what are effectively metastable 90° domains. Thus there is a coexistence of easy axis and easy plane domains before T_0 is reached. The same effect is present in the transition from easy plane to easy axis. A complete picture of the sample domain structure is not easy to obtain, but it is clear that the result of the process described above is to produce a *continuous* change from easy axis to easy plane magnetisation and vice versa. This change will occupy a small temperature range on either side of T_0. Thus over a small temperature range as T_0 is approached a large number of 90° domain walls will exist and therefore a significant number of spins will be lying in non-symmetry directions. This large number of domain walls should manifest itself as an increase in ultrasonic attenuation.

Our conclusion therefore is that in multidomain samples the domain structure converts first order reorientation transitions to continuous transitions. The same conclusion can be made in the case of first order magnetisation processes [8], [2] where spin reorientations associated with anisotropic effects are produced by the application of external magnitic fields.

4 — HEAT CAPACITY AT T_0 IN A MULTIDOMAIN SAMPLE

Recently [4] we have reportend measurements on the heat capacity of $Pr_2 (Co_{0.8} Fe_{0.2})_{17}$. This uniaxial material [2] has $K_2 < 0$ and undergoes a spin reorientation transition from easy plane to easy axis as temperature is increased through $T_0 = 188$ K. The phase transition, as seen in the heat capacity, occupies an interval of 2.5 K and is predominantly negative going with a final sharp positive going peak.

In the spirit of the discussion in section above we construct a simple model of this transition as being associated with an effectively *continuous* variation of the average magnetisation vector from $\Theta = \pi/2$ to $\Theta = 0$ as temperature is increased through this small temperature interval. Thus we can assign an average free energy

$$F(\Theta) = K_1 \sin^2\Theta + K_2 \sin^4\Theta \qquad (6)$$

and an entropy

$$S(\Theta) = -[(dK_1/dT + dK_2/dT \sin^2\Theta) \sin^2\Theta + (K_1 + 2K_2 \sin^2\Theta) \frac{d \sin^2\Theta}{dT}] \quad (7)$$

and a heat capacity

$$C(\Theta) = -T[(K_1 + K_2 \sin^2\Theta)(2 \cos 2\Theta (d\Theta/dT)^2 + \sin 2\Theta (d^2\Theta/dT^2)) + 2(dK_1/dT + \sin^2\Theta \, dK_2/dT) \sin 2\Theta (d\Theta/dT) + 2(dK_2/dT) \sin^2\Theta \sin 2\Theta (d\Theta/dT) + 2K_2 \sin^2 2\Theta (d\Theta/dT)^2] \quad (8)$$

These expressions differ from those for the $K_2 > 0$ case since there is no direct connection between Θ and K_1, K_2 as in the easy cone situation.

From (6) and (7) the changes in entropy and heat capacity at the transition as temperature increases are

$$\Delta S = \left(\frac{dK_1}{dT} + \frac{dK_2}{dT} \right) \text{ and } \Delta C = 0$$

as in section 2 above. However the variation with temperature during the transition is interesting.

For $Pr_2 (Co_{0.8} Fe_{0.2})_{17}$ dK_1/dT and dK_2/dT are both positive [4] so that the first term in (7) will produce a monotonic increase from $-(dK_1/dT + dK_2/dT)$ to zero as Θ changes from $\pi/2$ to 0. In the second term, $d\sin^2\Theta/dT$ is always negative while $(K_1 + K_2 \sin^2\Theta)$ varies from $(K_1 + K_2)$ (> 0) to K_1 (> 0). Thus the overall contribution of this term to the entropy is an initially negative going shape followed by a positive peak and a return to zero.

The negative contribution to the entropy arises always from the K_2 component of the second term which is associated with the forcing of the spins into the metastable energy minimum corresponding to $\Theta = 0$. This is mediated by the domain wall nucleation process discussed in section 3 above. This negative contribution to entropy will lead therefore to the negative heat capacity peak observed experimentally.

The precise form of the heat capacity as a function of temperature predicted by equation (8) depends critically on the temperature variation of the average spin orientation Θ (T). This is not known but it is possible to speculate in view of the mechanism suggested above that it will vary initially rather slowly with a rapid acceleration as T_0 is approached. In Fig. 6, we plot the form predicted by equation (8) using the experimental anisotropy data [2, 4]

$$\text{for: (a)} \quad \Theta(T) = \pi/2 \left[1 - \left(\frac{T - T_1}{\Delta T} \right)^3 \right] \text{ and}$$

$$\text{(b)} \quad \Theta(T) = \pi/2 \left[1 - \exp\left(-1/(T - T_1)^2 \right) \right],$$

where $\Delta T = 2.5$ K and $T_1 = 183.2$ K is the point where Θ departs from $\Theta = \pi/2$. It can be seen that both of these functions lead to the negative and positive peaks observed experimentally. It is unlikely however that any simple analytical function of this type will describe Θ (T) accurately. The indications from our own fitting attempts is that the variation Θ (T) which describes this particular data is most likely sigmoidal. This is a function which begins and ends slowly, but contains a rapid central variation. Such a form is also likely from the physics of the above model since 90° wall nucleation is initially gradual as T_0 is approached, but will only be complete asympotically.

5 – CONCLUSIONS

It has been shown that for spin reorientations in uniaxial materials with $K_2 > 0$ the heat capacity variation in the easy cone region can take a variety of shapes, depending in detail on the temperature dependence of the anisotropy constants. For $K_2 < 0$, the presence of domains changes first order spin reorientation transitions into those of second order with 90° domain walls nucleating at the centre of 180° walls.

We are grateful to Professor J. H. Araújo for illuminating discussions. Financial support from I. N. I. C. is acknowledged.

REFERENCES

[1] BELOV, K. P., ZVEZDIN, A. K., KADOMTSEVA, A. M., KRYNETSKII, I. B. and OVCHINNIKOVA, T. L., *Sov. Phys. Solid State* **16**, 1698-1700 (1975).

[2] MELVILLE, D., KHAN, W. I. and RINALDI, S., *IEEE Trans. Magn.* Mag-12, 1012 (1976).

[3] HORNER, H. and VARMA, C. M., *Phys. Rev. Lett.* **20**, 845 (1968).

[4] GUEDES DE SOUSA, E. B., SÁ, M. A., MONTENEGRO, J. F. D., MACHADO DA SILVA, J. M. and MELVILLE, D., *Solid State Comm.* **49**, 853-4 (1984).

[5] MITSEK, A. Z., KOLMAKOVA, N. P. and GAIDANSKII, P. F., *Soviet Physics Solid State* **11**, 1021-26 (1969).

[6] BARYAKHTAR, V. G., BAROVIK, A. E. and POPOV, V. A., *J.E.T.P. Lett* **9**, 391-2, (1969).

[7] LÁNDAU, L. D. and LIFSCHITZ, E. M., *Electrodynamics of continuous Media* (Course on Theoretical Physics, Vol. 8), Pergamon, Oxford (1960).

[8] ASTI, G. and RINALDI, S., *J. Appl. Phys.* **45**, 3600 (1974).

IONOSPHERIC PERTURBATIONS ON GPS OBSERVATIONS

LUÍSA BASTOS
Observatório Astronómico — Monte da Virgem, 4400 V. N. de Gaia — Portugal

(Received 5 August 1987)

ABSTRACT — The new satellite positioning system, the Global Positioning System (GPS), is having a great impact in solving all problems involving threedimensional position determination, on earth or space, with applications that go beyond Geodesy.

At the present state-of-art of receiver technology, the measuring precision is no longer a limiting factor in the final accuracy of the results. The utmost accuracy attainable with this system depends upon our capability to model the errors that may affect the observations, such as orbit and atmospheric propagation errors.

In this article we shall be concerned with ionospheric disturbance of radio signals transmited from the Navstar/GPS satellites. A summary of the different proposed ionospheric time delay models is presented and some comments concerning its application to the analysis of real data are made.

1 – INTRODUCTION

The principle of operation of GPS is based on the measurement of station-satellite distances using the radio signals that are continuously transmitted by the NAVSTAR / GPS satellites and subsequent computation of the observer's coordinates.

Instrumental errors have already been reduced to a few centimeters in the measured phase (Evans [1]); therefore orbital and propagation errors play a decisive role in the final accuracy of the results.

Here we shall discuss only problems related to the propagation of the signals in the ionosphere.

Ionospheric effects are extremely hard to model due to the high degree of variability of the neutral atmosphere. The result is mainly a delay of the propagation time. Because this delay is frequency dependent, a first order correction may be obtained

observing in two frequencies properly chosen. However, for the purpose of very precise geodetic positioning, the accuracy with which that correction is determined still needs to be improved.

The availability of better prediction models of ionospheric propagation delay along specific paths, all over the world, is of great interest for GPS users operating with single frequency receivers. These will perhaps be the most popular in the future, not only because they are less expensive but also because, for security reasons, the Departement of Defense of the United States may restrict the use of the second frequency.

The ionospheric delay at the primary GPS frequency (1575.42 MHz) can reach 50 nanoseconds in worst conditions. This will result in an error of about 15 m in the measured station-satellite range. Single frequency users are able to correct only 60 % of this error and the ionosphere will be a major limiting factor in the final accuracy. Due to the variability of the ionosphere in space, time and geophysical conditions, it is impossible to extrapolate ionospheric parameters for different locations. Users who require the highest accuracy must use the dual frequency capability of GPS.

In what follows we shall start with a short description of the GPS system and a brief review of some aspects concerning ionospheric behaviour at L-band frequencies. How specific characteristics of the GPS signals may be explored, in the different models, to analyse ionospheric effects, will then be our main concern.

2 – SYSTEM DESCRIPTION AND USE

GPS is a satellite based system, that when in full operation by the end of this decade, will be supported by a constellation of 18 satellites (actually 9 are already in orbit), at an altitude of about 20000 Km, equally spaced in 6 planes (3 by plane) with an inclination of 55° over the equator. The period of the near circular orbits is about 12 hours.

The satellites transmit continuously in two L-band frequencies, L_1 at 1575.42 MHz and L_2 at 1227.60 MHz, multiples of the basic frequency of the on-board oscillator, of 10.23 MHz, and a navigation message containing the satellite ephemeris is encoded on those carriers.

An observer, equipped with a GPS receiver, will be able to receive the signals, simultaneously, from at least four satellites, at any place on earth, 24 hours a day, under all atmospheric conditions. The corresponding station-satellite distances may be computed, using the known satellite position, and the observer can have, in a few minutes, his coordinates in the same threedimensional geocentric system to which the orbits are referred.

The most accurate method to obtain the station-satellite range is to measure the phase of the incoming signals. The range error may be of a few decimeters, depending on the degree of accuracy with which instrumental, orbital, clock, multipath and atmospheric propagation errors are modelled. The system reaches its maximum accuracy in relative positioning determination, i. e., baseline measurements.

With a GPS receiver we can measure the carrier phase difference between the signal transmitted by the satellite and the one generated in the receiver's oscillator. This difference may be expressed as (Goad [2]):

$$\Phi_j^i\,(t_r) = \Phi^i\,(t_t) - \Phi_j\,(t_r)\ , \qquad (2.1)$$

where t_t refers to transmit time from satellite i, and t_r to receipt time at receiver j. Assuming we have highly stable oscillators we can express the transmit time as:

$$t_t = t_r - (f/c)\ \rho_j^i\ ,$$

with f being the frequency, c the speed of light in vacuum and ρ_j^i the station-satellite range.

Ignoring for the time being all sources of error (resulting from time, orbit and propagation errors), we can rewrite equation (2.1) as

$$\Phi_j^i\,(t_r) = \Phi^i\,(t_r) - (f/c)\,\rho_j^i - \Phi_j\,(t_r) + N_j^i \qquad (2.2)$$

where N_j^i is an integer that has been introduced to account for the uncertainty in the number of cycles of the first measurement. In the reduction procedure it will be considered as an additional unknown.

In equation (2.2) the station coordinates are implicit in the term $(f/c)\,\rho_j^i$, and can be derived once the positions of the satellites are known.

In the present stage of development of GPS, allowing observations not in the most favourable conditions, the results already reach an accuracy of 1 to 5 p.p.m. in the determination of baselines with some tens of kilometers.

Precise modelling of ionospheric perturbations on GPS observations is essential for achieving a 0.1 p.p.m. accuracy in longer baselines; this is expected for the near future.

3 — IONOSPHERIC PERTURBATIONS AT L-BAND FREQUENCIES

The ionospheric effect on radio wave propagation is mainly a delay in the propagation time, although a bending of the trajectory is also observed. As is well known, the ionospheric behaviour is highly correlated with the columnar electronic density along the path ray. This quantity is greatly influenced by earth rotation, geomagnetic latitude and solar activity and therefore it is difficult to predict.

At frequencies above 400 MHz the ionospheric phase refraction index can be given by the approximate formula (Davidson et al. [3]:

$$n_{ph} \simeq 1 - (40.3/f^2)\ N_e\ , \tag{3.1}$$

where f is the carrier frequency and N_e the columnar electronic density. The total phase delay experienced by a wave propagating through the ionosphere will then be given by:

$$\delta\Phi = (f/c) \int (n_{ph} - 1)\ ds$$

or, using (3.1),

$$\delta\Phi = -[40.3/(fc)] \cdot \int N_e\ ds \tag{3.2}$$

As the ionosphere is a dispersive medium, the group refraction index does not equal the phase refraction index; it is given by:

$$n_g = n_{ph} + f \, dn_{ph} / df \ .$$

Substituting n_{ph} given by (3.1) we get for n_g :

$$n_g = 1 + (40.3/f^2) \ N_e$$

and for the group delay

$$\delta t = [40.3/(f^2 c)] \ . \ N_t \qquad (3.3)$$

N_t is the integral of the columnar electronic density along the line of sight, usually referred to as Total Electron Content (TEC).

Comparing equations (3.2) and (3.3) we conclude that the phase velocity is advanced while a correspondent retardation is observed for the group velocity. These effects depend mostly on the value of TEC.

For observations near the zenith δt can grow up to 30 nanoseconds. As N_t is quickly changing with the propagation direction, the ionospheric error in the measured range can reach tens of meters for directions far from the zenith. Since we know that TEC is very much influenced by solar activity (Clynch [4]), we can expect very severe perturbations in periods of maximum solar activity in the eleven year solar cycle, such as in the early nineties. The need for worldwide TEC models based on direct measurements can be easily understood from what has been said.

4 – ANALYSIS OF IONOSPHERIC PERTURBATIONS ON GPS SIGNALS

There is no doubt that the improvement of GPS results depends on the precise determination of ionospheric effects upon the observed signals. The tests undertaken so far (Lachapelle [5], Kleusberg [6]) show that the importance of this correction grows with baseline length and that the error is of the order of 1 p.p.m. over the measured distance. A rotation of the baseline has also been detected as a result of atmospheric effects.

The methods commonly used to compute ionospheric parameters are based on Faraday rotation measurements of the signals transmitted by geostationary satellites and Doppler or range measurements using satellite observations in two frequencies. The disadvantage of these methods is that the spatial coverage of the observations is limited and we are not able to correct the total ionospheric error.

Let us see how ionospheric perturbations can be handled in GPS observations.

The GPS satellites transmit in two L-band frequencies as mentioned before. The carrier frequencies, L_1 and L_2 are biphase modulated with a pseudo random noise (PRN) binary code at a rate of 10.23 MHz (Spilker [7]).

If we have a dual frequency receiver, the specific characteristics of those signals can be explored in different ways to get further knowledge about the ionosphere, as we shall see next.

4.1 — We have seen in paragraph 3, that the ionosphere is responsible for a phase advance, which is inversely proportional to the frequency. Neglecting other sources of error, we can rewrite equation (2.2) to account for this effect [2]:

$$\Phi^i_j\,(t_k) = \Phi^i\,(t_k) - (f/c)\;\rho^i_j - \Phi_j\,(t_k) + N^i_j + (A/f)\;,$$

where t_k is the receipt time at epoch k.

Since L_1 and L_2 are multiples of the same basic frequency, the respective phases differ by the ratio f_1/f_2.

Observing in both frequencies we may write:

$$\Phi^i_j\,(t_k)_{L1} = \Phi^i\,(t_k) - \Phi_j\,(t_k) - (f_1/c)\,\rho^i_j + N^i_j\,(L_1) + A/f_1 \qquad (4.1.2)$$

and

$$\Phi^i_j\,(t_k)_{L2} = f_2/f_1\;[\Phi^i\,(t_k) - \Phi_j\,(t_k) - (f_1/c)\;\rho^i_j] + N^i_j\,(L_2) + A/f_2 \qquad (4.1.3)$$

Now these two equations can be combined in the form:

$$\delta I = \Phi^i_j\,(t_k)_{L1} - f_1/f_2\;\Phi^i_j\,(t_k)_{L2}$$

The resulting quantity is independent of time errors:

$$\delta I = N_j^i\ (L_1) - f_1/f_2\ N_j^i\ (L_2) + (1 - f_1^2/f_2^2)\ (A/f_1)\ . \qquad (4.1.4)$$

If phase lock is maintained the integers N will remain constant during the observation session, and epoch to epoch changes in δI will be only due to the ionosphere.

In figure 1 we have plotted epoch changes of this L_1/L_2 phase combined quantity relative to the initial epoch, for satellite 9.

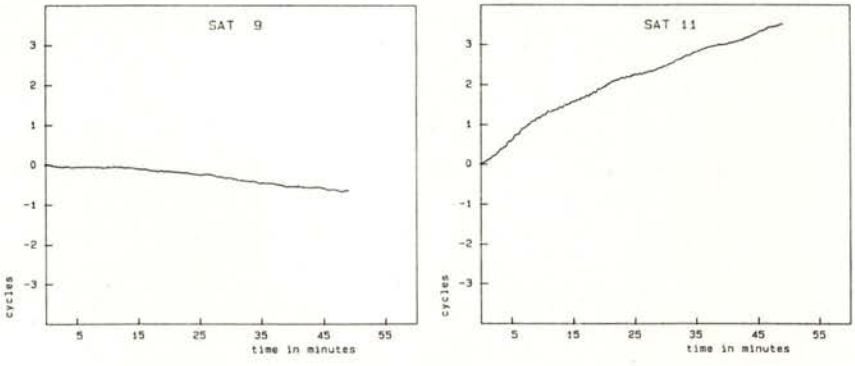

Fig. 1 — L_1/L_2 phase combination for satellites 9 and 11

The observations were made during the early hours of one morning in September 1986. Data were collected, with dual frequency Tl 4100 receivers, every 3 seconds. The station was located south of Munich at about 47° north latitude and 11° east longitude. Near sunrise, the ionosphere is still relatively quiet. The satellite elevation angle, above 60°, was slowly changing during this 45 minutes observation span, giving the smooth trend observed.

Figure 1 shows also similar data for satellite 11. Taking into account that the elevation angle of this satellite was below 30° and increasing, we can see δI monitoring the ionospheric behaviour.

In figure 2, δI was plotted for satellite 6 observed from two close stations (Bastos and Landau [8]). It shows a high degree of correlation what was expected since ionospheric disturbance is highly correlated with earth location and line of sight.

One way to avoid ionospheric effects on GPS observations, without having to compute any ionospheric parameters is suggested by Goad [2]. It consists in using a linear combination of the type

$$\Phi^i_j\,(t_k) = \alpha_1\,\Phi^i_j\,(t_k)_{L1} + \alpha_2\,\Phi^i_j\,(t_k)_{L2}\;;$$

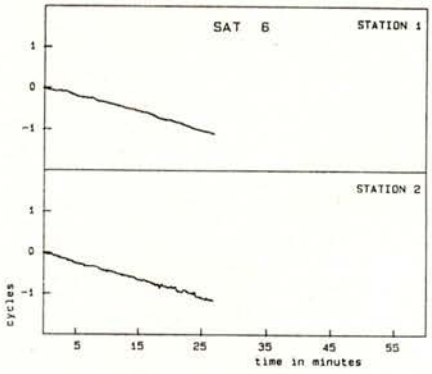

Fig. 2 — L_1/L_2 phase combination for satellite 6 and two stations

where α_1 and α_2 are appropriate functions of the two frequencies f_1 and f_2. However this ionospheric corrected phase has the disadvantage of increasing, by a factor of 2 or 3, instrumental and multipath errors (Evans [1]); therefore one should avoid this phase combination and use the raw phases, computing accurately the correspondent ionospheric correction.

4.2 — One of the most common techniques to compute the group delay is based on dual frequency observations making use of the dispersive nature of the ionosphere. We have seen in paragraph 3 that the group delay is inversely proportional to the square of the frequency. Following Jorgensen, we can write:

$$D_{L1} = K/f_1^2 \qquad \text{and} \qquad D_{L2} = K/f_2^2\;,$$

where K is the constant of proportionality, and D_{L1} and D_{L2} the delays, in meters, respectively at the L_1 and L_2 frequencies.

With a dual frequency receiver we are able to measure the difference in the delays at each carrier frequency:

$$D = D_{L1} - D_{L2}$$

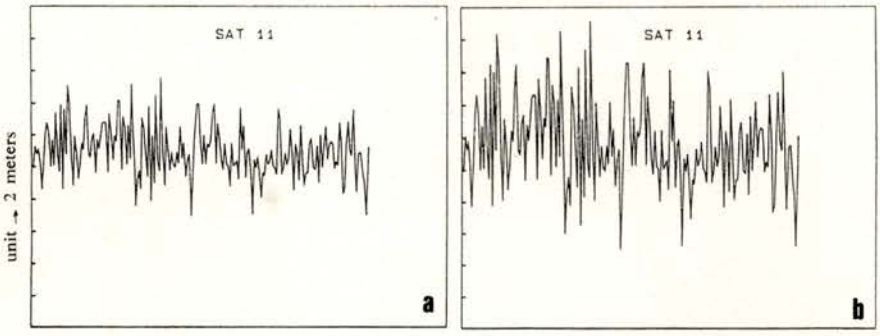

Fig. 3 — Absolute ionospheric delays for frequencies L_1 (3a) and L_2 (3b)

After simple calculations and substituting f_1 and f_2 for its values we get:

$$D_{L1} = 1.54573\ D \qquad (4.2.1)$$

and

$$D_{L2} = 2.54573\ D \qquad (4.2.2)$$

Neglecting higher order terms these equations give us the absolute value of the first order correction for the ionospheric delay.

In figures 3 and 4 we have plotted this ionospheric delay for satellite 11, for the L_1 and L_2 frequencies respectively.

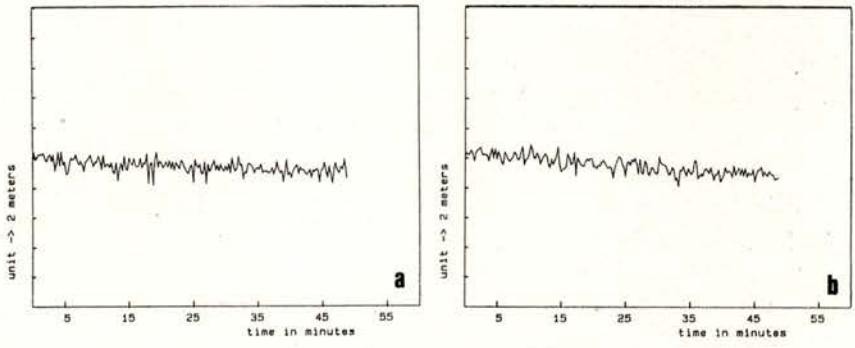

Fig. 4 — Relative ionospheric delays for frequencies L_1 (4a) and L_2 (4b)

We can see that this is a very 'noisy' quantity, with an r.m.s. reaching several meters, and that the delay is of course bigger in the L_2 frequency. Due to problems with the reception of the signals, we have used only a part of the data, where no interruptions occur, covering a small time interval. Neverthless,

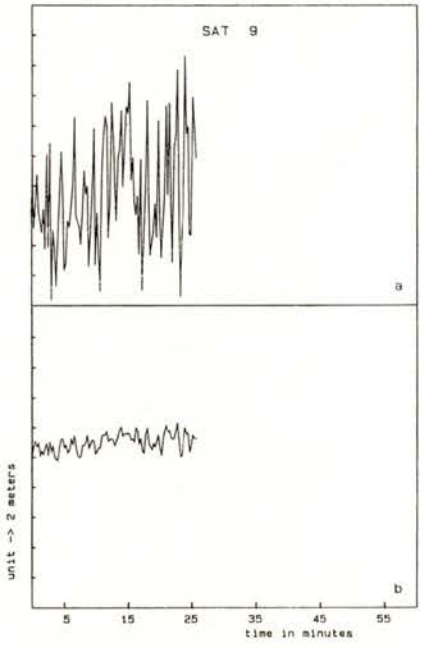

Fig. 5 — Absolute (5a) and relative (5b) ionospheric delay

analysing the global trend we recognize a decrease of the time delay, expressed in meters, which is in agreement with the increase of the satellite elevation angle during that observational period. In figure 5a we have plotted the ionospheric delay for satellite 9, observed from another station, at a slightly later time. The increase of the observed values again agrees with the decrease of the satellite elevation angle.

The short period variations shown in the figures are due to multipath effects (Klobuchar [10]), another problem to be solved but that is outside the scope of this article.

Taking into account the time of the year (Klobuchar [11]) and the hour of the day when the observations took place we recognize the importance this effect may have in the final accuracy of the measured station-satellite range.

Accordingly to Klobuchar [12] the residual error after this first order correction, computed as above, is around 2 meters, still too big for the purpose of very precise positioning.

4.3 – Profiting from the fact that with code frequency receivers we can have measurements on the carrier and on the modulation of that same carrier, the structure of the GPS signals can be used to compute epoch to epoch changes in the ionospheric delay [9].

The ionosphere is responsible for a phase advance on the carrier and a group delay, of the same amount, on the modulation.

Using the code modulation we can compute the station-satellite range at two epochs and measuring the carrier phase at the same epochs we can have the correspondent change in range. As the ionospheric effect is the same, with the opposite sign, for both code and carrier, we can write:

$$D = 1/2 \left[\rho_j^i (t_k) - \rho_j^i (t_{k-1}) \right] - \int_{t_{k-1}}^{t_k} \rho \, dt$$

Although this expression gives only relative values of the ionospheric time delay, it has the advantage of requiring only one frequency. In order to compare this method with the previous one we have plotted D, for the same satellites, in figures 3b, 4b and 5b. We can see that the noise level is much smaller. As this technique, based on the group delay/phase advance, is more accurate to compute the epoch to epoch changes of the ionospheric delay, we may combine it with the dual frequency technique, referred in 4.2, to improve the final accuracy of the determination of the effect of the ionosphere.

4.4 – Another way of analysing the ionospheric behaviour and determining its effect on GPS observations is suggested by MacDoran [13]. The method is referred to as SLIC (Satellite L-band Ionospheric Calibration) and is based on the measurement of the time interval between code transitions in two frequencies.

It can be used by dual frequency code or codeless receivers users, to compute the Total Electron Content in the line of sight dirction.

The observable group delay between L_1 and L_2, as we have seen, is given in nanoseconds by:

$$\Delta T = \delta t_2 - \delta t_1 = (40.3/c)\ N_t\ [1/f_2^2 - 1/f_1^2]$$

For the GPS frequencies this expression may be rewritten as:

$$\Delta T = 3.5\ N_t\ , \qquad (4.4.1)$$

where N_t is TEC in units of 10^{17} el/m^2:

This method allows TEC measurements with an accuracy of a few times 10^{15} el/m^2 and according to Royden [15], the results are in good agreement with Faraday rotation measurements.

Although this method has disadvantages concerning equipment and reduction procedures, it offers some advantages over Faraday rotation: better distribution of the measurements in time and space, better accuracy and no phase ambiguity. Adittional advantage for the GPS user results from the fact that no knowledge of the P-code is necessary and he still can take advantage of the dual frequency emission. As we have noticed before, the P-code may not be accessible to civilian users in the near future.

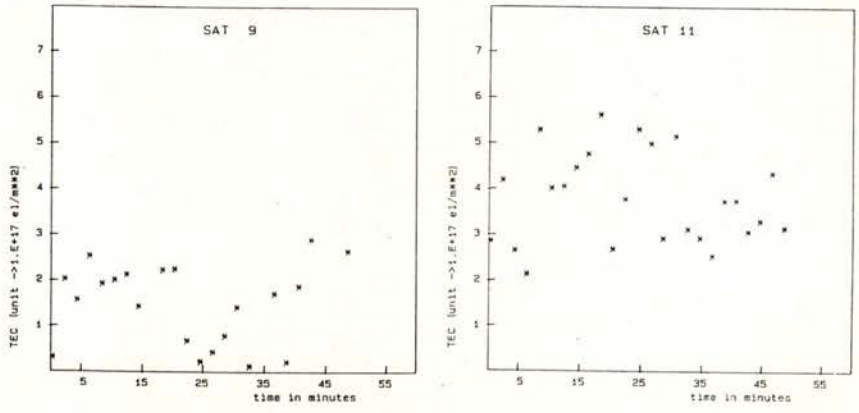

Fig. 6 — TEC (total electron content) in the lign of sight direction for satellites 9 and 11

Since the observations we have were taken with a code receiver we have used (4.2.1) and (4.2.2) to compute the delay in L_1 and L_2 and (4.4.1) to calculate TEC, for satellites 11 and 9 observed from the same station. Figure 6 show the values of TEC computed with a two minute interval. We can see the high rate of change of TEC whose values are almost double for satellite 11, which has a lower elevation angle. This is in agreement with what we have said in paragraph 3. Note that a value of 5.10^{17} el/m^2 induces an error of about 10 m in distance measurements with the L_1 frequency.

5 – CONCLUSIONS

A deeper analysis is needed of the effects of the ionosphere on GPS observaitons. For that more data, taken at different times and under different conditions, are needed. Nevertheless, from what has been said some conclusions can be drawn about the role of the ionosphere on GPS baseline measurements and about the role of GPS data for the development of ionospheric models.

Ionospheric effects on GPS observations can be dealt with in different ways. Besides the direct computation of ionospheric parameters, as we have described, some attempts have been made to remove this effect from GPS observations using different combinations of the observed phase, such as suggested in paragraph 4.1. For baseline determination between close stations, the ionospheric effects cancel out when differencing the observations, due to the correlation of the ionospheric behaviour with earth location. This correlation can also de used in dynamic applications where one of the stations is fixed, and may have difficulties in computing ionospheric parameters relatively to the other, more affected by other kinds of perturbations due to its motion.

Much work is still needed to improve accuracy in the determination of ionospheric effects on GPS observations. According to Lachapelle [6], the ionosphere is responsible for errors of the order of 1 p.p.m. (or greater) in baseline measurements. Using GPS to measure long baselines (some hundreds of kilometers), with an accuracy of 0.1 p.p.m. will still be a challenge, even for the dual frequency user, demanding an improvement of the existing ionospheric models.

On the other hand it must be emphasized that GPS data can play a decisive role on the improvement of those models because it is well distributed all over the world and will be available at different epochs and under a variety of geophysical conditions. TEC measurements can be better carried out using GPS data, and considering that the number of satellites still available for Faraday rotation measurements is decreasing, GPS can be seen as an alternative solution.

Prilepin [16], also pointed out the superiority of GPS information for the determination of the two major terms of the integral ionosphere refraction index and the correction for the bending of the trajectory.

In view of the results obtained so far with GPS, and keeping in mind that a lot of work is still being done concerning precise orbit determination and modelling of propagation effects, a significant improvement is to be expected when the system is in full operation in the early nineties.

The collaboration of the Institute of Astronomical and Physical Geodesy of the University FAF Munich, is grateful acknowledged for allowing the use of the GPS data, collected by researchers of the Institute.

REFERENCES

[1] EVANS, A. et al., «Collocation tests of an advanced geodetic Global Positioning System Receiver», *Proceedings of the First Internacional Symposium on Precise Positioning with GPS*, Rockville, 1985.

[2] GOAD, C., «Precise Positioning with the GPS», *CERN ACCELARATOR SCHOOL*, Geneve, 1986.

[3] DAVIDSON et al., «Global Positioning System — Differential positioning simulations», *Technical Report n.° 90*, Department of Surveying Engineering, University of New Brunswick, 1983.

[4] CLYNCH, C. et al., «Evaluation of ionospheric residual range error model», *Proceedings of the Third International Geodetic Symposium on Satellite Doppler Positioning*, New Mexico, 1982.

[5] LACHAPELLE et al., «Single and dual frequency GPS results for baselines of 10 to 500 km», *The Canadian Surveyor*, Vol. **40**, n.° 2, 1985.

[6] KLEUSBERG, A., «Ionospheric propagation effects in geodetic relative GPS positioning, *Manuscripta Geodaetica*, Vol. **11**, 1986.

[7] SPILKER, J., «GPS signal structure and performance characteristics» Institute of Navigation, 1980.

[8] BASTOS, L. et al., «Fixing cycle slip in Kinematic positioning with GPS, using Kalman filtering» (submitted to Manuscripta Geodaetica, July 1987).

[9] JORGENSEN, P., «Ionospheric measurements from Navstar satellites», *Technical* Report, Aerospace Corporation, El Segundo, California, 1978.

[10] KLOBUCHAR, J. A., «Multipath effects on the determination of absolute ionospheric time delay from GPS signals», *Radio Science, Vol.* **20**, n.° 3, 1985.

[11] KLOBUCHAR, J. A., «A first-order prediction model of Total Electron Content group path delay for a mid latitude ionosphere», Air Force Cambridge Research Laboratories, 1970.

[12] KLOBUCHAR et al., «A Preliminary Evaluation of the two frequency ionospheric correction for the NAVSTAR/Global Positioning System», AGARD-CP-284, 1979.

[13] MACDORAN et al., «SERIES: Satellite emission range infarred earth surveying», *Proceedings of the Third International Geodetic Symposium on Satellite Doppler Positioning*, New Mexico, 1982.

[14] ROYDEN et al., «Comparison of NAVSTAR satellite L-band ionospheric calibrations with Faraday rotation measurements», *Radio Science*, Vol. **19**, n.° 3, 1984.

[15] PRILEPIN, M. T., «Determination of ionospheric correction by group and phase velocity», *Proceedings of the Fourth International Geodetic Symposium on Satellite Positioning*, Texas, 1986.

AEROMAGNETIC SURVEY OF PORTUGAL
(Southern panel)

MIRANDA, J. M. (1), GALDEANO, A. (2) and MENDES-VICTOR, L. A. (1)

(1) Centro de Geofísica da Universidade de Lisboa
R. Escola Politécnica 58, 1200 Lisboa, Portugal

(2) Institut de Physique du Globe de Paris
Tour 2425, 4 Place Jussieu, Paris, 75004, France

(Received 13 July 1987)

ABSTRACT — The Aeromagnetic Survey of Portugal here presented makes possible a high precision mapping of the magnetic anomalies due to crustal heterogeneities. The separation of the measured field into a deep, or normal, part and a shallow one, is achieved by the IGRF80 model. The final magnetic anomalies show a remarkable correlation with the major regional features and the main geological structures.

Data presented here concern only the southern panel of the survey. Flight operations were made in 1978.

1 – INTRODUCTION

The Instituto Nacional de Meteorologia e Geofísica (INMG), in collaboration with the Centro de Geofísica da Universidade de Lisboa (CGUL), planned and executed the Aeromagnetic Survey of Portugal. Their purposes were the accurate mapping of the geomagnetic elements over Portugal and the identification of the magnetic signature of the main structural features in the territory.

Flight operations were carried out by the geophysical team of the Portuguese Air Force with a Geometrics G803 proton precession magneometer, and took place in the years of 1978 (southern pannel) and 1981 (northern pannel).

Magnetic base stations, also equipped with proton magnetometers were maintained by the INMG in Beja, Tomar and Vila Real in order to provide efficient time reduction of measurements.

Final control of secular variation was achieved by comparison with Magnetic Observatory of Coimbra University.

Data processing took place in the INMG, the CGUL and the Institut de Physique du Globe de Paris, in the framework of the collaboration between the three institutions.

The aim of this work is to present the technical characteristics of the survey with particular emphasis on the main options taken by the authors in all different stages of data processing.

The processing of each panel originated different problems particularly because there is a 3 year time gap between them and also because some differences did exist between field operations methodology for each pannel. So, we decided to discuss and present first the southern pannel, together with its total intensity map for the 1979.0 epoch and its associated anomalies. In a later paper we shall present the northern panel and the final geomagnetic maps.

2 – GENERAL CHARACTERISTICS OF THE AEROMAGNETIC SURVEY

The initial planning of the survey divided the portuguese territory in two panels (here named «southern panel» and «northern panel»). The flight line directions follow the magnetic meridians, 10 Km apart, and numbered from 1 (at west) to 34 (east).

Every 40 Km a tie-line was flown, perpendicularly to the flight lines and numbered from 37 (at the north) to 51 (at the south). Fig. 1 shows the general planning scheme.

The measurement of the geomagnetic field was made with a proton procession magnetometer operating with 1 sec sampling rate, corresponding to near 70 m spacing over the terrain.

The mean flight height was 10 000 feet (approximately 3 000 m) and was controlled by a barometric altimeter.

The horizontal position of the measure points was calculated from aerial photographs, taken every 10 seconds and synchcronized with the magnetometer.

A total of 34 flight hours took place, corresponding to approximately 6 700 Km of geomagnetic profiles used for the processing.

From all the lines executed by the Air Force the only ones which were discarded were those aborted during operation and the tie-line 51, because its spatial restitution was considered not reliable.

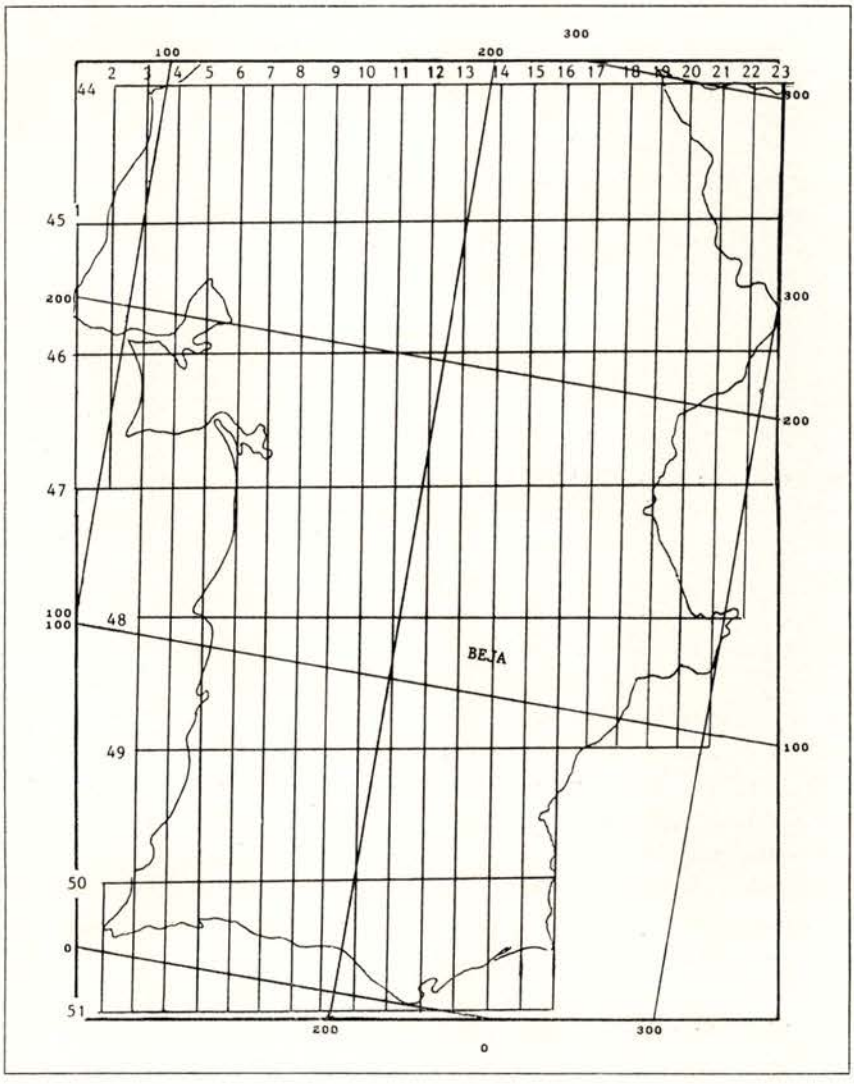

Fig. 1 — Planning of the L. A. P. C. The tie-line 45 divides the northern from the southern pannel. The reference station for the southern pannel was located in Beja.

3 — SYNTHESIS OF MAIN PROCESSING STEPS

One tenth of the total amount of the photographs executed by the aircraft equipment was geometrically restituted after identification of the sharp features on 1:25000 topographic maps.

The coordinates of the geometrical centres of the photos were sampled and then plotted for validation.

Above the sea, in the areas important to assure a clear definition of the geomagnetic field a careful extrapolation was made based upon the stability of the aircraft movement.

The coordinates of all the measurement points were then calculated by interpolation with cubic splines.

3.1 — *Processing of magnetometer records*

The magnetic tape content, recorded by the plane equipment, includes: (i) code designation of flight line, (ii) sequential numbering of the measurement, (iii) magnetic field's intensity (nT), (iv) day, (v) measurement time with 1 sec precision, and (vi) barometric altitude. Besides this relevant information, other fields were also recorded but we will not consider them in our work.

All the files were filtered with a symmetrical 11 point cosinusoidal, filter and then sampled at 1/10 of the original measurement points. The mean spacing between field values retained is approximately 700 m. This value, when compared with the mean flight height (3 000 m) assures the retention of all relevant magnetic information. The sampling points were also chosen so that they correspond to the photographs really identified.

The filtered field values and geographical coordinates of each measurement point were added into the magnetic tape records.

3.2 — *Reduction stations processing*

The time reduction of field data was essentially based upon the instantaneous comparison between field measures and the reduction station. So, we must be able to know the (annual) mean

field values for each reduction station and we must also be sure that the daily geomagnetic variation is homogeneous for all the panel covered by each station.

The determination of the geomagnetic annual mean field for the reduction station is usually accomplished by the comparison with a permanent magnetic observatory, from which mean values are already known. This is done by the determination of a mean value for the difference between daily magnetic field values at both stations. The difference can also be calculated from measurements at very quiet hours.

Unfortunatelly, the Beja reduction station was not in operation during the night and so we needed to establish an alternative method for an effective calculation of its mean annual field.

The analogic records for the Beja and Coimbra stations were digitized and sampled with a 100 sec constant step. Then we made the assumption that, for each day *d*, the time variation at both stations should be related by an expression of the form:

$$B = F * C$$

where B and C have the following components:

$$b_i = \overline{T}_B^d - T_B\ (t_i) \qquad c_i = \overline{T}_C^d - T_C\ (t_i)$$

The filter F can be calculated in a least squares (LS) sense ($\| B - F * C \| = \min$). However, while $\overline{T}_C^d$ is a known value, $\overline{T}_B^d$ is not and, in this step, is our true unknown.

The calculation process starts with a first guess for $\overline{T}_B^d$ (determined from the true measurement records). This allows a first choice for the filter coefficients f_i from the LS procedure

$$\sum_{m=1}^{NTF} f_m \left[\sum_{n=1}^{NP} c_{n-m+NTF}\ c_{n-q+NTF} \right] = \sum_{n=1}^{NP} (c_n\ b_{n-q+NTF})$$
$$(q = 1, \ldots, NTF)$$

where NTF and NP are, respectively, the dimensions of the filter and the real data segment.

Then, we can «reconstruct» Beja values from Coimbra measurements and so we will get another guess for $\overline{T}_B$; the process is then repeated until we can verify a convergence on $\overline{T}_B^d$ values.

The typical results obtained for the prediction error DF are shown in Fig. 2. We were able to find convergence for every day of the survey.

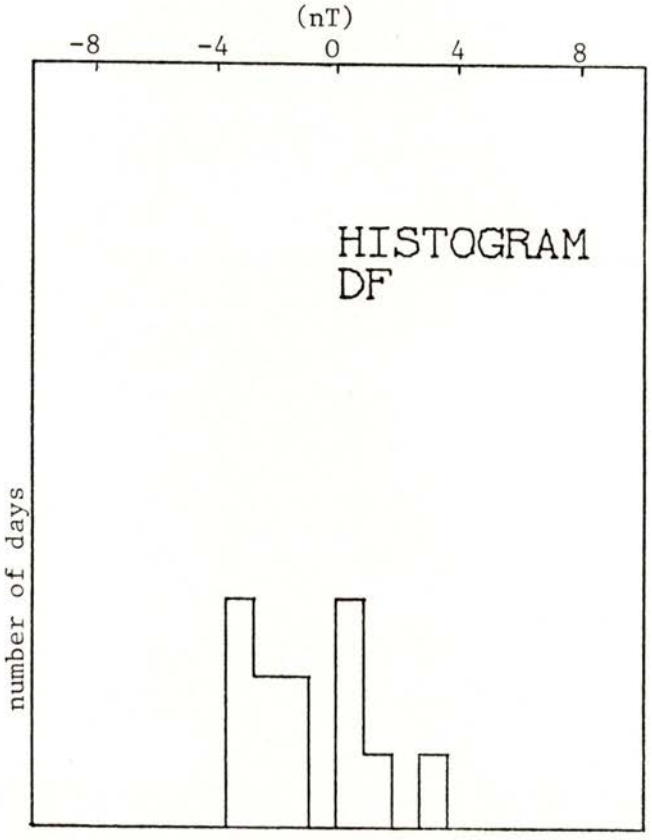

Fig. 2 — Differences between the true daily mean for Coimbra Observatory and the predicted Beja station values.

After applying this methodology to all surveying days we concluded that for all values of d, the differences between daily mean values at Coimbra and Beja are all included in the interval

$$\overline{T}_C^d - \overline{T}_B^d = (790 \pm 4)\ \text{nT}$$

The estimated daily differences distribution is shown in Fig. 3.

Coimbra mean annual value for 1979.0 epoch is 44094 nT. Thus we can deduce the mean value for the Beja station:

$$\overline{T}_{B,\,1979.0} = 43305 \text{ nT}$$

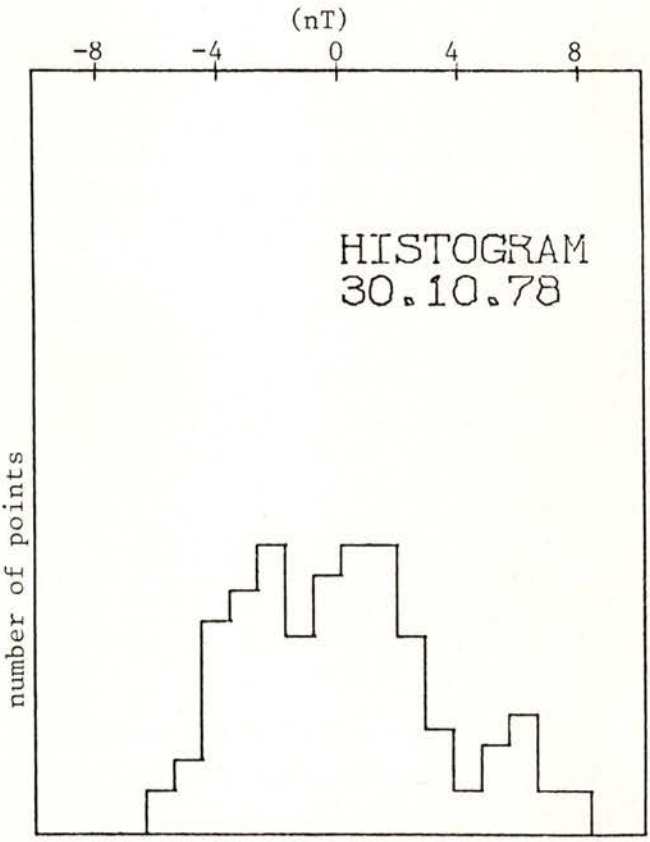

Fig. 3 — Histogram of the prediction error for a typical day (30 Oct. 1978).

Time reduction of the geomagnetic field measurements is then easily determined from the differences ($\overline{T}_B$ (t) − 43305 nT) and applied to all field records.

3.3 — *Flight line levelling*

The effectiveness of time and spatial data reduction is essentially verified by the cross errors between flight lines and tie-lines.

Such errors are mainly related to (i) the conductivity anomalies usually due to geological discontinuites, (ii) localization errors, and (iii) inherent inaccuracy of barometric determination of altitude.

The first source of errors affects both flight and tie-lines but the other two are strongly correlated to the horizontal and vertical gradients of the field. The tie-lines must be flown in geomagnetic quiet days and some of them were repeated.

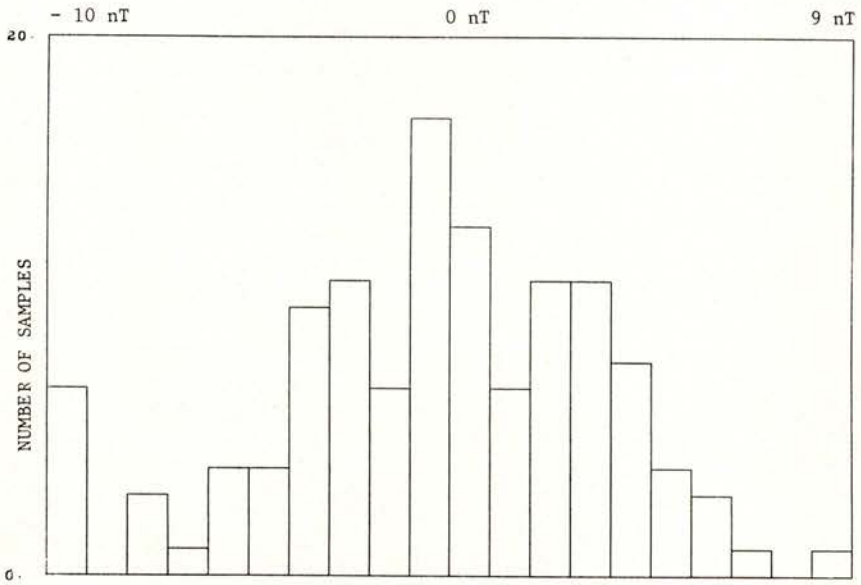

Fig. 4 — Cross error distribution (nT). All flight lines were forced to have null mean cross errors.

The methodology followed in the detection and elimination of cross errors included the following steps: (i) automatic determination of the coordinates of the cross point between each flight

line and all tie-lines, (ii) linear interpolation between the four relevant points for the determination of the error «tie-line minus flight line», (iii) constant correction of each tie-line from the mean cross error with all the flight lines, (iv) final correction of each flight line supposing that the error could be expressed by a cubic spline.

In Fig. 4 we show the histogram of cross errors for the southern panel. A small quantity of high values is related to high horizontal gradient both in the geomagnetic field and the topography or to very particular radio-electrical phenomena that cause a phase lock condition in the magnetometer. In low gradient areas the errors are always small.

3.4 — *Flight line regularization*

The spatial distribution of data points does not match with the previously planned grid and corresponds to equally time sequences rather than to spatial ones because the speed of the aircraft does change during the flight. It is then necessary to perform the interpolation of these field values into a regular grid, that will be the basis of the subsequent processing steps.

The methodology develloped by the second author (unpublished) is particularly adapted to aeromagnetic surveys, where data collection is made along profiles. It is divided in the following steps:

(i) elimination of the spikes (if any) over the profile. This filtering is achieved by fitting smoothing splines [1] to the field data. The measure of the global fitting error is then minimized:

$$\sum_{i=1}^{N} \left[\frac{F(x(i)) - y(i)}{dy(i)} \right]^2 < S$$

and so, changes in the values of S and the individual weights dy (i) are then related to the smoothing effect, allowing the control for every situation.

(ii) determination of the optimal location of the regular grid that approximates, in the LS sense, all the coordinates of the data points. This location is mainly characterized

by the coordinates of its east azimuth and the spacing between profiles. The gridded values are then represented by a matrix where the columns correspond to the flight lines.

(iii) projection of the true field data onto the regular grid, first in the direction of the flight lines and afterwards in the direction of the tie-lines. This projection is made with smoothing splines or by Akima splines [2] according to the smoothing effect needed.

The results obtained in the L. A. P. C. are presented in Figs. 5 and 6. We can assume that the filtering level imposed to the aeromagnetic data is very low. Only a small number of points were significantly changed. On the other hand, Fig. 6 shows that only the flight lines 1 and 2 are particularly far from the calculated grid.

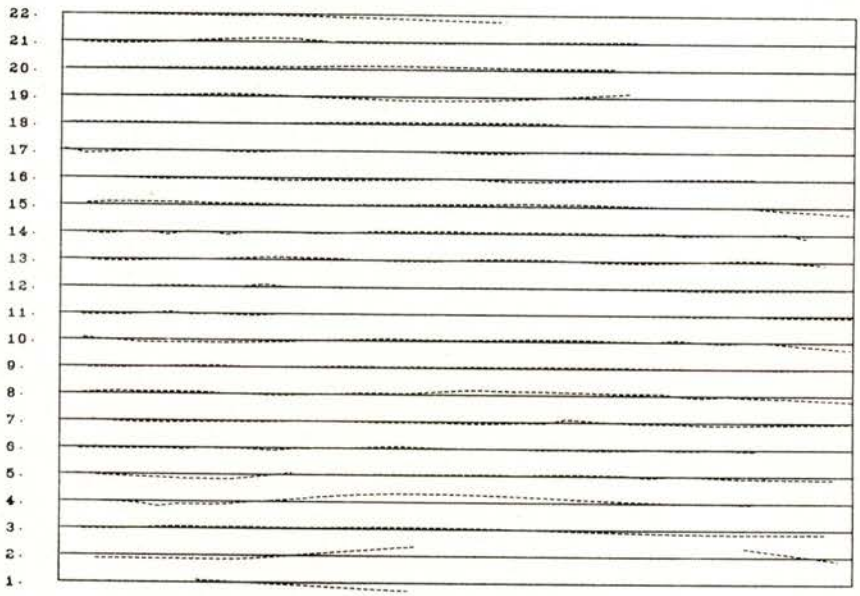

Fig. 5 — Comparison between the true measurement points and grid location.

The final spacing between profiles is 10 Km (the LS value was 10.014 Km) and the east azimuth – 9.8 degrees.

The projection of the flight lines over the regular grid produced a matrix with dimension (304,23) corresponding to a 10 Km spacing between profiles and a 1 Km spacing along each one.

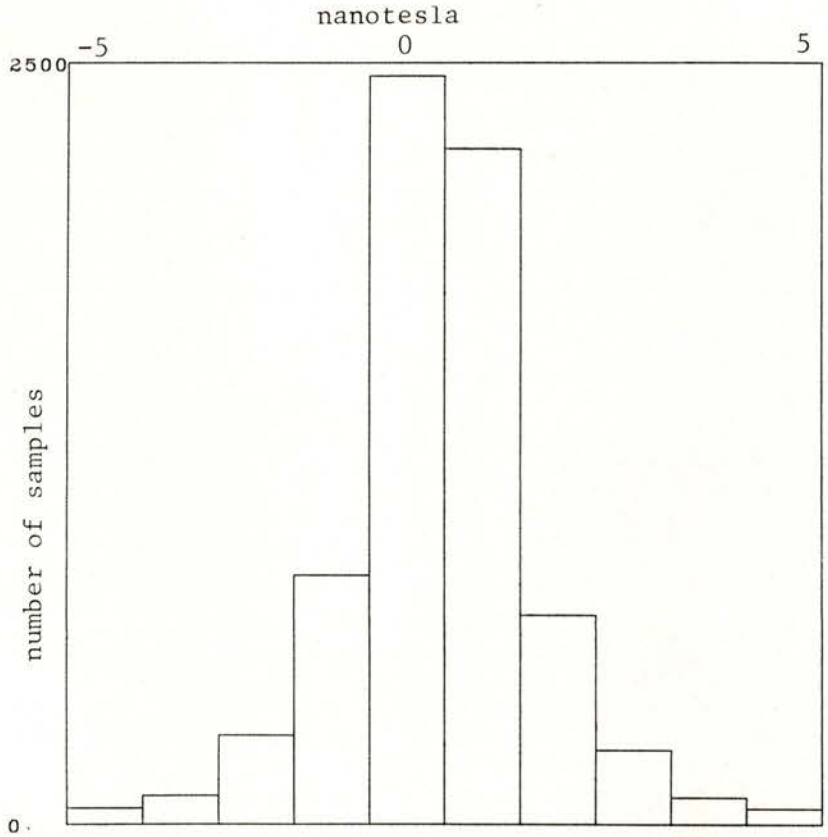

Fig. 6 — Differences between data poins before and after smoothing.

Being aware that the spacing between processed data points was approximately 700 m, the 1 Km spacing between retained values assures the fiability of the final representation of the field.

3.5 — *Magnetic field mapping*

The mapping of the geomagnetic field over the horizontal plane is possible if we can assume a spatial representation that is compatible with field data along the measurement profiles.

The basic assumption made was that the magnetic field could be well represented by two dimensional cubic splines [2] fitting the gridded data. This method was proved to be satisfactory to map the field in several aeromagnetic surveys [3].

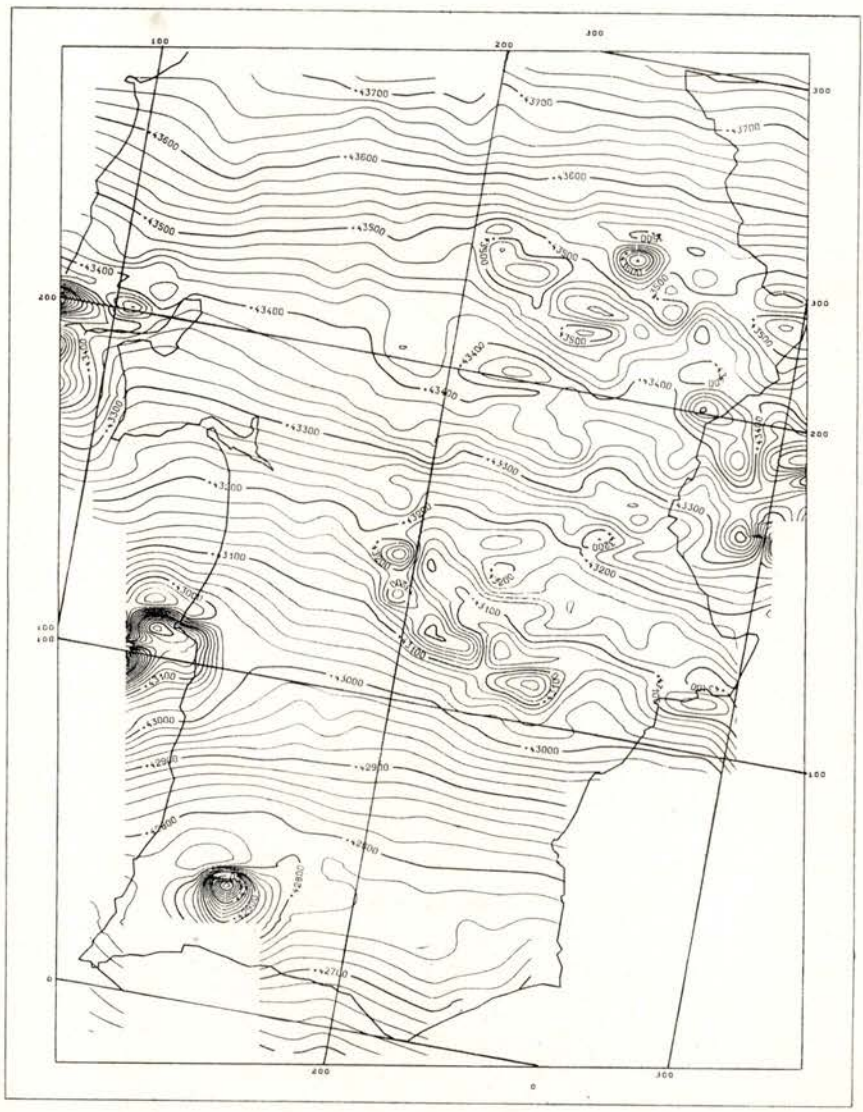

Fig. 7 — Total field map for southern Portugal. Epoch: 1979.0; altutide: 3000 m; equidistance between isovalues: 20 nT.

The aeromagnetic map of southern Portugal for the 1979.0 epoch and the 3000 m altitude is shown in Fig. 7.

4 – NORMAL AND ANOMALOUS COMPONENTS OF THE MAGNETIC FIELD

4.1 — *Polynomial representations*

The total field aeromagnetic map shows a sharp separation between two regions of very different magnetic signatures. The first one corresponds to the Ossa Morena Zone (OMZ) easily identified by the high value of the horizontal gradient, showing an almost perfect delineation of its known geological limits at south, and partially, at west (cf. Ribeiro et al. [4]. The second one corresponds to the South Portuguese Zone (SPZ), where the horizontal gradient is smaller and we can identify three major magnetic anomalies: Monchique, Sines and Sintra, almost aligned, the last two being only partially included in the survey area.

The separation of the measured field into a normal component that must retain the contribution of the deep sources located in the core of the earth, and an anomalous component related to the lateral inhomogeneities of the crust, is strongly constrainet by the dimension of the survey area.

We are then in a situation where it is necessary to determine on one hand if it is possible to calculate a polynomial expression for the main field, as is usually done (Le Mouel [5]; Galdeano [3] and, on the other hand, if the existing global geomagnetic reference fields can successively represent the main field.

The calculation of a polynomial expression for the main field:

$$F^N(x_i; y_i) = \sum_{j=0}^{m} \sum_{k=0}^{n} a_{jk} P_j(x_i) P_k(y_i)$$

can be suitably made with orthogonal polynomials (Le Mouel [5]; Mendes-Victor [6]). Their major advantage relies in the fact that, its coefficients being mutually independant, it is easy to divise

a method for estimating the «best» approximation degree, calculated only from the real data.

The determination of the polynomials was done with the recursion formulae given by Berezin and Zhidkov [7]. The corresponding coefficients were calculated for the gridded data by Grant's method [8]. The measure of the fit of the polynomial expansion is given by the behaviour of the residuals:

$$z^2_{pq} = a_{pq} \| P_p(x) \| . \| P_q(y) \|$$

because they are a measure of the individual contribution to the norm from each polynomial.

—	1923927	1725311	17019	134882	15121	116010	1134	9337
56386115	213299	2345143	65856	140704	60077	298663	41616	
487012	189796	54239	24960	65172	6604	106910	17272	
137044	7447	2290	39821	30872	27952	30719		
8381	20330	41230	2263	20106	3980	23517		
1118	18009	13910	187	47	57478			
12420	18398	20178	11369	27901	3750			
608	6635	106	1425	578				
33134	11129	9652	11007	7409				
10766	707	1154	3659					
55393	21952	648	556					
914	255	61						
20095	8457	82						
326	587							
139	424							
950								
1205								

Fig. 8 — Value of the residuals z^2_{pq} for the lower order polynomials of the expansion of the total field.

The values of z^2_{pq} are partially listed in Fig. 8. We can conclude that there is no sharp discontinuity (mainly in the EW direction) as detected in other aeromagnetic surveys, probably because its lateral extension, when compared to the dimensions

of the major magnetic structures, gives rise to the existence of medium range terms in the polynomial expansion that emphasize the magnitude of the EW transition in the total field map.

These results lead to the conclusion that a planar expression for the normal field could be the most suitable, being the least sensitive to regional features. The explicit determination of the coefficients was done with all the original data, by a robust LS procedure. Its values are:

$$F^N(x, y) = 43758.7 - (x - 200000) \times 0.122432734 \times 10^{-3} + (y - 300000) \times 3.7333213882 \times 10^{-3} \text{ nT}$$

where $(x - 200000)$ and $(y - 300000)$ represent the value (in meters) of the national Hayford Gauss coordinates referred to the Cartographical Central point of Portugal. The choice of the origin of the planar model coordinates is the most adequate because it will be the origin for the polynomial expansion of the normal field in the north.

4.3 — *Comparison between the IGRF80 model and the planar expression for the main field*

The chosen model for the International Geomagnetic Reference Field was the IGRF80 [9] that corresponds to an expression of the earth's main magnetic field in Schmidt spherical harmonics of degree and order 10, whose coefficients were deduced from Observatory and Satellite data.

The corresponding map for Portugal (epoch: 1979.0, height 3000 m) is presented in Fig. 9. It is very similar to that obtained from the planar model both in the values of the field and its gradient.

However, a closer analysis of both reference fields allows the identification of a «non-planar» component in the IGRF80 that can be easily shown by the corresponding differences map (Fig. 10).

The morphology of the IGRF can be well fitted locally by a second degree polynomial. It might be thought that a parabolic fit of survey data would give a better expression for the normal

field. However (see Fig. 11) this would, once more, be severely influenced by the lateral limitations of the survey.

Being aware that the IGRF80 gives the possibility of combining the local fit of the data with the constraints introduced from the

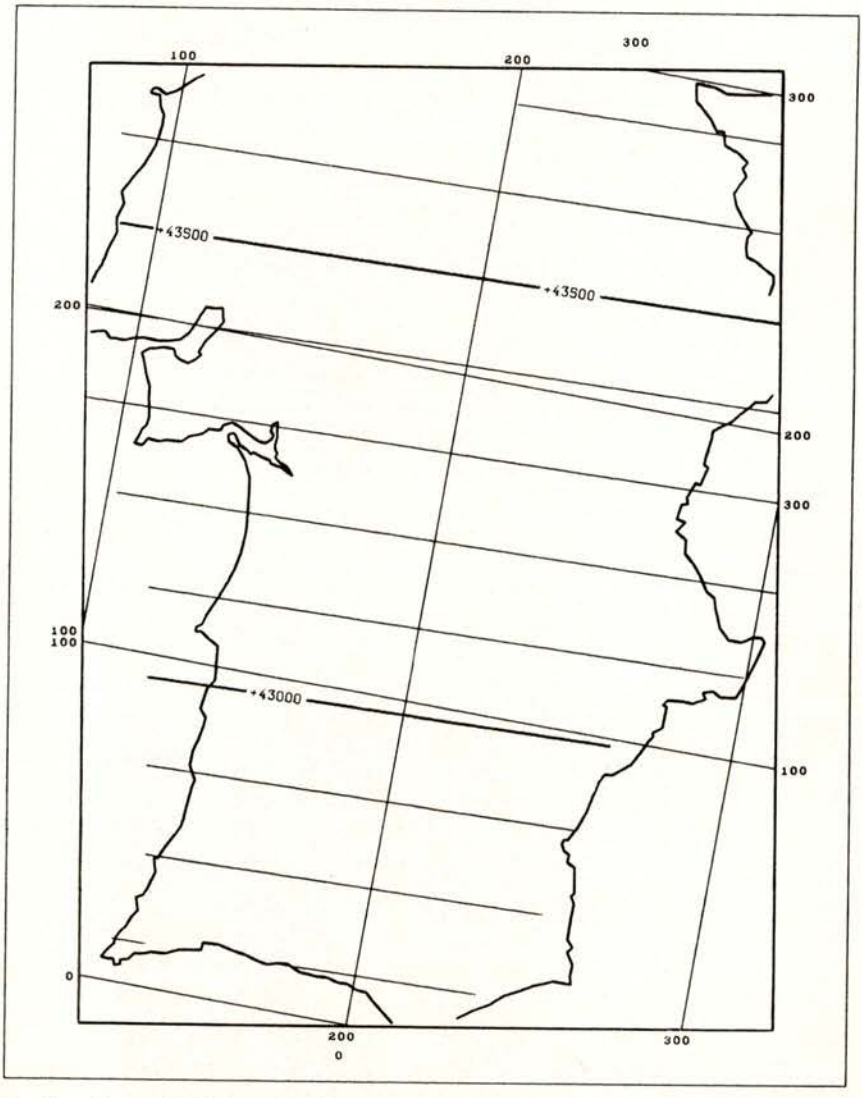

Fig. 9 — Normal fields deduced from IGRF80 (a) and plannar approximation of the survey data (b). Isovalues are plotted every 100 nT.

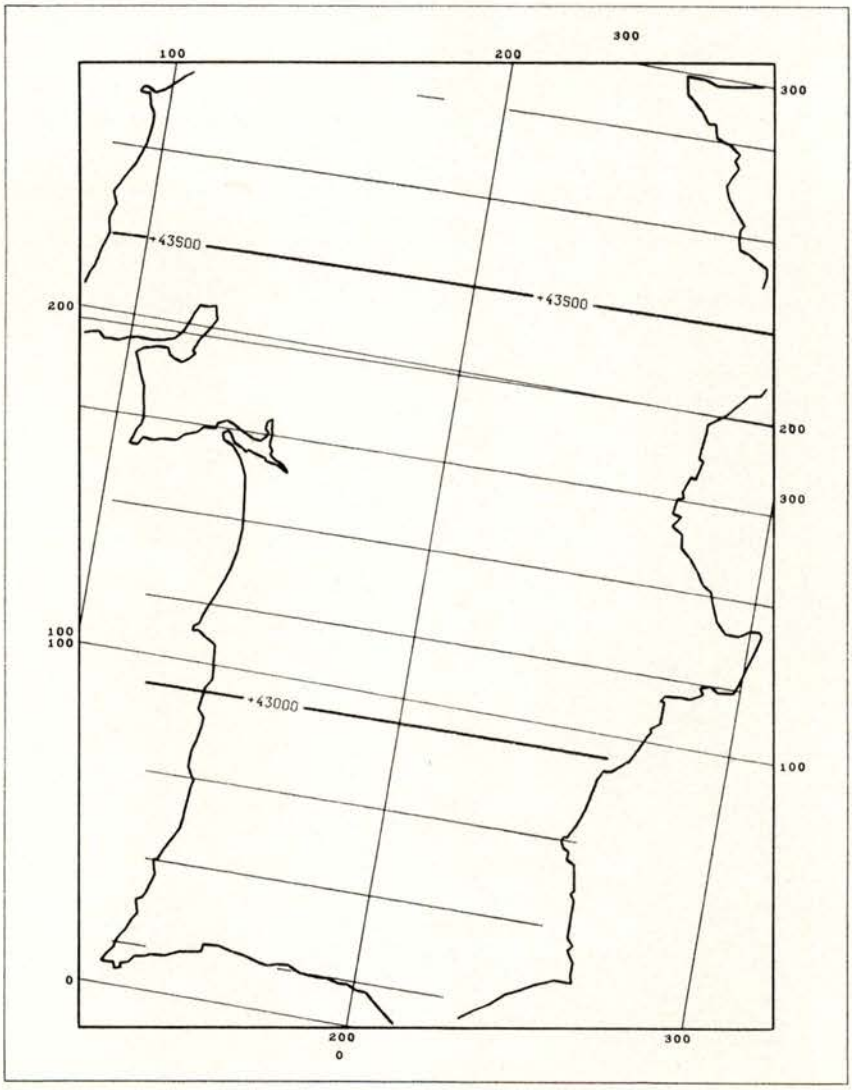

Fig. 9 (b)

analysis of the global main field, it is better to use the IGRF80 to define the normal field. The only slight change that must be done in this representation is to subtract 17 nT from IGRF value, in order to achieve a null mean over the area covered by the survey.

The map of the total field anomalies is presented in Fig. 12. The observations made concerning the total field map are now more obvious. The boundaries of the OMZ and SPZ are magnetically sharp, the SPZ being mainly characterized by small/medium range wavelength magnetic anomalies, and the OMZ being an anomalous

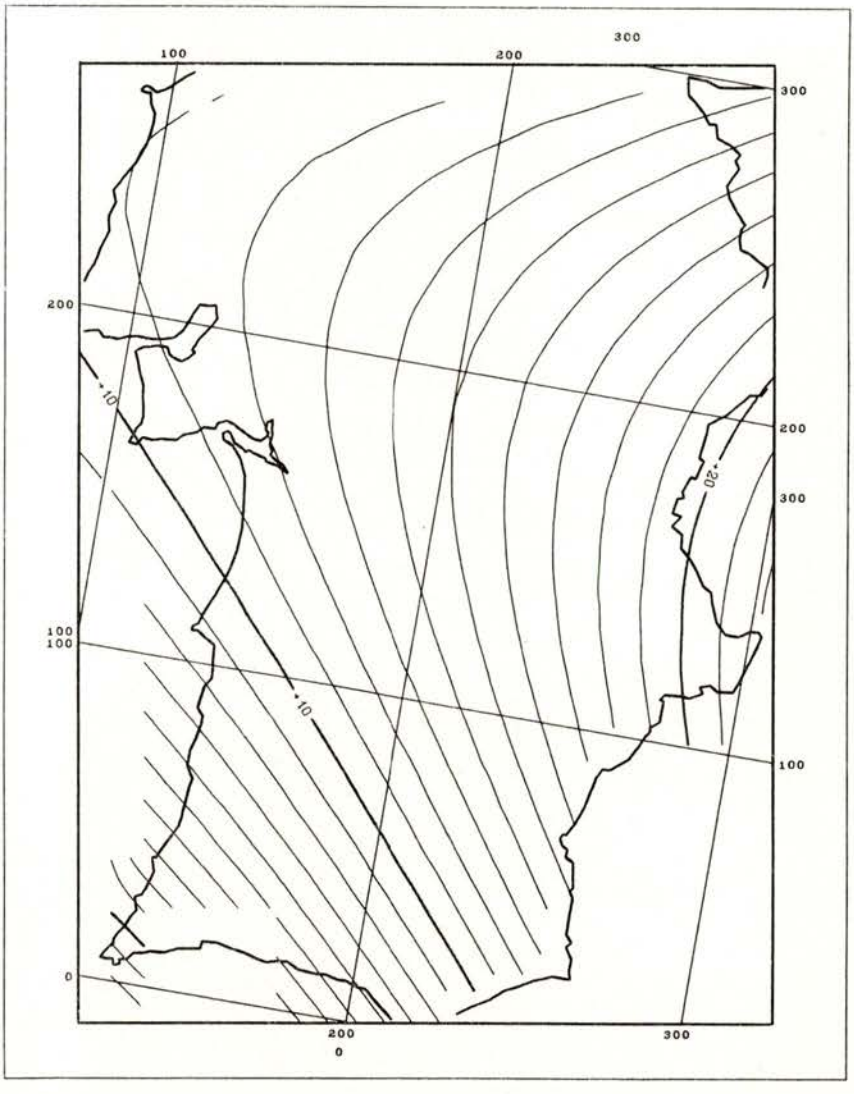

Fig. 10 — Differences (nT) between IGRF80 and the plannar model.

area, with various small wavelength anomalies, surely related to shallow magnetic structures.

The morphology of the anomalous total field, and in particular the location of the zero anomaly level seems to confirm the validity of the procedure adopted.

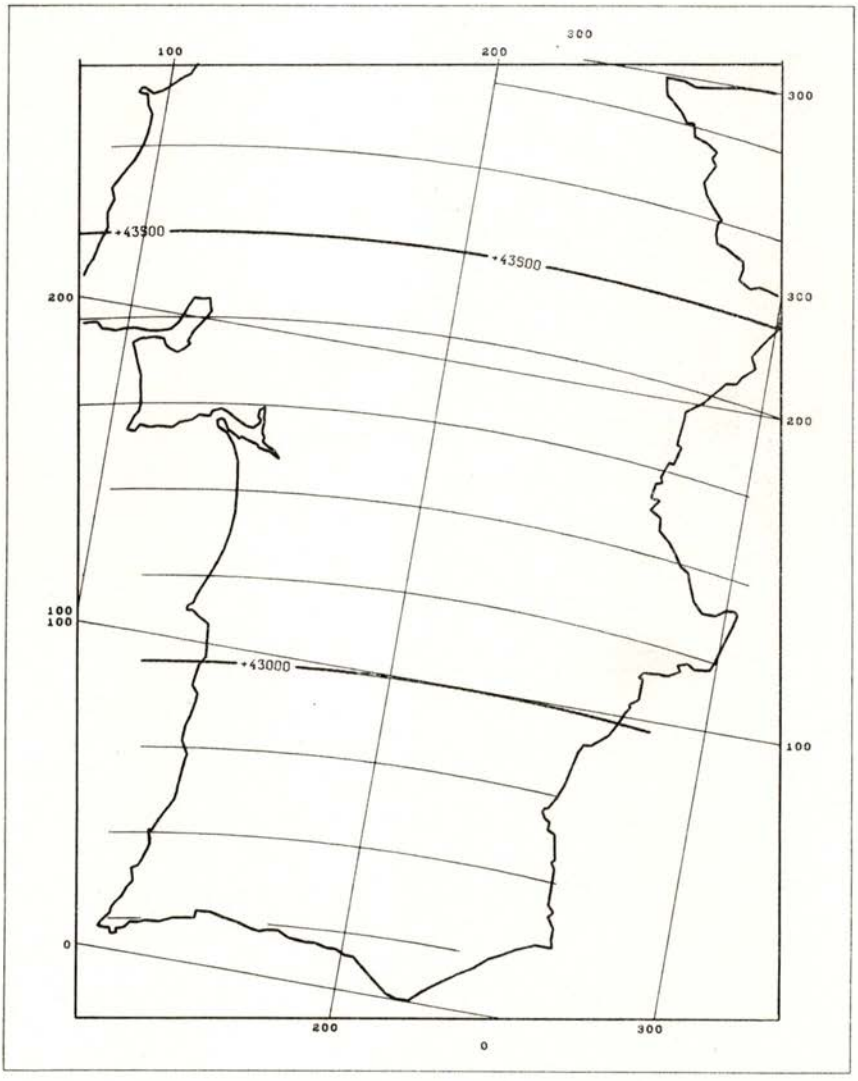

Fig. 11 — Parabolic fitting of survey data. Distance between isolines: 100 nT.

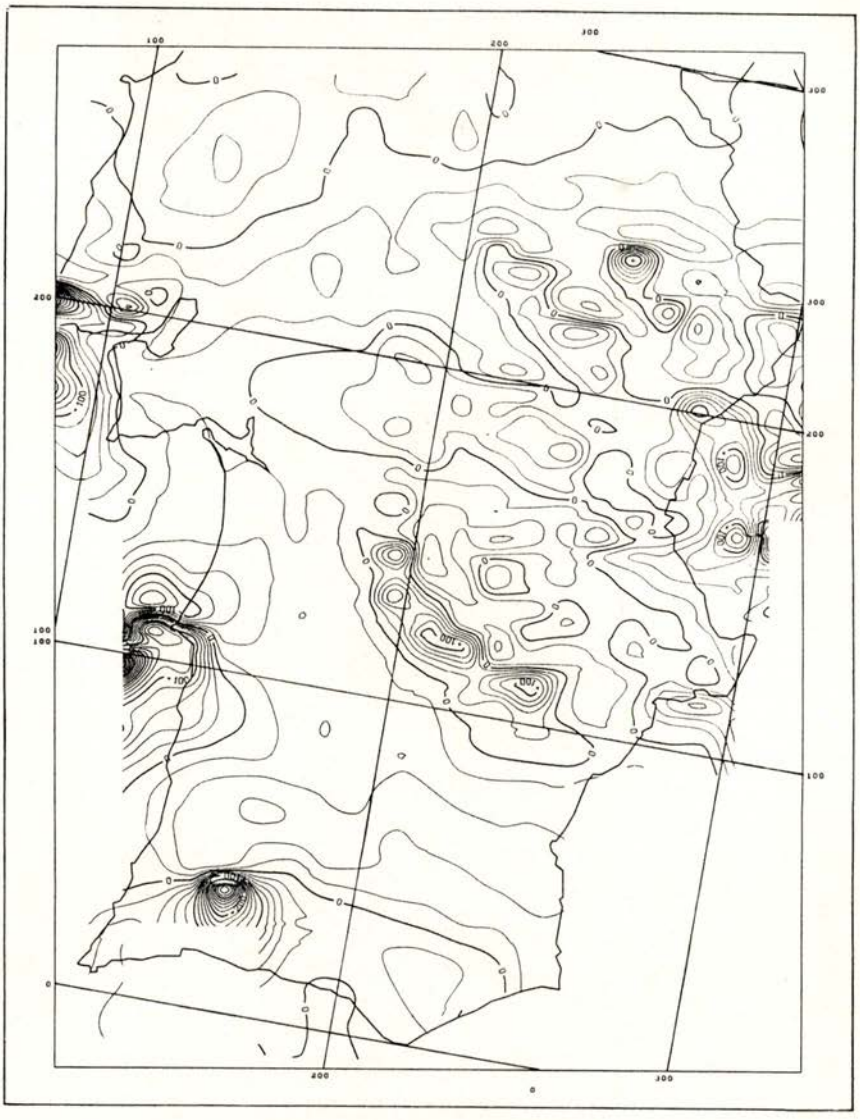

Fig. 12 — Total field anomalies map for southern Portugal (nT).

5 - ACCURACY

The main sources of error have been pointed out already. These include errors due to field measurement, to the uncertainty in the location of the measurement points, and to the time reduction

methods employed. In the last category we must also distinguish between the errors due to the calculation of the Beja mean annual field value and those due to the non-homogeneity of the diurnal variation over the survey area.

The proton precession magnetometer assures a nominal precision of 1 nT. From the smoothing effect (see Fig. 5) we can estimate a maximum of 2 nT for this component of the noise.

Location errors in the horizontal coordinates are small over land (of the order of 50 m) but can be larger over the sea. For seriously anomalous areas (horizontal gradient greater than 20 nT/Km) this can originate an error of 1 or 2 nT over the land. It is surely greater over the sea.

The errors due to the set of the annual mean value for Beja station can be roughly represented by the dispersion of the daily differences (cf. Fig. 2) which is about 4 nT.

The uncertainty in the flight height and in the non-homogeneity of the diurnal variation can only be indirectly estimated by the cross errors between flight and tie-lines.

The final accuracy of the survey can be estimated as ± 10 nT. It must be emphasized that the major part of this uncertainty is a smoothly varying quantity that was distributed along the lines during the reduction process, and so will mainly affect the greater wavelengths presented in the map.

6 — CONCLUSIONS

The aeromagnetic survey of Portugal, the southern pannel of which was here analysed, is intended to be a reliable basis for the design of crustal models.

The authors hope that it will be possible to establish an adequate representation of the main and the crustal magnetic fields for the Portuguese territory after the conclusion of the northern pannel of the survey. The correlation between geology and magnetic behaviour, which is already apparent in the presented maps, demonstrates the importance of this survey as a tool for understanding the deep geology of Portugal.

This work is a result of a great number of individual contributions as the processing of an aeromagnetic survey involves an intimate collaboration between the flight and the observatory operations, the photo identifications and all the other processing techniques. The authors are most indebted to all the personnel of the INMG, in particular to I. Abreu, M. A. Baptista and M. L. Contreiras, and to the geophysical team of the Portuguese accomplishment of the survey.

We wish also to thank Dr. Le Moüel, Director of the Geomagnetism Laboratory of the IPGP, for all the material collaboration that was essential to this work.

REFERENCES

[1] REINSCH, C. H., «Smoothing by spline functions» *Num. Nath.*, **10**, 177/183 (1967).

[2] AKIMA, A., «A new method of interpolation and smooth curve fitting based on local procedure»s. *Journ. ACM*, **17**, n.° 4, 589/602 (1970).

[3] GALDEANO, A., «La cartographie aeromagnetique du sud-ouest de l'Europe et de la region afar. Realisation, methodes de traitment, applications geodinamiques». Thesis presented to the Université de Paris VII (1980).

[4] RIBEIRO, A. et al., «Introduction a la Geologie Generale du Portugal». Serviços Geológicos de Portugal (1979).

[5] LE MOUEL, J. L., «Sur la distribution des elements magnetiques en France». Thesis presented to the Faculté de Sciences de l'Université de Paris (1969).

[6] MENDES-VICTOR, L. A., «L'interpretation des mesures gravimétriques magnetiques aux îles du Cap Vert et la théorie de l'expansion des fonds océaniques». Thèse Docteur-ès-Sciences Physiques — Université de Strasbourg, 198 p. (1970).

[7] BEREZIN, I. S., ZHIDHKOV, Z. P., «Computing Methods». Pergamon Press, London (1965).

[8] GRANT, F., «A problem in the analysis of geophysical data». *Geophysics*, **XXII**, 309/344 (1957).

[9] PEDDIE, N., «International Geomagnetic Reference Fild: The third generation». *J. Geom. Geoel.*, **34**, 309/326 (1982).

Composição, Impressão e Acabamento
na
Imprensa Portuguesa • Rua Formosa, 108-116 • 4000 PORTO

SOCIEDADE PORTUGUESA DE FÍSICA
AV. REPÚBLICA 37-4.°, 1000 LISBOA, PORTUGAL

PORTUGALIAE PHYSICA publishes articles or research notes with original results in theoretical, experimental or applied physics; invited review articles may also be included.

Manuscripts, with an abstract, may be written in English or French; they should be typewritten with two spaces and in duplicate. Figures or photographs must be presented in separate sheets and be suitable for reproduction with eventual reduction in size; captions should make the figures intelligible without reference to the text. Authors are requested to comply with the accepted codes concerning references.

There is no page charge. Author(s) will get 50 free reprints (without covers); these are to be shared among all the authors of the article. Authors interested in more reprints should say so when sending their manuscripts; quotations shall be sent with the proofs.

Subscription rates for volume 18:

3.600 Escudos (US$24) — individuals
9.000 Escudos (US$60) — libraries

PORTUGALIAE PHYSICA may also be sent on an exchange basis; we wellcome all suggestions to such effect.

All mail to be addressed to

PORTUGALIAE PHYSICA
C/O LABORATÓRIO DE FÍSICA, FACULDADE DE CIÊNCIAS
PRAÇA GOMES TEIXEIRA
4000 PORTO PORTUGAL

PORTUGALIAE PHYSICA

VOL. 18 · NUMB 1/2 · 1987

CONTENTS

ISSN 0048-4903 POPYA4 18 (1/2) 1-98 (1987)

PORTUGALIAE PHYSICA

VOLUME 18
FASCÍCULO 3-4
1987

SOCIEDADE PORTUGUESA DE FÍSICA

PORTUGALIAE PHYSICA

Fundada em 1943 por A. Cyrillo Soares, M. Telles Antunes, A. Marques da Silva e M. Valadares

Publicação subsidiada pelo INSTITUTO NACIONAL DE INVESTIGAÇÃO CIENTÍFICA

ISSN 0048 - 4903

PORTUGALIAE PHYSICA

VOLUME 18
FASCÍCULO 3-4
1987

EXPRESSION DU MOMENT MAGNETIQUE ROTATIONNEL DES MOLECULES QUASI-RIGIDES AB_6 DE SYMETRIE O_h

NOÉMIO MACIAS-MARQUES (1) et MARIA LAURA PALMA (1)

Departamento de Física da Faculdade de Ciências da Universidade de Lisboa
et Centro de Física da Matéria Condensada do Instituto Nacional
de Investigação Científica (*), Portugal

JACQUES BORDÉ

Laboratoire de Physique des Lasers, CNRS UA 282,
Université de Paris-Nord, Av. J.-B. Clément,
93430 Villetaneuse, France

(Received 20 April 1988)

ABSTRACT — It is shown that, in the case of rovibrating octahedral molecules, the tensor relating the rotational magnetic moment to the total angular momentum has a simple expression: its nuclear component is a constant and its electronic component is proportional to the tensor $[\mu]$ which appears in the kinetic energy part of the rovibrational hamiltonian.

RÉSUMÉ — On montre que, pour les molécules octaédriques quasi-rigides, le tenseur reliant le moment magnétique rotationnel au moment angulaire total a une expression simple: la partie nucléaire est constante et la partie électronique est proportionnelle au tenseur $[\mu]$ utilisé dans l'énergie cinétique de l'hamiltonien de vibration-rotation.

1 — Introduction

Pour les molécules toupies sphériques dont la configuration d'équilibre possède la symétrie du groupe ponctuel O_h, il est bien connu que, lors de leur interaction avec le rayonnement, les transitions dipolaires *électriques* purement rotationnelles (i. e., à

(1) Une partie de ce travail a été réalisée au cours d'un stage de recherche dans le Laboratoire de Spectroscopie Moléculaire de l'Université Pierre et Marie Curie (Paris - VI), France.

(*) *Adresse:* C.F.M.C. (INIC), Av. Prof. Gama Pinto, 2, 1699 LISBOA CODEX, PORTUGAL.

l'intérieur d'un niveau vibrationnel donné) sont absolument interdites. Cette interdiction trouve son origine dans le fait que la configuration d'équilibre possède un centre de symétrie; et persiste même quand l'on tient compte des effets de non-rigidité, comme l'a démontré J. WATSON [1].

Il s'avère donc intéressant de s'enquérir des possibilités d'existence, pour de telles molécules, de transitions dipolaires *magnétiques* purement rotationnelles, puisque les mêmes arguments de symétrie ne les interdisent d'aucune façon. Nous tenons à souligner que la suggestion originale de cette voie de recherche nous a été donnée par C. BORDÉ [2]. Nous nous y sommes consacrés depuis quelque temps et certains résultats de nos travaux sur ce sujet — concernant le niveau vibrationnel fondamental, avec une application particulière à SF_6 — furent déjà présentés, d'une façon résumée [3] [4].

La présente Note porte exclusivement sur un des problèmes que nous avons eu à résoudre dans ces travaux et que nous préférons traiter séparément.

Le moment dipolaire magnétique moléculaire intervenant dans l'interaction avec le rayonnement peut avoir différentes sources physiques, parmi lesquelles le mouvement de rotation de la molécule détient une place importante. C'est pourquoi notre attention s'est fixée spécialement, tout au début de nos travaux, sur l'étude du *moment magnétique rotationnel moléculaire*, dans le but d'examiner si ce moment pourrait être éventuellement à l'origine d'interactions radiatives produisant un spectre de rotation pure.

Toutefois, tel que l'ont établi ESHBACH et STRANDBERG (dans un travail devenu classique [5]), le moment magnétique rotationnel $\mathbf{m}$ des molécules toupies sphériques, dans leur état électronique fondamental ^1A, reste, pour l'approximation du rotateur rigide, toujours proportionnel au moment angulaire total $\mathbf{J}$. Cette proportionnalité se vérifie soit en ce qui concerne la contribution $\mathbf{m}_{(n)}$ des noyaux, soit en ce qui concerne la contribution électronique $\mathbf{m}_{(e)}$. Or, un tel alignement de $\mathbf{m}$ avec $\mathbf{J}$ entraîne des moments de transition dipolaire magnétique qui sont nuls entre niveaux rotationnels.

Pour tenir compte des mouvements de déformation des molécules, nous avons eu recours à l'expression du moment magnétique rotationnel que l'on peut extraire du terme de Zeeman

dans la formulation récemment développée par F. MICHELOT [6] pour l'hamiltonien effectif d'une molécule semi-rigide non-linéaire quelconque, dans un état électronique non-dégénéré.

Particularisant cette expression générale de MICHELOT pour le cas des molécules toupies sphériques AB_6 avec une configuration d'équilibre octaédrique, qui appartient au groupe de symétrie O_h – nous avons pu montrer qu'elle est, dans ce cas, susceptible d'une certaine simplification.

Dans ce travail, nous démontrons cette simplification et nous mettons en relief les caractéristiques importantes qu'elle possède dans la perspective de nos recherches.

2 — Le tenseur $[\mathfrak{S}]$ reliant $\mathbf{m}$ à $\mathbf{J}$

Le moment magnétique rotationnel, $\mathbf{m}$,

$$\mathbf{m} = \mathbf{m}_{(n)} + \mathbf{m}_{(e)} \tag{1}$$

peut être déduit du terme décrivant l'effet Zeeman rotationnel dans le formalisme de MICHELOT [6]. Il y est relié au moment angulaire total $\mathbf{J}$ au moyen d'un tenseur du 2ème ordre, $[\mathfrak{S}]$, par l'expression

$$\mathbf{m} = \frac{\mu_n}{\hbar}\,[\mathfrak{S}]\,\mathbf{J} = \frac{\mu_n}{\hbar}\,\{[\mathfrak{S}_{(n)}] + [\mathfrak{S}_{(e)}]\}\,\mathbf{J} \tag{2}$$

μ_n étant le magnéton nucléaire (*) (les éléments de $[\mathfrak{S}]$ sont alors des quantités physiques sans dimensions). Dans le système d'axes mobiles [0 xyz], (2) s'écrit

$$m_\alpha = \frac{\mu_n}{\hbar}\left(\mathfrak{S}^{\alpha\beta}_{(n)} + \mathfrak{S}^{\alpha\beta}_{(e)}\right) J_\beta \tag{3}$$

où α et β courent sur (x, y, z) et où la convention d'Einstein est adoptée.

(*) $\mu_n = \dfrac{e\hbar}{2m_p}$ (m_p, masse du proton).

Les expressions générales $\mathfrak{S}^{\alpha\beta}_{(n)}$ et $\mathfrak{S}^{\alpha\beta}_{(e)}$, que l'on extrait de [6], s'écrivent, respectivement:

$$\mathfrak{S}^{\alpha\beta}_{(n)} = m_p \sum_N Z_N \left[\left([I'']^{-1} \right)_{\alpha\beta} \left(\mathbf{r}_N \cdot \mathbf{r}^0_N \right) - \left([I'']^{-1} \right)_{\alpha\gamma} r^{\gamma}_N \, r^{0\beta}_N \right] \quad (4)$$

$$\mathfrak{S}^{\alpha\beta}_{(e)} = - \frac{2m_p}{m_e} \sum_{p \neq 0} {}^{\mu}{}^{\alpha\gamma} \frac{<0 \mid L_\gamma \mid p><p \mid L_\beta \mid 0>}{V_p - V_o} \quad (5)$$

Donnons tout de suite la signification des symboles utilisés dans ces expressions:

(*a*) m_e est la masse de l'électron, m_p celle du proton; Z_N est le nombre atomique du noyau N.

(*b*) $\mathbf{r}_N$ désigne la position instantannée du noyau N, $\mathbf{r}^0_N$ sa position d'équilibre. Rappelons que l'on peut exprimer les vecteurs-position des noyaux comme combinaisons linéaires des coordonnées normales de vibration couramment utilisées, Q_k; on les écrit

$$\mathbf{r}_N = \mathbf{r}^0_N + m_N^{-1/2} \sum_k \mathbf{l}_{Nk} \, Q_k \quad (6)$$

à l'aide de vecteurs constants adéquats, $\mathbf{l}_{Nk}$, m_N étant la masse du noyau N.

(*c*) La matrice [I''], dont l'inverse intervient dans (4), a été conçue dans [7] comme:

$$[I''] = [I^0] + 1/2 \sum_k Q_k \, [a_k], \quad (7)$$

$[I^0]$ étant la matrice $\{I^0_{\gamma\beta}\}$ du tenseur d'inertie à la configuration d'équilibre de la molécule et $[a_k]$ la matrice des constantes $a^{\gamma\beta}_k$ qui peuvent être exprimées par:

$$a^{\gamma\beta}_k = 2 \, \varepsilon_{\gamma\rho\chi} \, \varepsilon_{\beta\mu\chi} \sum_N m_N^{1/2} \, r^{0\rho}_N \, l^{\mu}_{Nk} \quad (8)$$

(où $\{\varepsilon_{\gamma\rho\chi}\}$ représente le tenseur du 3ème ordre de Levi-Civita).

(*d*) La matrice des éléments $\mu^{\alpha\beta}$ — essentiellement dépendants des coordonnées Q_k — représente le «tenseur d'inertie inverse effectif», $[\mu]$, qui figure dans la formulation hamiltonienne de l'énergie cinétique du rotateur vibrant; il se trouve relié aux tenseurs déjà définis par:

$$[\mu] = [I'']^{-1} \; [I^v] \; [I'']^{-1} \tag{9}$$

(tel que J. WATSON l'a montré dans la Réf. [7]).

(*e*) Par V_p nous désignons les niveaux d'énergie électroniques — valeurs propres de l'hamiltonien du problème électronique — et par $|p>$ les états électroniques associés au niveau V_p . V_o et $|0>$ concernent, en particulier, *l'état électronique fondamental.*

(*f*) Enfin, les L_α ($\alpha = x, y, z$) sont les opérateurs composantes du moment angulaire orbital électronique suivant les axes mobiles.

Comme l'on devait s'y attendre, les expressions (4) et (5) constituent bien une généralisation de celles déduites par ESHBACH et STRANDBERG [5] pour le cas du rotateur rigide: on les retrouve si l'on fait, sur (4) et (5), $\mathbf{r}_N \equiv \mathbf{r}_N^0$.

3 — Simplification du tenseur $[\mathfrak{S}]$

Nous allons maintenant montrer que la formulation générale décrite par les expressions (4) et (5) peut se réduire, pour le cas particulier qui nous occupe, à la forme suivante:

$$\mathfrak{S}_{(n)}^{\alpha\beta} = \frac{m_p \, Z_B}{m_B} \; \delta^{\alpha\beta} \tag{10}$$

$$\mathfrak{S}_{(e)}^{\alpha\beta} = -\frac{2 \, m_p}{m_e} \; \mu^{\alpha\beta} \; \mathfrak{L} \tag{11}$$

avec

$$\mathfrak{L} = \sum_{p \neq 0} \frac{|<0|L_\gamma|p>|^2}{V_p - V_o} \tag{12}$$

où γ peut être x, y ou z, indifféremment.

A. Prenons la partie électronique, $\mathfrak{S}^{\alpha\beta}_{(e)}$.

Il nous suffira de montrer que la matrice $\{\mathscr{L}_{\gamma\beta}\}$, définie par

$$\mathscr{L}_{\gamma\beta} = \sum_{p \neq 0} \frac{< 0 \mid L_\gamma \mid p > < p \mid L_\beta \mid 0 >}{V_p - V_0} , \qquad (13)$$

devient, dans notre cas particulier, diagonale et scalaire:

$$\mathscr{L}_{\gamma\beta} \equiv \delta_{\gamma\beta} \, \mathfrak{L} . \qquad (14)$$

Considérons les opérations de symétrie du groupe ponctuel de la molécule dans sa configuration d'équilibre; désignons-les, génériquement, par $\mathfrak{R}$. Ces opérations sont prises en compte comme des opérations agissant sur les axes moléculaires (axes principaux d'inertie de la molécule dans sa configuration d'équilibre).

Nous suivons alors une méthode qui consiste à:

(i) d'une part, discuter en détail quelles sont les transformations qu'une opération $\mathfrak{R}$ quelconque induit sur les diverses entités qui composent l'expression (13) — pour trouver comme résultat *la transformation que devrait subir, par l'effet de* $\mathfrak{R}$, *chacun des éléments de la matrice* $\{\mathscr{L}_{\gamma\beta}\}$;

(ii) d'autre part, tenir compte du fait que, en même temps, *par l'effet de* $\mathfrak{R}$, *la valeur de chacun des* $\mathscr{L}_{\gamma\beta}$ *doit se maintenir inaltérée.*

Pour justifier ce dernier fait, nous dirons qu'il repose directement sur l'hypothèse que les états électroniques (représentés dans (13) par $\mid 0 >$, $\mid p >$,...) sont, dans une très bonne première approximation, indépendants des coordonnées de vibration — dépendant donc exclusivement des coordonnées électroniques (*). On peut de cette façon considérer que les seuls paramètres nucléaires

(*) Cette hypothèse est habituellement admise dans les travaux sur ce domaine. Voir par exemple les Références [6], [8] et [9].

intervenant dans l'expression (13) sont ceux qui se rapportent à la configuration d'équilibre de la molécule. Ainsi, les éléments $\mathscr{L}_{\gamma\beta}$ ne seront liés qu'à cette configuration et la valeur de chacun d'eux reste donc inaltérée, dans la mesure où toute opération de symétrie $\mathfrak{R}$ réalise un recouvrement de la configuration d'équilibre — celle qui définit le groupe ponctuel de la molécule.

Dévellopons donc la méthode déjà annoncée.

(A.1) – Voyons tout d'abord que l'action d'une opération $\mathfrak{R}$ quelconque sur chacun des éléments $\mathscr{L}_{\gamma\beta}$ donnés par (13) peut être analysée au seul moyen de l'étude de la transformation subie par les opérateurs L_γ et L_β. La raison en est que tout se passe comme si les etats électroniques ($|0>$, $|p>$,...) restaient invariants sous l'opération $\mathfrak{R}$.

En effet:

(*a*) Pour les cas qui nous intéressent, car il s'agit de molécules ^{1}A, l'état électronique fondamental $|0>$ est non-dégénéré et totalement symétrique — il est donc invariant dans toute opération $\mathfrak{R}$.

(*b*) En ce qui concerne les états électroniques $|p>$ (avec $p \neq 0$), nous pouvons décomposer la somme sur p en (13), compte tenu des dégénérescences, en sommes partielles dont chacune corréspond aux états $|p_l^{(i)}>$ qui se transforment les uns dans les autres par les opérations $\mathfrak{R}$ et qui sont donc associés à la même valeur propre électronique V_i par une dégénérescence essentielle. Si g_i est le degré de dégénérescence de la valeur propre V_i, on peut écrire

$$\mathscr{L}_{\gamma\beta} = \sum_{i}^{(V_i \neq V_o)} \frac{1}{V_i - V_o} \sum_{l=1}^{g_i} <0 | L_\gamma | p_l^{(i)}> <p_l^{(i)} | L_\beta | 0> \quad (15)$$

et l'on a

$$\mathfrak{R} \, | p_l^{(i)} > = \sum_{l'=1}^{g_i} R_{ll'}^{(i)} \, | p_{l'}^{(i)} > \quad (l = 1,\ldots, g_i) \, ; \quad (16)$$

la matrice $\{ R^{(i)}_{ll'} \}$ étant une matrice unitaire. Alors, le terme générique i de la somme en i, qui constitue (15), se transforme en

$$\frac{1}{V_i - V_o} \sum_{l, l', l''}^{l \text{ à } g_i} R^{(i)}_{ll'} \, R^{(i)*}_{ll''} \, <0 \mid L^T_\gamma \mid p^{(i)}_{l'}> <p^{(i)}_{l''} \mid L^T_\beta \mid 0>$$

si l'on désigne par L^T_α l'operateur transformé de L_α sous l'opération de symétrie $\mathfrak{R}$. Par conséquent, l'expression (15) devient, sous l'effet de l'opération $\mathfrak{R}$:

$$\mathscr{L}^T_{\gamma\beta} = \sum_{i}^{(V_i \neq V_o)} \frac{1}{V_i - V_o} \sum_{l=1}^{g_i} <0 \mid L^T_\gamma \mid p^{(i)}_l> <p^{(i)}_l \mid L^T_\beta \mid 0>; \tag{17}$$

ce qui donne

$$\mathscr{L}^T_{\gamma\beta} = \sum_{p \neq 0} \frac{<0 \mid L^T_\gamma \mid p> <p \mid L^T_\beta \mid 0>}{V_p - V_o} \tag{18}$$

lorsqu'on reconstitue, sur (17), la somme globale (unique) sur tous les p ($p \neq 0$).

Ainsi, effectivement, l'opération $\mathfrak{R}$ transforme $\mathscr{L}_{\gamma\beta}$, donné par (13), en $\mathscr{L}^T_{\gamma\beta}$, donné par (18), comme si l'action de $\mathfrak{R}$ ne s'exerçait que sur les opérateurs L_α.

(A.2) — Notons ensuite que les composantes L_α ($\alpha = x, y, z$) du moment angulaire orbital électronique constituent, par rapport au groupe O_h des molécules en étude, un vecteur du type de symétrie F_{1g}. C'est à dire que, sous l'opération de symétrie générique $\mathfrak{R}$, les composantes L_α vont se transformer suivant

$$L^T_\alpha = D^{F_{1g}}_{\alpha\nu} (\mathfrak{R}) \; L_\nu \tag{19}$$

où $\left\{ D^{F_{1g}}_{\nu\nu'} (\mathfrak{R}) \right\}$ est une représentation irréductible du type F_{1g} du groupe O_h, qui peut être prise comme réelle ($\nu, \nu' = x, y, z$).

Alors, l'introduction de (19) dans (18) entraîne — compte tenu de (13) — la transformation suivante pour $\mathscr{L}_{\gamma\beta}$:

$$\mathscr{L}^{T}_{\gamma\beta} = D^{F_{1g}}_{\gamma\gamma'}(\Re)\; D^{F_{1g}}_{\beta\beta'}(\Re)\; \mathscr{L}_{\gamma'\beta'} \tag{20}$$

Et, *puisque les* $\mathscr{L}_{\gamma\beta}$ *doivent, en même temps, rester invariants* — item (ii) de notre méthode —, (20) impose:

$$\mathscr{L}_{\gamma\beta} = D^{F_{1g}}_{\gamma\gamma'}(\Re)\; D^{F_{1g}}_{\beta\beta'}(\Re)\; \mathscr{L}_{\gamma'\beta'} \tag{21}$$

Si l'on somme ici sur toutes les opérations $\Re$ du groupe O_h (d'ordre l) et si l'on utilise après le théorème d'orthogonalité des représentations irréductibles (de dimension 3)

$$\sum_{\Re} D^{F_{1g}}_{\gamma\gamma'}(\Re)\; D^{F_{1g}}_{\beta\beta'}(\Re) = \frac{l}{3}\,\delta_{\gamma\beta}\,\delta_{\gamma'\beta'} \tag{22}$$

(compte tenu du fait que les matrices D sont réelles), on obtient:

$$l\,\mathscr{L}_{\gamma\beta} = \frac{l}{3}\,\delta_{\gamma\beta}\,\delta_{\gamma'\beta'}\,\mathscr{L}_{\gamma'\beta'}\ . \tag{23}$$

C'est à dire que l'on aura:

$$\mathscr{L}_{\gamma\beta} = \left(\frac{1}{3}\sum_{\gamma'}\mathscr{L}_{\gamma'\gamma'}\right)\delta_{\gamma\beta}\ . \tag{24}$$

Ce qui montre que $\{\mathscr{L}_{\gamma\beta}\}$ est une matrice *diagonale* et *scalaire*.

Nous avons ainsi établi la relation (14) et, avec ceci, le fait que dans le cas particulier ici considéré, l'expression (5) de $\mathfrak{S}^{\alpha\beta}_{(e)}$ se réduit bien à l'expression (11), avec £ défini par (12).

B. Passons ensuite à la partie nucléaire, $\mathfrak{S}^{\alpha\beta}_{(n)}$.

Pour commencer, l'expression (4) peut s'écrire

$$\mathfrak{S}^{\alpha\beta}_{(n)} = m_p\,([I'']^{-1})_{\alpha\gamma}\sum_{N} Z_N\left[\delta^{\gamma\beta}\left(\mathbf{r}_N\cdot\mathbf{r}^{o}_N\right) - r^{\gamma}_N\, r^{o\beta}_N\right] \tag{25}$$

Ensuite, puisque, pour les molécules octaédriques AB_6, le centre de symétrie de la configuration d'équilibre est situé en A et coïncide avec l'origine des axes moléculaires (c'est à dire, $\mathbf{r}_A^o = 0$), nous pouvons mettre (25) sous la forme

$$\mathfrak{S}_{(n)}^{\alpha\beta} = m_p \frac{Z_B}{m_B} ([I'']^{-1})_{\alpha\gamma} \sum_N m_N \left[\delta^{\gamma\beta} \left(\mathbf{r}_N \cdot \mathbf{r}_N^o \right) - r_N^\gamma \, r_N^{o\beta} \right] \quad (26)$$

Alors il nous suffira de montrer que

$$\sum_N m_N \left[\delta^{\gamma\beta} \left(\mathbf{r}_N \cdot \mathbf{r}_N^o \right) - r_N^\gamma \, r_N^{o\beta} \right] = I''_{\gamma\beta} \quad (27)$$

pour obtenir le résultat (10).

Dans la démonstration de (27) nous recourons, d'une part, aux relations (6) rappelées dans le § 2 et, d'autre part, à la définition (7) combinée avec l'expression (8), rappelées toutes deux dans le § 2. En effet, si l'on introduit (6) dans le 1er membre de (27), on obtient l'expression

$$\sum_N m_N \left[\delta^{\gamma\beta} \left(\mathbf{r}_N^o \right)^2 - r_N^{o\gamma} \, r_N^{o\beta} \right] +$$

$$+ \sum_k \left\{ \sum_N m_N^{1/2} \left[\delta^{\gamma\beta} \left(\mathbf{r}_N^o \cdot \mathbf{l}_{Nk} \right) - r_N^{o\beta} \, l_{Nk}^\gamma \right] \right\} Q_k \quad (28)$$

dont le 1er terme est déjà visiblement $I_{\gamma\beta}^o$. Le 2ème terme de (28) peut subir les transformations successives suivantes:

$$\sum_k \left\{ \sum_N m_N^{1/2} \left[\delta^{\gamma\beta} \, \delta^{\rho\mu} \, r_N^{o\rho} \, l_{Nk}^\mu - \delta^{\beta\rho} \, r_N^{o\rho} \, \delta^{\gamma\mu} \, l_{Nk}^\mu \right] \right\} Q_k =$$

$$\sum_k \left[\left(\delta^{\gamma\beta} \, \delta^{\rho\mu} - \delta^{\beta\rho} \, \delta^{\gamma\mu} \right) \sum_N m_N^{1/2} \, r_N^{o\rho} \, l_{Nk}^\mu \right] Q_k =$$

$$\sum_k \left[\varepsilon_{\gamma\rho\chi} \, \varepsilon_{\gamma\rho\chi} \sum_N m_N^{1/2} \, r_N^{o\rho} \, l_{Nk}^\mu \right] Q_k , \quad (29)$$

où l'on a utilisé l'identité bien connue

$$\delta^{\gamma\beta}\ \delta^{\rho\mu} - \delta^{\beta\rho}\ \delta^{\gamma\mu} = \varepsilon_{\gamma\rho\chi}\ \varepsilon_{\beta\mu\chi} \quad . \tag{30}$$

Or, la dernière expression de (29) s'identifie avec $\frac{1}{2}\sum_k a_k^{\gamma\beta}\ Q_k$, d'après (8). Alors, le 1er membre de (27) devient

$$I^{o}_{\gamma\beta} + \frac{1}{2}\sum_k a_k^{\gamma\beta}\ Q_k \tag{31}$$

s'identifiant avec $I''_{\gamma\beta}$, d'après (7); ce qui démontre enfin (27).

Ainsi, l'expression (4) de $\mathfrak{S}^{\alpha\beta}_{(n)}$ se réduit bien à l'expression simplifiée (10).

Nous faisons remarquer que la très simple transformation de (25) en (26) sera également valable pour toute molécule du type AB_n ($n \geqslant 2$), à la seule condition que, dans la configuration d'équilibre, la position de l'atome A coïncide avec le centre de masse de l'ensemble des noyaux, qui est l'origine du trièdre mobile (c'est à dire, que $\mathbf{r}_A^o = 0$). C'est ainsi, même dans les cas où le centre de masse n'est pas centre de symétrie (comme, par exemple, pour PF_5 ou pour OsO_4). Par conséquent, le résultat (10) vaudra, sous la même forme, pour les molécules de ce type-là, toujours considérées comme des molécules vibrantes.

4 — Conclusion

La simplification que nous venons de démontrer possède certaines caractéristiques qui prennent de l'importance dans la perspective de nos recherches mentionnées dans l'Introduction.

(i) D'une part, cette simplification nous a conduit encore à une relation de proportionnalité directe entre la contribution nucléaire $\mathbf{m}_{(n)}$ et le moment angulaire total $\mathbf{J}$; d'après (10), compte tenu de (1) et (3), on a:

$$\mathbf{m}_{(n)} = \frac{\mu_n}{\hbar}\ \frac{m_p}{m_B}\ Z_B\ \mathbf{J} \tag{32}$$

Remarquons en plus que cette constante de proportionnalité ne dépend nullement des coordonnées nucléaires. Ainsi, quoique ce résultat soit valable pour la molécule vibrante, il ne s'écarte point de celui de ESHBACH et STRANBERG, valable pour l'approximation du rotateur rigide. En conclusion, aucun effet n'est à attendre de cette contribution (nucléaire) du moment magnétique rotationnel en ce qui concerne les possibilités d'existence de transitions dipolaires magnétiques purement rotationnelles.

(ii) D'autre part, la dite simplification nous amène à une relation entre la contribution électronique $\mathbf{m}_{(e)}$ et $\mathbf{J}$ *qui est essentiellement non-scalaire;* d'après (11), compte tenu de (1) et (3), on a en effet:

$$\mathbf{m}_{(e)} = -\frac{\mu_n}{\hbar}\frac{2m_p}{m_e}\,£\,[\mu]\,\mathbf{J} \tag{33}$$

où £ est la quantité scalaire définie par (12) et où $[\mu]$ est le tenseur défini par (9). L'expression (33) s'écarte donc, d'une façon très nette, de celle obtenue par ESHBACH et STRANDBERG, pour le rotateur rigide.

Sous les hypothèses qui nous ont permis d'obtenir (33), nous pouvons déceler dans le présent résultat deux propriétés remarquables:

a) c'est le mouvement des noyaux, par la présence de $[\mu]$ dans (33), qui confère au tenseur $\{\mathfrak{S}^{\alpha\beta}_{(e)}\}$ son caractère essentiellement non-scalaire, en même temps qu'il le rend essentiellement dépendant des coordonnées Q_k;

b) l'influence des mouvements électroniques dans (33) n'est finalement représentée que par un facteur scalaire, £, qui, en plus, ne dépend pas des coordonnées vibrationnelles (pouvant être regardé comme une constante moléculaire).

En conclusion, la contribution électronique $\mathbf{m}_{(e)}$ du moment magnétique rotationnel — du fait que, par (33), elle ne s'aligne pas en général avec le moment angulaire total $\mathbf{J}$ — pourra, en principe, dans son interaction avec le champ du rayonnement, être à l'origine de l'existence de transitions dipolaires magnétiques purement rotationnelles.

Notons encore que les composantes $\mu^{\alpha\beta}$ du tenseur $[\mu]$ peuvent être connues à une bonne approximation d'après l'interprétation théorique des spectres de vibration-rotation habituels (ceux

qui s'observent en provenance de transitions dipolaires électriques); cette connaissance expérimentale de $[\mu]$ est due à son intervention dans l'expression hamiltonienne de l'énergie cinétique du rotateur vibrant. Alors, il faut souligner que l'observation éventuelle de transitions dipolaires magnétiques, dont l'origine puisse être attribuée à l'interaction de $\mathbf{m}_{(e)}$ avec le rayonnement, conduirait à une connaissance expérimentale de la grandeur (constante) £. Ceci prend de l'importance quand on remarque que £, par son expression (12), pourra toujours être l'objet d'un calcul *ab initio* fondé sur la connaissance théorique des fonctions d'onde décrivant les états électroniques.

RÉFÉRENCES

[1] J. K. G. WATSON, J. Mol. Spectr., **40**, 536 (1971); I. M. MILLS, J. K. G. WATSON and W. L. SMITH, Mol. Phys., **16**, 329 (1969).

[2] C. BORDÉ, Communication privée (1980).

[3] N. MACIAS MARQUES, M. L. PALMA e J. BORDÉ, Comunicação B. 1, 3.ª Conf. Nac. de Física (Física/82), Coimbra, Portugal (1982); M. L. PALMA, N. MACIAS MARQUES and J. BORDÉ, Communication 0.1, VIII Colloquium on High Resolution Molecular Spectroscopy, Tours, France (1983).

[4] M. L. PALMA, N. MACIAS MARQUES and J. BORDÉ, «Actas da 4.ª Conferência Nacional de Física (Física/84), Évora, Portugal (1984)», Comunicação 2.13. Publication en 1985.

[5] J. R. ESHBACH and M. W. P. STRANDBERG, Phys. Rev., **85**, 24 (1952).

[6] F. MICHELOT, Mol. Phys., **45**, 949 et 971 (1982).

[7] J. K. G. WATSON, Mol. Phys., **15**, 479 (1968).

[8] W. H. FLYGARE and R. C. BENSON, Mol. Phys., **20**, 225 (1971).

[9] R. E. MOSS and J. PERRY, Mol. Phys., **25**, 1121 (1973).

MFRG STUDY OF SPIN-1 ISING MODELS: EFFECTS OF A TRANSVERSE FIELD AND RANDOMNESS IN THE CRYSTAL-FIELD COUPLING

C. A. S. SANTOS and M. C. MARQUES
Laboratório de Física, Faculdade de Ciências, Universidade do Porto
4000 Porto, Portugal

(Received 14 April 1988)

ABSTRACT — The mean-field renormalization group method is used to study the effect of the transverse field on the quantum Blume-Capel model; the critical surface in the temperature — crystal field coupling — transverse field space is obtained. The same method is applied to the Blume-Capel model with random crystal field interactions. Comparison is made with the results obtained by other methods.

1 — INTRODUCTION

Spin-1 models with crystal and biquadratic interactions were firstly introduced by Blume, Emery and Griffiths [1] to describe phase separation and superfluid ordering in He^3-He^4 mixtures, and have since been applied to order-disorder phenomena in adsorbed monolayers, multicomponent fluids and magnetic systems. Despite its simplicity the Blume-Emergy-Griffiths (BEG) model presents a complex phase diagram with first and second-order transition lines and tricritical points. Starting with the conventional mean-field aproximation used in the original paper [1], the model has since been investigated by diferent methods ranging from improved mean-field like approximations [2, 3, 4] to different RG versions [5, 6, 7]; as a result, rather accurate estimates for the location of tricritical points and tricritical exponents are now available.

Alternatively some authors have studied the (d-1)-dim model in a transverse field Γ at $T = 0$ as an equivalent system to the d-dim classical BEG model [8, 9, 10, 11, 12]. However, as far as we know, no study of the classical-to-quantum crossover which arises by switching on the transverse field at $T \neq 0$ has been presented: In this work we make use of MFRG (mean-field renormalization group), a technique which has previously been applied to the transverse spin-1/2 Ising model [13] and to the Potts model in a transverse field [14]. This same method has already been applied to the study of classical spin-1 Ising model [15, 16] and provides a reasonably accurate description of the phase diagram, namely the location of second-order phase transitions and tricritical points. The method is not entirely justified for first-order phase transitions, however its estimates of the first-order critical coupling are in some cases [17] better than those obtained by mean-field. This stands as one of the limitations of MFRG; on the other hand, the method has the advantage of enabling the calculation of the entire T-Γ phase diagram.

2.1 — *MFRG for the quantum Blume-Capel model*

We start with an hamiltonian of the form

$$H = -J \sum_{<ij>} S_i^z S_j^z + \sum_i [D(S_i^z)^2 + \Gamma S_i^x]$$

where S_i^x, S_i^z are the corresponding spin-1 matrices. When $\Gamma = 0$ this reduces to the classical Blume-Capel model. At $T = 0$, $\Gamma \neq 0$ this model is equivalent to the classical $(d + 1)$ Blume-Capel model [9].

MFRG is a model based on the comparison of two clusters of different size; the interactions within the clusters are treated exactly and the effect of the other spins is represented by a mean-field b which is assumed to scale like the order parameter itself.

We have chosen to compare one-spin and two-spin clusters, the main advantage being that calculations can then be done analytically.

The hamiltonian for the one-spin cluster is then

$$H_I = \Gamma' \, S_1^x + D' \, (S_1^z)^2 - C_I \, S_1^z$$

where $C_I = zJ'b'$ represents the surrounding mean-field, and z is the number of nearest neighbours to one spin.

If we assume b' to be small (which is true in the vicinity of a second-order transition) we can work out a perturbation expansion for $<S^z>$ in powers of b' and keep only the lienar term. This is done in the Appendix following the method of ref. [14]; one gets

$$m_I = <S^z>_I = \frac{2}{\beta \, C_I} \cdot \frac{Z_\uparrow^{(2)}}{Z_\uparrow^{(0)}} + 0\,(b'^2)$$

The hamiltonian for the two-spin cluster is

$$H_{II} = \Gamma \, (S_1^x + S_2^x) + D \, [\, (S_1^z)^2 + \, (S_2^z)^2 \,] - \\ - J \, S_1^z S_2^z - C_{II} \, (S_1^z + S_2^z)$$

Where $C_{II} = (z-1)\,Jb$; and

$$m_{II} = < \frac{S_1^z + S_2^z}{2} >_{II} = \frac{1}{\beta \, C_{II}} \cdot \frac{Z_{II}^{(2)}}{Z_{II}^{(0)}} + 0\,(b^2) \quad \text{(see Apendix)}$$

The MFRG assumption is that b' and b must scale like m_I and m_{II}; imposing this scaling relation for b' and b, we arrive at the renormalization recursive relation for $K' \, (= J' \beta')$, $\Delta' \, (= D' \beta')$, $\alpha' \, (= \Gamma' \beta')$ and K, Δ, α (defined analogously).

The fixed point equation associated with it

$$\frac{1}{z-1} \cdot \frac{Z_{II}^{(2)}}{Z_{II}^{(0)}} \Bigg|_{(K^*,\, \Delta^*,\, \alpha^*)} = \frac{2}{z} \cdot \frac{Z_I^{(0)}}{Z_I^{(2)}} \Bigg|_{(K^*,\, \Delta^*,\, \alpha^*)} \qquad (1)$$

yields the phase diagram in the transverse field-temperature space.

2.2 – *Results*

The phase diagram obtained from equation [1] for a square lattice ($z = 4$) is chown in Fig. 1. For $\Gamma = 0$ the model reduces to the situation treated by de Alcantara Bonfim [15], i. e. the classical Blume-Capel model. This author has associated the tricritical coordinate, Δ_t, to the maximum value taken by Δ in the

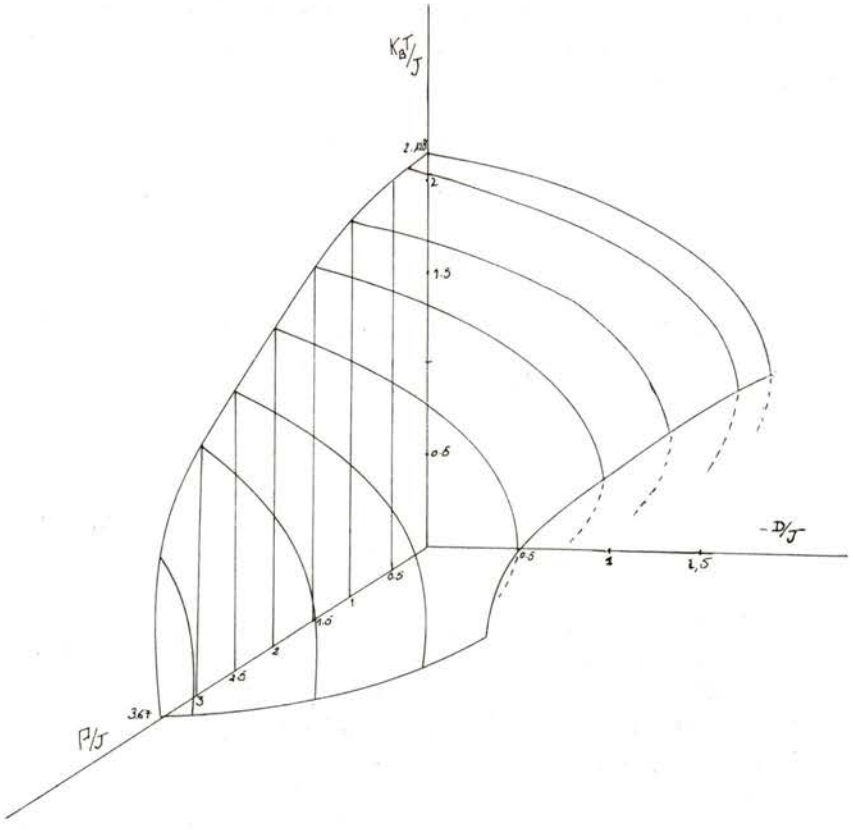

Fig. 1 — Phase diagram of the quantum Blume-Capel model in the T-D-Γ space

———— second-order transition

– – – – – – – first-order transition

curve obtained from MFRG. This method does not envolve a calculation of the free energy necessary to locate the first-order line. However a study of this model by means of the linear chain approximation [4] has shown that in the Δ region where a pair of solutions exists, the upper branch of the curve can be interpreted as giving the Curie temperature of a second-order phase transition, the tricritical point Δ_t within 0.2 % of the maximum value taken by Δ in that curve. We take this argument to support the, otherwise unjustified, assumption of de Alcantara Bonfim and associate the tricritical point with the point beyond which no solution exists to equation (1). The lower branch of the curve (shown in dash) represents an unstable solution. One knows from ground state energy considerations that the first-order line must cut the $T = 0$ axis at $2D/zJ = 1$, so at low temperatures the first-order line is certainly not well represented by the dashed line.

Fig. 2 shows the phase diagram at $T = 0$, for a unidimensional lattce ($z = 2$), together with the predictions of mean-field and other RG methods [9, 11, 12] devised for the $T = 0$ case only. We can see that the curve obtained from equation (1) compares well with the estimates of the second-order lines as given by other RG techniques. However the intersection of the line of extremal points (T_f , D_t , Γ) with the $T = 0$ plane does not coincide with the tricritical point as predicted by the other RG methods. Whether this is due to a failure of the criterium used by the Alcantara Bonfim for the location of the tricritical point within MFRG, or whether it is a limitation of the other RG methods is not clear at the moment. The techniques used by other authors are essentially real-space block spin RG schemes by which a few neighbouring spins are grouped into blocks, the intrablock Hamiltonian is diagonalized and its three lowest levels retained to define the new single-spin variables; this truncation procedure is certainly a limitation of these methods. In the MFRG method the contributions of all the energy levels of the two-spin cluster are duly accounted for in the derivation of the RG recursion relation. On the other hand the MFRG procedure leads to just one equation relating K, α, Δ and K', α', Δ', whereas a completely specified RG scheme requires more than one equation; thus, only

a few points in the critical surface obtained from equation (1) are actually fixed points of such a well specified procedure; in that respect, those other RG methods stand a better chance of

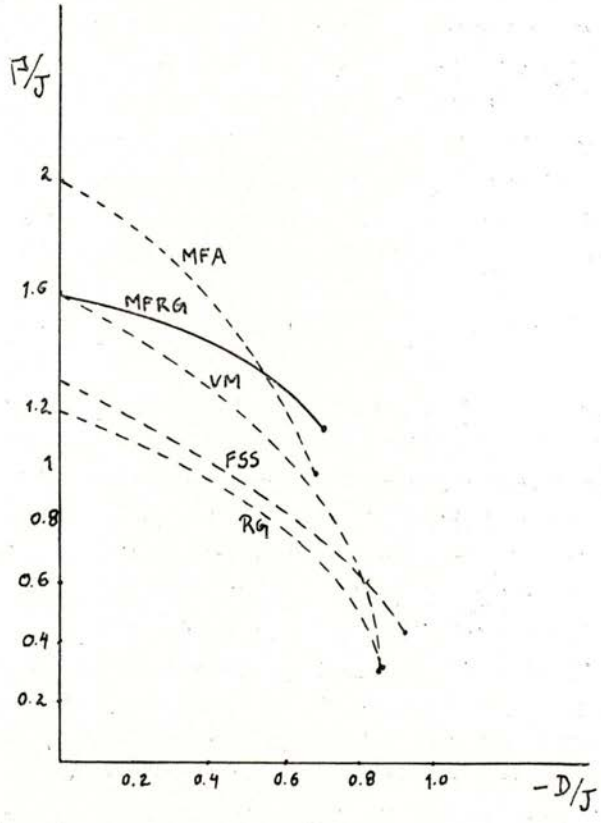

Fig. 2 — Transverse field (Γ) against crystal-field (D) for the quantum Blume-Capel model at $T = 0$; denotes the critical point (MFA — mean-field approximation; MFRG — mean-field renormalization group; VM — variational methods; FSS — finite size scaling; RG — block-spin renormalization group).

appropriately locating first-order phase transitions, since these are then associated with critical coupling lying in the domain of attraction of the so called 'discontinuity fixed points'.

3 – BLUME-CAPEL MODEL WITH RANDOM CRYSTAL-FIELD COUPLING

In this section we consider the effect of random crystal-field interactions on the phase diagram of the classical Blume-Capel system. A similar model has been studied by Kaneyoshi [18] by means of the differential operator technique.

The hamiltonian of the system is then given by

$$H = - \sum_{<ij>} J \, S_i^z S_j^z - \sum_i D_i (S_i^z)^2$$

where D_i has a probability distribution of the form

$$P(D_i) = x \, \delta(D_i - D) + (1 - x) \, \delta(D_i)$$

We get for the 1-spin and 2-spin clusters, after a configurational average has been performed:

$$m_I = \langle S^z \rangle_I = \frac{2Z \, e^{\Delta'}}{2 \, e^{\Delta'} + 1} \, . \, x' \, k' \, b' + \frac{2Z}{3} (1 - x') \, k' \, b'$$

$$m_{II} = \left\langle \frac{S_1^z + S_2^z}{2} \right\rangle_{II} = 2(z-1) \, . \, ((2 \, e^{2\Delta + k} + e^{\Delta}) \, /$$

$$(4 \, e^{2\Delta} \cosh k + 4 \, e^{\Delta} + 1)) \, . \, x^2 kb + 2(z-1) \frac{2 \, e^k + 1}{4 \cosh k + 5} \, .$$

$$(1 - x)^2 kb + 2(z-1) \, . \, ((4 \, e^{k+\Delta} + e^{\Delta} + 1) \, /$$

$$(4 \, e^{\Delta} \cosh k + 2 \, e^{\Delta} + 3)) \, . \, x(1 - x) \, kb$$

The critical lines derived from the MFRG fixed point equation are drawn in figures 3.1 and 3.2 for different values of the concentration and in the case $z = 3$ (honeycomb lattice).

The tricritical point disappears for $x = 0.745$; this differs from the value $x = 0.68$ obtained by Kaneyoshi.

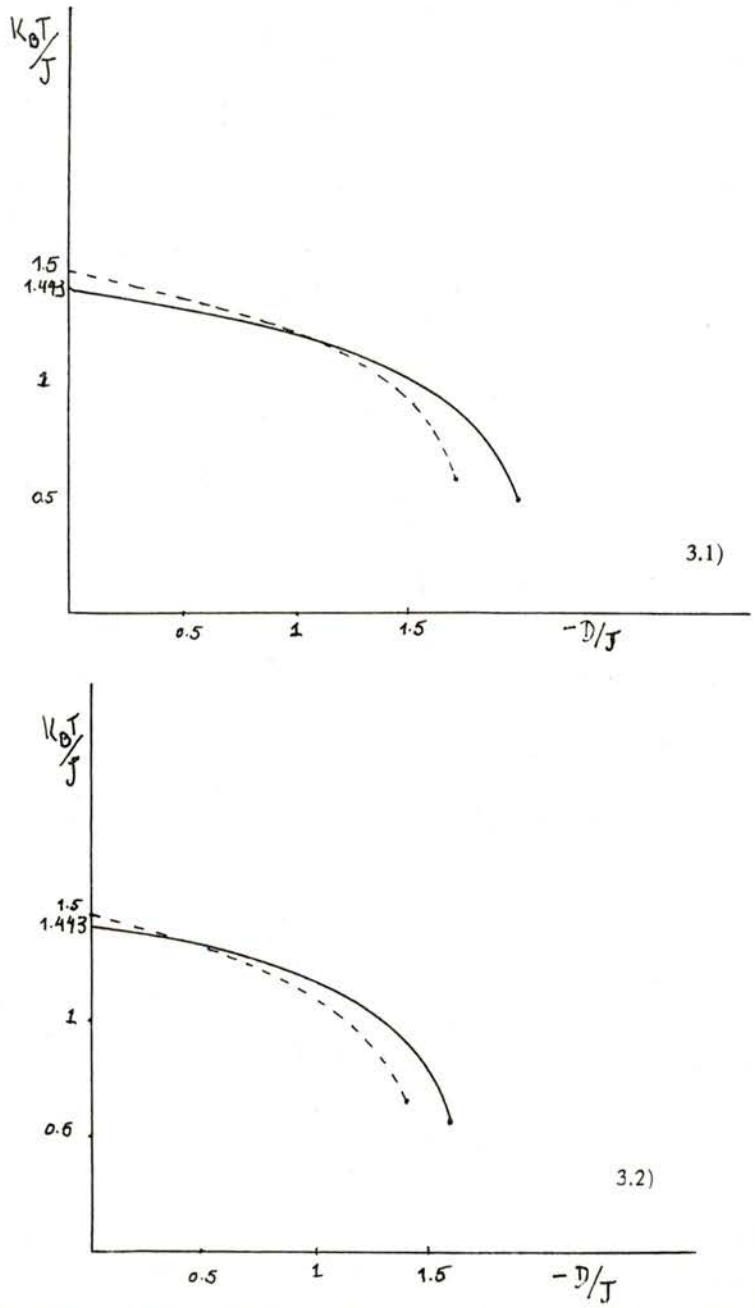

Fig. 3 — Temperature versus crystal field (D) for the classical Blume-Capel with random crystal field at two different concentrations — 3.1 — Pure case; 3.2 — x = 0.8.

4 – CONCLUSIONS

The use of MFRG has enabled us to treat the quantum Blume-Capel model at all temperatures and spatial dimensionality. In the limits $T = 0$ or $\Gamma = 0$ the results of the present work reasonably agree with those presented by other authors in what concerns the location of the line of second-order phase transitions. The tricritical point is also approximately located. The method is not appropriate to study first-order phase transitions and some of its assumptions are less justified at low temperatures when certain relevant correlations are not accounted for; these two limitations affect more critically the location of the tricritical point at low temperatures and this may be the reason for certain discrepancies with the results of other authors at $T = 0$.

We have also applied MFRG to the Blume-Capel model with random crystal-field coupling. The results compare well with those obtained by other methods; this is probably due to the fact that dilution of the crystal-field coupling does not bring the tricriticral point to a low temperature range, as in the former case.

Better accuracy can be achieved by considering bigger clusters which means however that the fixed point equation no longer can be analytically obtained.

We thank M. A. Santos for discussions and a critical reading of the manuscript. C. A. S. Santos acknowledges the financial support of Instituto Nacional de Investigação Científica under a 'Bolsa de Iniciação à Investigação'.

APPENDIX

The eigenvalues and eigenvectors of the isolated one-spin cluster

$$H_I^0 = \Gamma' \, S_1^x + D' \, (S_1^z)^2$$

are the following

$$E_1 = D' \; ; \; |U_1> = \frac{1}{\sqrt{2}} \; (|\uparrow> - |\uparrow>)$$

$$E_2 = (D' + A)/2; \; |U_2> = \frac{D' + A}{\sqrt{2(D' + A)^2 + 8\Gamma'^2}} \cdot (|\uparrow> +$$

$$+ \frac{2\sqrt{2}\,\Gamma'}{D' + A} \cdot |\rightarrow> + |\uparrow>)$$

$$E_3 = (D' - A/2; \; |U_3> = \frac{D' - A}{\sqrt{2(D' - A)^2 + 8\Gamma'^2}} \cdot (|\uparrow> +$$

$$+ \frac{2\sqrt{2}\,\Gamma'}{D' - A} \cdot |\rightarrow> + |\downarrow>)$$

where $A = \sqrt{D'^2 + 4\,\Gamma'^2}$

The partition function Z_I which corresponds to the hamiltonian H_I can then be [14]

$$Z_I = Z_I^{(0)} + Z_I^{(2)} + O(b'^3)$$

where $Z_I^{(0)} = e^{-\beta D'} + e^{-\beta/2(D'+A)} + e^{-\beta/2(D'-A)}$ is the unperturbated partition function and

$$Z_I^{(2)} = \beta C_I^2 \left[\frac{(D' + A)^2}{(D' + A)^2 + 4\Gamma'^2} \cdot \frac{2}{A - D'} \cdot \right.$$

$$(e^{-\beta D'} - e^{-\beta/2(D'+A)}) + \frac{(D' - A)^2}{(D' - A)^2 + 4\Gamma'^2}$$

$$\left. \cdot \frac{2}{D' + A} \; (e^{-\beta/2(D'-A)} - e^{-\beta D'}) \right]$$

One then gets

$$\beta < S_1^z >_I = \frac{d\ln Z_I}{dC_I} = \frac{1}{Z_I^{(0)}} \cdot \frac{dZ_I^{(2)}}{dC_I} + O(b'^2) =$$

$$= \frac{2}{C_I} \cdot \frac{Z_I^{(2)}}{Z_I^{(0)}} + O(b'^2)$$

The hamiltonian for the isolated two-spin clusters is

$$H_{II}^{0} = \Gamma (S_1^x + S_2^x) + D [(S_1^z)^2 + (S_2^z)^2] - J \, S_1^z S_2^z$$

This hamiltonian comutes with the site interchange operator and the «reflexion» operator $\hat{P} \mid m_1 m_2 > = \mid - m_1 - m_2 >$; we can therefore search for the eigenvectors of H_{II}^{0} among the eigenvectors of these operators. One obtains

$$\mid V_1 > = \frac{J + D + B}{\sqrt{(J + D + B)^2 + 4\Gamma^2}} \cdot \left[\frac{2\Gamma}{J + D + B} \cdot \mid U_1 > + \mid U_2 > \right] \qquad E_1 = \frac{J + 3D - B}{2}$$

$$\mid V_2 > = \frac{J + D - B}{\sqrt{(J + D + B)^2 + 4\Gamma^2}} \cdot \left[\frac{2\Gamma}{J + D - B} \cdot \mid U_1 > + \mid U_2 > \right] \qquad E_2 = \frac{J + 3D + B}{2}$$

$$\mid V_3 > = \mid U_3 > \qquad E_3 = D$$

$$\mid V_8 > = \frac{D - J - C}{\sqrt{(D - J - C)^2 + 4\Gamma^2}} \cdot \left[\frac{2\Gamma}{D - J - C} \mid U_8 > - U_9 > \right] \qquad E_8 = \frac{3D - J + C}{2}$$

$$\mid V_9 > = \frac{D - J + C}{\sqrt{(D - J + C)^2 + 4\Gamma^2}} \cdot \left[\frac{2\Gamma}{D - J + C} \mid U_8 > - U_9 > \right] \qquad E_9 = \frac{3D - J - C}{2}$$

where $B = \sqrt{4\Gamma^2 + (J + D)^2}$, $\quad C = \sqrt{4\Gamma^2 + (J - D)^2}$ and

$$f(J, D, \Gamma, E_k) = (E_k (-J + 2D - E_k)(J + 2D - E_k)) / \sqrt[\Gamma]{F}$$

$$F = E_k^2 (J + 2D - E_k)^2 + 2(-J + 2D - E_k)^2 (J + 2D - E_k^2) + \\ + E_k^2 (-J + 2D - E_k)^2 + E_k^2 (-J + 2D - E_k)^2 (J + 2D - E_k^2)/\Gamma^2$$

$$|V_k> = \frac{\Gamma}{J-2D+E_k} \cdot f(J,D,\Gamma,E_k) \cdot |U_4> + \frac{\sqrt{2}\,\Gamma}{E_k} \cdot$$

$$f(J,D,\Gamma,E_k)\,|U_6> - \frac{\Gamma}{J+2D-E_k}\, f(J,D,\Gamma,E_k) \cdot$$

$$\cdot\, |U_7> + f(J,D,\Gamma,E_k)\,|U_5> \qquad E_k\,,\ k = 4,5,6,7$$

The E_k's are the solutions of equation

$$[(2D-E_k)^2 - J^2]\ [E_k(E_k-D) - 2\Gamma^2] + 2\Gamma^2 E_k(2D-E_k) = 0$$

A perturbation expansion of $<S_1^z + S_2^z>$ requires the calculation of matrix elements $<V_j|\, S_1^z + S_2^z\,|V_j>$, of which only a few are nonzero.

Following the same procedure as above we get

$$1/2\,<S_1^z + S_2^z>_{II} = \frac{C_{II}}{Z_{II}^{(0)}} \sum_{i=1}^{7} e^{-\beta E_i} \sum_j \frac{A_{ji}}{E_j - E_i}$$

where the coefficients A_{ij} are defined as $|\,<V_j|\, S_1^z + S_2^z\,|\,V_i>\,|^2$. The expressions for the nonvanishing elements are

$$A_{31} = A_{13} = \frac{4\Gamma^2}{4\Gamma^2 + (J+D+B)^2}$$

$$A_{32} = A_{23} = \frac{4\Gamma^2}{4\Gamma^2 + (J+D-B)^2}$$

$$A_{8k} = A_{k8} = \frac{(D-J-C)^2}{4\Gamma^2 + (D-J-C)^2} \cdot f^2(J,D,\Gamma,E_k) \cdot$$

$$\left[\frac{4\Gamma^2}{(D-J-C)\,(J-2D+E_k)} - 1\right]^2;\ k = 4,5,6,7$$

$$A_{9k} = A_{k9} = \frac{(D-J+C)^2}{4\Gamma^2 + (D-J+C)^2} \cdot f^2(J,D,\Gamma,E_k)$$

$$\left[\frac{4\Gamma^2}{(D-J+C)\,(J-2D+E_k)} - 1\right]^2;\ k = 4,5,6,7$$

REFERENCES

[1] BLUME M., EMERGY V. J., GRIFFITHS R. B., Phys. Rev. **A4** (1971), 1071.
[2] IWASHITA T., URYÛ N., Phys. Lett. **73A** (1979), 333.
[3] CHAKRABORTY K. G., Phys. Rev. **B29** (1984), 1454.
[4] CHAKRABORTY K. G., TUCKER J. W., Physica **137A** (1986), 111.
[5] ADLER J., AHARONY A., OITMAA J., *JJ.* Phys. **A11** (1978), 963.
[6] KAUFMAN M., GRIFFITHS R. B., YEOMANS J. M. F., Phys. Rev. **B23** (1981), 3448.
[7] LANDAU D. P., SWENDEN, Phys. Rev. **B33** (1986), 7700.
[8] BOYANOVSKY D., MASPERI L., Phys. Rev. **D21** (1980), 1550.
[9] HAMBER H., Phys. Rev. **B21** (1980), 3999.
[10] GEFEN Y., IMRY Y., MUKAMEL D., Phys. Rev. **B23** (1981), 6099.
[11] ALCARAZ F. C., DRUGOWICH DE FELÍCIO J. R., KÖBERLE R., STILCK J. F., Phys. Rev. **B32** (1985), 7469.
[12] ARIZMENDI C. M., EPELE L. N., FANCHIOTTI H., GARCIA CANEL C. A., Z. Phys. **B64** (1986), 231.
[13] PLASCAK J. A., J. Phys. **A17** (1984), L279.
[14] MARQUES M. C., SANTOS M. A., J. Phys. **C19** (1986), 4213.
[15] DE ALCÂNTARA BONFIM O. F., Physica **130A** (1985), 367.
[16] DE ALCÂNTARA BONFIM O. F., SÁ BARRETO F. C., Phys. Lett. **109A** (1985), 341.
[17] INDEKEU J. O., MARITAN A., STELLA A. L., J. Phys. **A15** (1982), 291.
[18] KANEYOSHI T., J. Phys. **C19** (1986), L557.

PRECIPITATION OF THE PHASE α - Fe_2O_3 IN GLASSES OF THE SYSTEM $\times$ Fe_2O_3 $PbO.2B_2O_3$ (*) ($0.1 \leqslant \times \leqslant 0.6$)

D. M. C. GUIMARÃES

Centre of Physics of Aveiro University (INIC)
3800 Aveiro — Portugal

(Received 13 February 1988, revised 6 October 1988)

ABSTRACT — The precipitation of the phase α - Fe_2O_3 in glasses of the system x Fe_2O_3 $PbO.2B_2O_3$ depends both on concentration and cooling rate. It is shown that the effect of the cooling rate is strikingly important.

1 — INTRODUCTION

With glasses x Fe_2O_3 $PbO.2B_2O_3$, the phase α - Fe_2O_3 does not precipitation for $x < 0.3$. From $x \geqslant 0.3$ the phase α - Fe_2O_3 begins to precipitatate and this effect becomes more and more intense with the increase in x. The effect of the cooling rate is preponderant. Experiments were devised in order to get experimental evidence of the influence of the factors that determine the precipitation of α - Fe_2O_3.

2 — THE ROLE OF THE COOLING RATE

The cooling rate depends on a number of factors such as thermal diffusivity, radiation transfer, geometric shape, surface conditions and first of all on the sample volume. In the next paragraph is described that blocks of glass with considerable

(*) Presented at the VI Nacional Conference of Physics (26-29 September, Aveiro, Portugal).

dimensions were prepared so that a rather smooth variation of cooling rate was obtained between the central zone and the walls. So, it was possible to observe the influence of the cooling rate on the precipitation of α - Fe_2O_3.

3 — OBSERVATIONS WITH GLASSES xFe_2O_3 $PbO.2B_2O_3$

3.1 — *Glass preparation*

The constituents of the glass (Fe_2O_3, PbO, BO_3H_3) were mixed in stoichiometric proportions during several hours in a «rotary ball mill». The mixture was put inside a platinum crucible that was introduced in a furnace at 1100°C during 2 hours. The liquid was afterwards mouled. The mould was pre-heated and was formed by metallic blocks that were adequately disposed. The blocks were recovered by colloidal graphite. The so prepared glass clocks had approximately 6 cm $\times$ 4 cm $\times$ 2 cm. They were introduced in a furnace at 450°C for annealing (2 hours). Glasses were prepared corresponding to the following compositons: $x = 0.1, 0.2, 0.25, 0.3, 0.35, 0.4, 0.45, 0.48, 0.5, 0.52, 0.55, 0.57, 0.6$.

3.2 — *Observation of the glass structure*

The blocks of glass were sliced and several sections were chosen for mounting and polish.

For $x = 0.1$ and 0.2, the optical microscope, the scanning electron microscope and the X-rays did not reveal the presence of the phase α - Fe_2O_3.

The first observed crystals began to appear for $x = 0.3$, close to the surface of the sample. Fig. 1 and Fig. 2 show photographs corresponding to compositions $x = 0.3$ and $x = 0.35$ obtained with the scanning electron microscope. All the other photographs were obtained with the same apparatus.

For $x = 0.4$, zones with crystals were observed in the bulk of the material (Fig. 3), but X-rays did not reveal yet the presence of the phase α - Fe_2O_3.

The peaks corresponding to α - Fe_2O_3 by X-rays diffraction only appear for $x \geqslant 0.45$, because in these conditions the con-

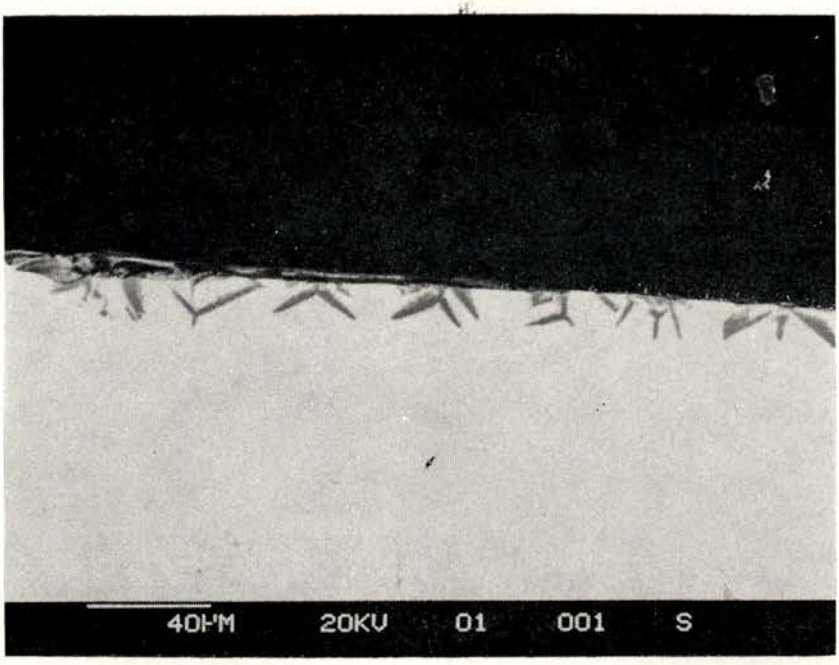

Fig. 1 — Small crystals are formed at the surface of the sample ($x = 0.3$) ($\times$ 400)

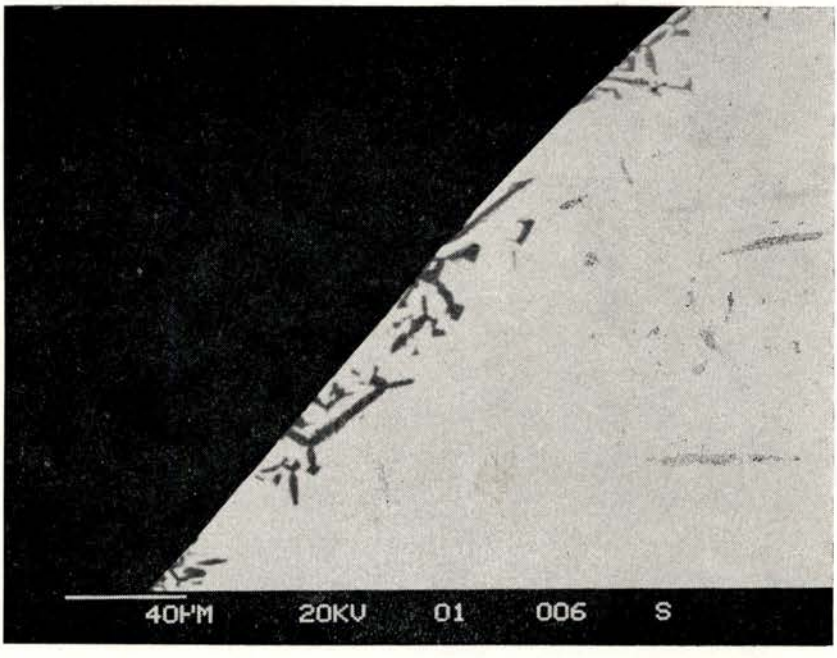

Fig. 2 — Crystal and aggregates close to the surface are bigger than in Fig. 3 ($x = 0.35$) ($\times$ 400)

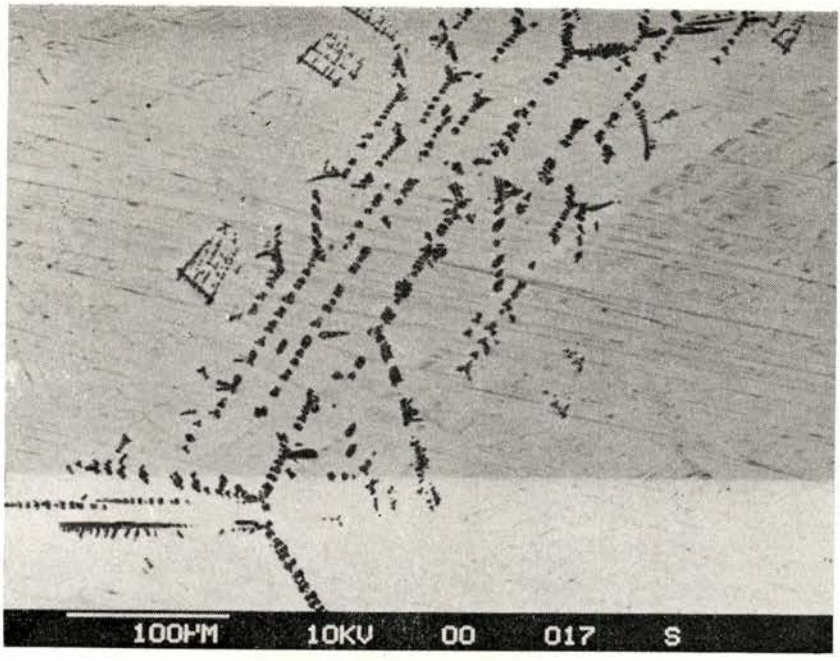

Fig. 3 — An «island» formed by crystals is seen, but the overall concentration is very small and X-rays do not «see» the crystals
($x = 0.4$ ($\times$ 200)

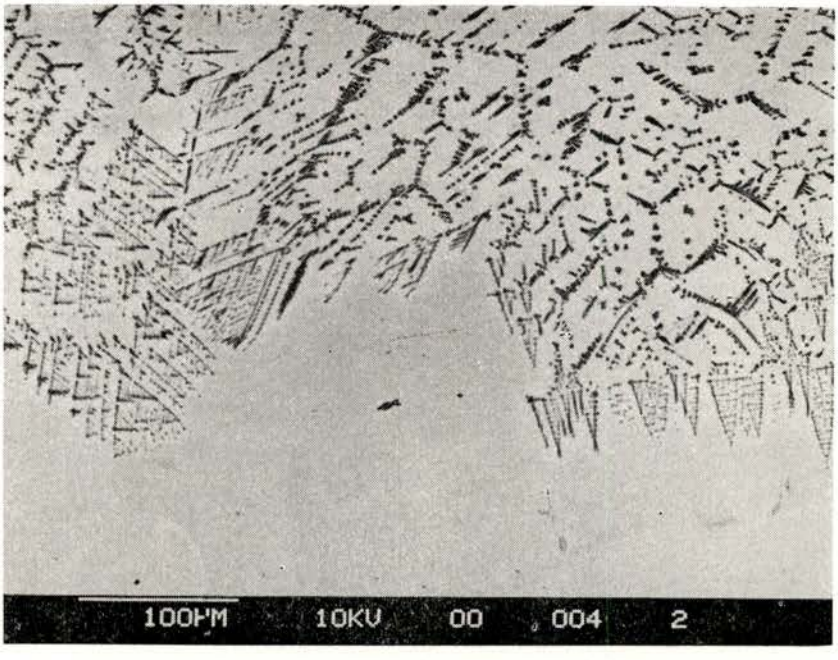

Fig. 4 — Here is shown the disappearance of crystals near the wall
($x = 0.5$) ($\times$ 200)

centration of the phase becomes high enough. Neverthelless, no volume fraction determinations were possible for $x < 0.48$, due to the existence in the sample of regions with no crystals whose dimensions were very difficult to estimate.

For $0.48 < \times < 0.6$ it was observed that the volume fraction of the phase α - Fe_2O_3 increases rather regularly with x; for a given x, the sizes of the crystals and crystal aggregates and the volume fraction increase from the boundary to the central zone of the sample.

Near the walls one observes no precipitation of crystals at all. The high cooling rate in these zones prevents entirely the crystallization (Fig. 4).

For $x = 0.5$ and $x = 0.6$ photographs of corresponding zones in the samples do not reveal an evident difference (Fig. 5, Fig. 6). Nevertheless repeated measurements have led to the result that the volume fraction is bigger for $x = 0.6$:

Composition x	Volume fraction	
	Central zone	zone far from centre (~ 1.5 cm from wall)
0.5	28 %	13 %
0.6	28 %	18 %

Intermediate values were found $0.5 < \times < 0.6$. An absolute indetermination of 2 % is admited in all results, due to the poor reproducibility of the conditions of sample preparation, difference in the mass of the sample from case to case and the errors inherent to the process of measurement.

It is well known that the morfology of the phases resulting from a demixetion process vary according the mechanism of the decomposition. In the case of the nucleation and growing mechanism the separated particles have a spherical appearance and show a poor connectivity. This is not evidently the case under study. The features of the precipitated phase that shows an irregular configuration and strong aggregation of the crystallites suggest the occurrence of a spinodal decomposition [1].

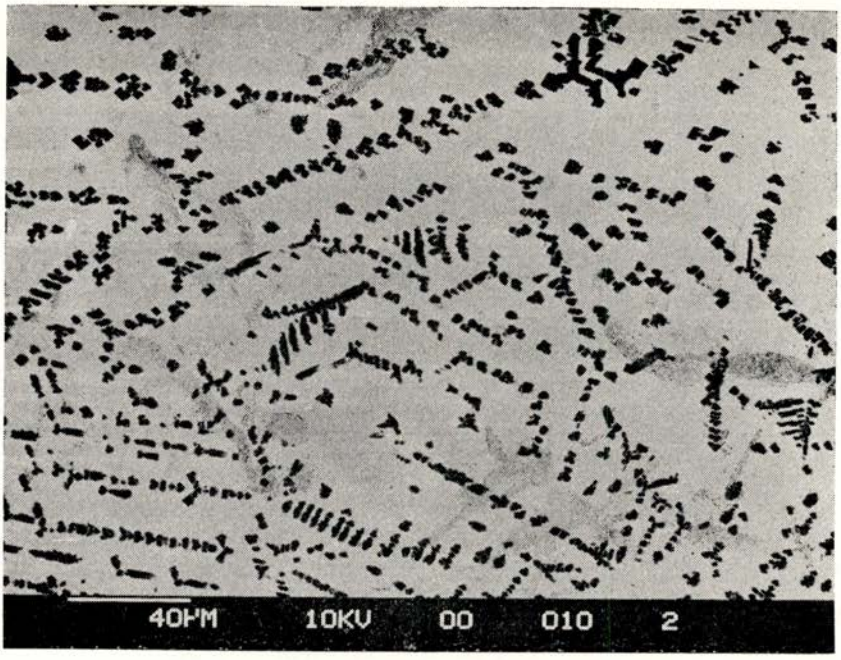

Fig. 5 — This is a region of small crystals, not too far from the wall. Crystals are spread all over the sample (x = 0.5) (× 400)

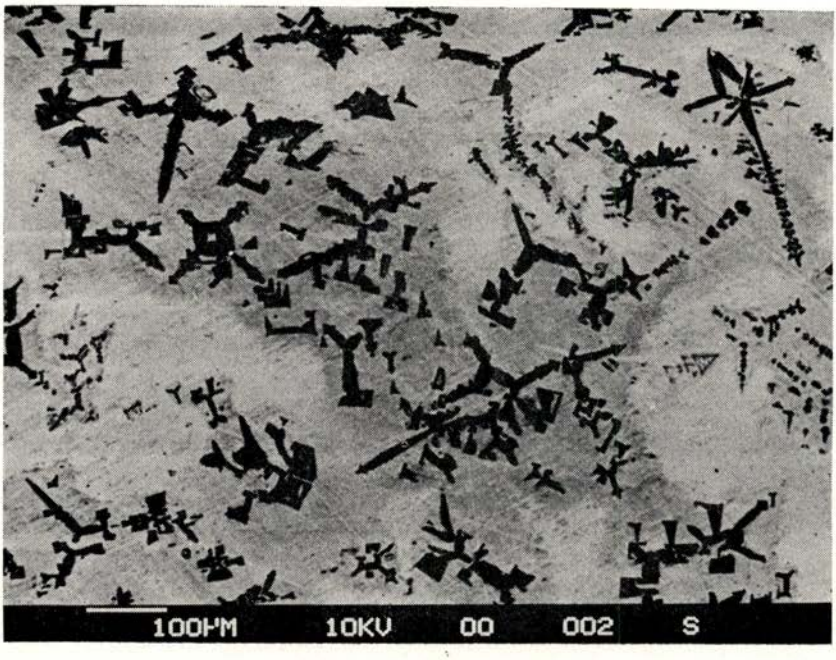

Fig. 6 — This is a central zone. In general the crystals constitute big and irregular aggregates (x = 0.6) (× 100)

The technique used for volume fraction determination [2, 3] was point counting. Measurements were carried on with a transparent millimetric sheet, where a mesh of adequate size (of the same order of that of the crystallites) was chosen.

4 — CONCLUSION

The precipitation of the phase α - Fe_2O_3 in glasses of the system xFe_2O_3 $PbO.2B_2O_3$ is strongly dependent on the cooling rate. Regions where the cooling rate is high enough (vicinity of walls) are completely devoid of crystals. On the other hand, big aggregates of crystals appear in central zones where the cooling rate is minimum. The volume fraction of the phase α - Fe_2O_3 increases with x ($x \geqslant 0.3$).

This work was carried on in the Physics Department of Warwick University.

We acknowledge Dr. S. K. Mendiratta of Aveiro University who introduced us in the study of glasses xFe_2O_3 $PbO.2B_2O_3$, read the manuscript and made useful suggestions. We are grateful to Dr. D. Holland of Warwick University for assistance and to the technical staff for help.

Financial support from INIC (Portugal) is acknowledged.

REFERENCES

[1] ZARZYCKI, J., *Les Verres et l'État Vitreux*, Masson (1982).

[2] DEHOFF, Robert T. & RHINES, Frederick N., Ed., *Microscopie Quantitative*, Masson (1972).

[3] UNDERWOOD, Ervin E., *Quantitative Stereology*, Addison-Wesley Publishing Company (1969).

AEROMAGNETIC SURVEY OF PORTUGAL
Northern Panel

MIRANDA, J. M.
GALDEANO, A.
MENDES VICTOR, L. A.
Centro de Geofísica da Universidade de Lisboa
Institut de Physique du Globe de Paris

(Received April 1988)

ABSTRACT — In an earlier paper (Miranda et al., 1987) we presented the southern panel of the Aeromagnetic Survey of Portugal. With the conclusion of the northern one, here discussed, the survey is accomplished and an accurate mapping of the total magnetic field, for the 1980.0 epoch, is achieved.

The fitting of the two panels of the survey, for the chosen reference epoch, is made using the IGRF80 model, whose quality is judged from the array of magnetic repeat stations established by the Instituto Nacional de Meteorologia e Geofísica.

The analytical representation of the normal field is poorly constrained by the survey data suggesting the use of the IGRF80 model.

Finally, we present the total field anomaly map for the Portuguese mainland territory.

1 — GENERAL PROCESSING SCHEME FOR THE NORTHERN PANEL

1.1 — *Flight operations*

The flight operations of the northern panel were conducted by the geophysical team of the Portuguese Air Force and took place between the 11 June and the 30 July 1981. The total flight

time for this panel was 26 hours, corresponding to approximately 6900 km of geomagnetic profiles.

The methodology followed was similar to that described for the southern panel (op. cit.). *Synthetically,* the magnetic field was measured every second with a Geometrics G803 magnetometer. The mean flight height of 10000 feet was barometrically controlled and the horizontal position was monitored by 10 sec interval photographs taken by a synchonized camera.

The Hayford-Gauss coordinates of each photo center were geometrically identified on 1:25000 topographic maps. The true flight lines are displayed in Fig. 1 for all the survey (northern and southern panels).

1.2 – *Daily variation of the field*

Magnetic reference stations were installed in Vila Real and Tomar (see Fig. 1). The Vila Real station provided the primary reference for the entire survey area, the Tomar station being kept only as a safeguard.

The Vila Real reference station operated successfully 24 hours a day during all survey operations, assuring a «continuous» monitoring of the magnetic field's daily variation, with a repetition rate of 10 sec.

The annual mean value for the reference station at the 1981.5 epoch was deduced by comparison between its mean hourly value and the corresponding ones at Coimbra Observatory, for the interval 00.00 a.m. to 01.00 a.m. and for all the period covered by the survey operations.

The mean difference between the two stations is:

$$\overline{T}_{C,\,s} - \overline{T}_{VR,\,s} = 412 \pm 11 \text{ nT}$$

where $\overline{T}_{C,\,s}$ is the mean value for the Coimbra Observatory and $\overline{T}_{VR,\,s}$ that for the Vila Real reference station.

The value of the standard deviation is mainly due to the variability in Coimbra total field values, calculated from H and Z measurements.

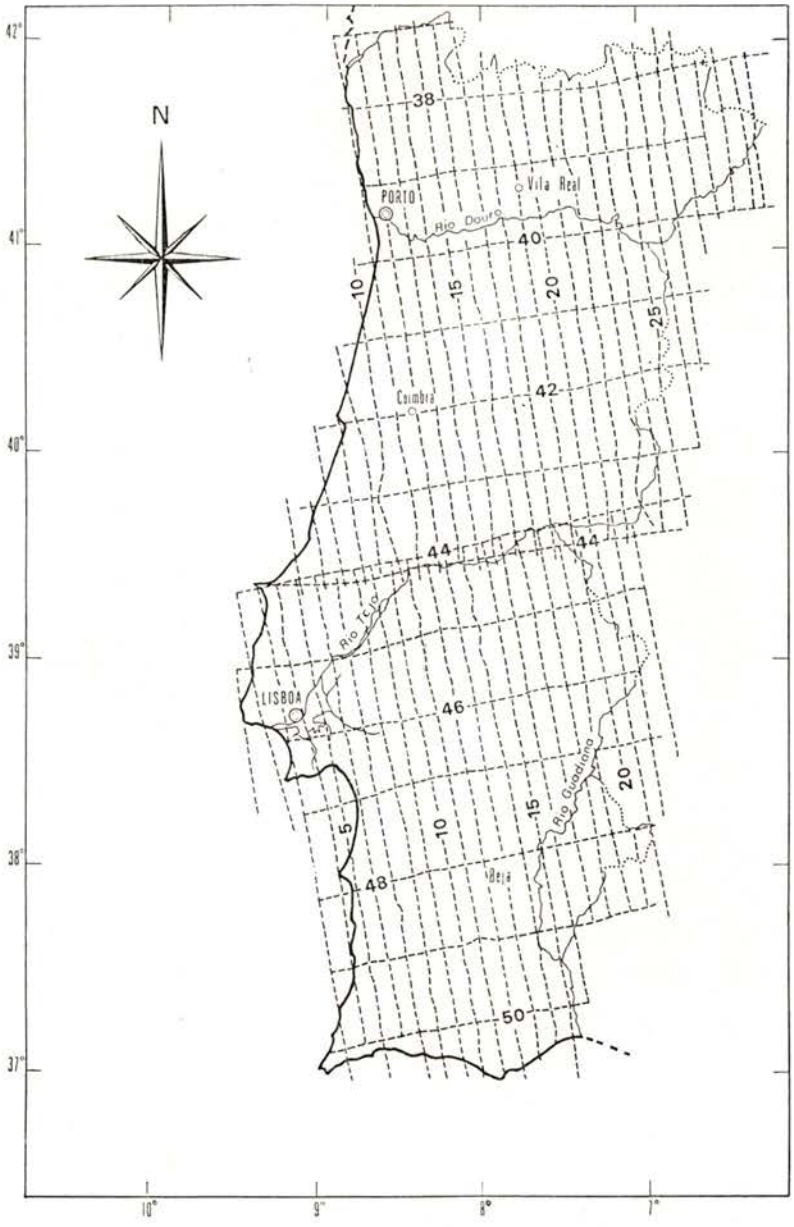

Fig. 1 — Actual flight lines of the Aeromagnetic Survey of Portugal as deduced from photo identifications.

The annual mean value for Vila Real reference station is then:

$$\overline{T}_{VR,\ 1981.5} = 44499\ nT \pm 11\ nT$$

A comparison between the Vila Real and Chambon-la-Forêt Magnetic Observatory daily values for the same period, carried out as a subsidiary check, lead to a similar value (44500 ± 12 nT). The similarity of both central values seems to indicate that the mean difference Coimbra-Vila Real is well established.

Daily variation was then determined from the differences (T_{VR} (t) $-$ 44499 nT) and applied to all field records.

1.3 — *Flight lines levelling*

The cross errors between flight and tie-lines were calculated and corrected as discussed for the southern panel. We must emphasize that flight lines 5 and 31, as they were only crossed by one tie-line, are poorly constrained, increasing the uncertainly in the corresponding field values.

The flight lines 25 and 27 and some of the tie-lines were disturbed and their mean values were significantly changed during the levelling processes as we imposed the condition that the mean cross over error for each flight line should be zero.

The residual cross errors are shown in Fig. 2. Their values are of the same order of magnitude as those presented for the southern panel, with a standard deviation of near 4.6 nT.

All the flight lines were then corrected with spline interpolation of the cross differences.

1.4 — *Data gridding*

The corrected values of the field records were filtered by «smoothing splines» (Reinsch, 1967) as described for the southern panel. The smoothing effect is, as before, very small, and mainly

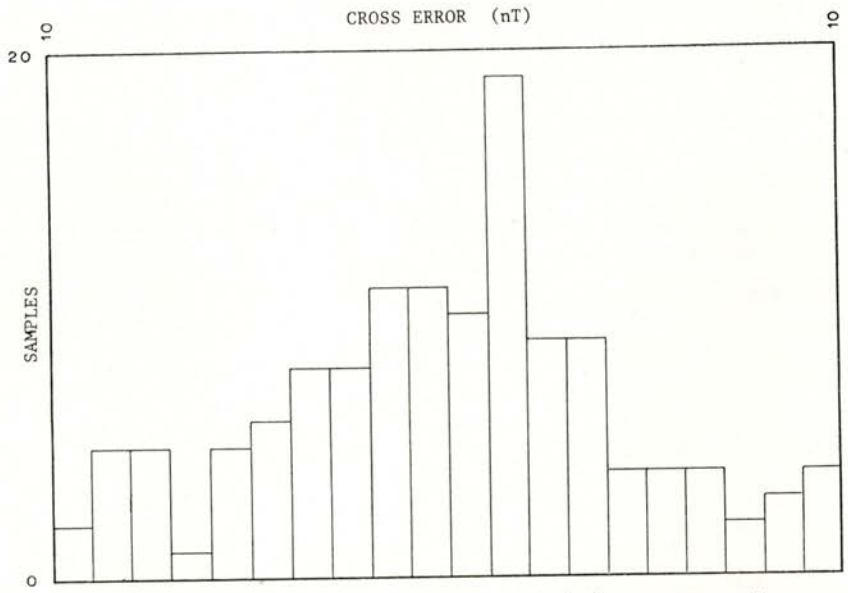

Fig. 2 — Residual errors for the northern panel of the aeromagnetic survey of Portugal.

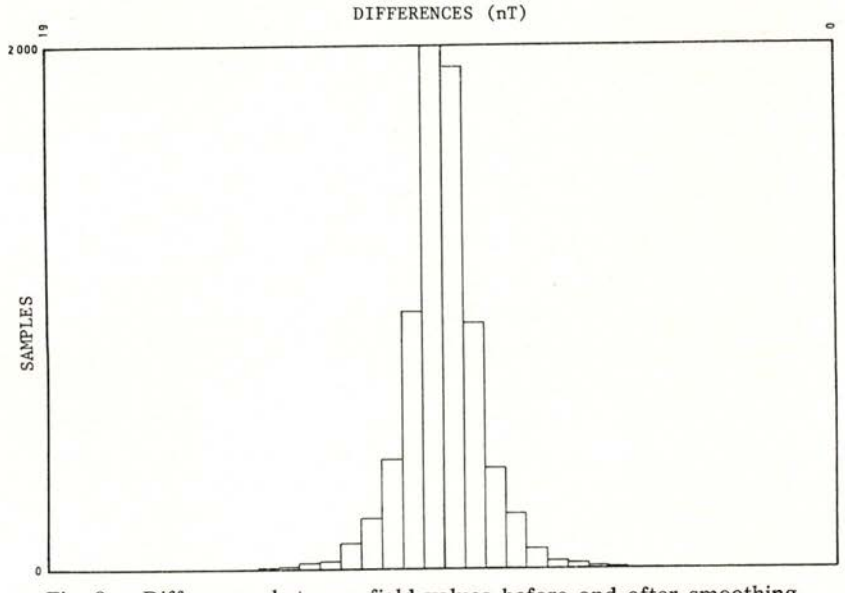

Fig. 3 — Differences between field values before and after smoothing.
(a) Coimbra Magnetic Observatory.
(b) SMN (Simona — Miranda do Douro) station.

contributes to spike elimination. In Fig. 3 we present the histogram of the differences before and after smoothing.

The projection of the flight lines over the regular grid produced a matrix with dimension (316,28) corresponding to a 10.230 km spacing between profiles (with east azimuth −7,5 degrees) and a 1 km spacing along each one.

These least squares values are significantly different from those that were found for the southern panel (10.014 km and −9.8 degrees) and, also, from the chosen value of equispacement for the representation of data.

2 – FITTING OF THE NORTHERN AND SOUTHERN PANELS

2.1 – *Secular variation model*

The southern panel was reduced to the 1979.0 epoch and the northern one to 1981.5. It was natural to choose the almost central 1980.0 epoch as the final reference of the survey.

The secular variation of the main field between 1980.0 and both individual reference epochs can be estimated from the repeat magnetic network established by the I. N. M. G. since 1952 in the portuguese territory.

From 1952 to 1962 and after 1973 the repeat stations were regularly occupied and it is possible to calculate the secular variation of the different elements (H, Z, D) in the array. Since 1978 the total field has been independently measured with a proton precession magnetometer and its secular variation can be better estimated.

As there is a relatively large number of observations (in the two periods mentioned above we almost have measurements every year) it is better to integrate all the known data in a single mathematical model for each station and then to use the explicit mathematical expression to directly compute the corresponding differences for the intervals 1979.0-1980.0 and 1980.0-1981.5.

The known existence of two «jerks» of the main field near the 1969.0 and the 1979.0 epochs imposes a necessary discontinuity

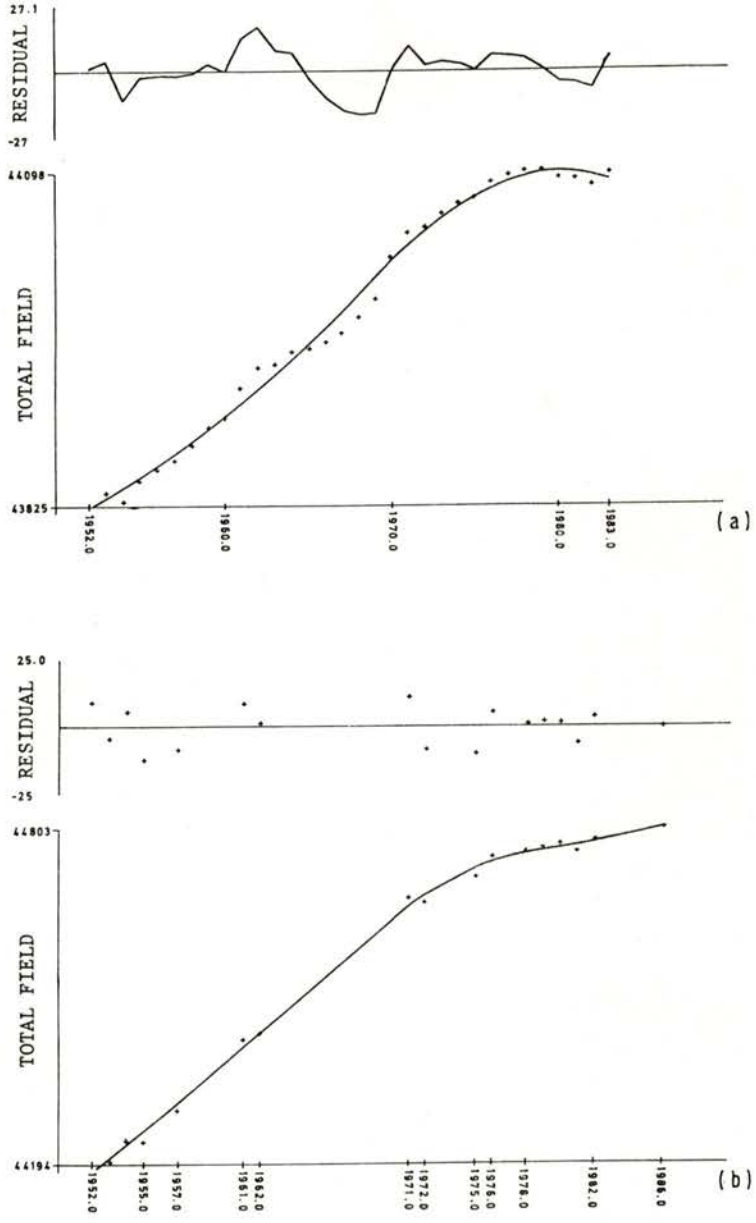

Fig. 4 — Comparison between the measured values of the total magnetic field and the interpolation by the use of a second degree polynomial for each of the intervals 1952-69; 1969-79 and 1979-86. The polynomials and their first time derivative are continuous in all the domains.

in the second time derivative of the secular variation. Consequently it was assumed that the total field could be expressed as a piecewise continuous second degree time polynominal whose coefficients differ for the three intervals (1952.0-1969.0; 1969.0--1979.0; 1979.0-1986.0) but in such a way that both the polynomials and their first time derivative are continuous throughout.

This assessment is in good agreement with the secular variation of the total field measured in Coimbra Observatory (see Fig. 4a).

The coefficients for all the repeat stations according to their effective period of occupation are presented in the table of Fig. 5. The results seem reasonable for the array, with the exception of the Algarve stations where large discrepancies are observed or the time series is very short (e. g. ARP).

STATION	A_1	B_1	A_2	B_2	A_3	B_3
COI	0.1903	7.65	−0.5902	14.29	−0.9931	2.48
CUM	0.1083	8.27	−0.7521	12.31	0.1568	−2.73
BCF	0.2216	9.94	−0.8103	17.43	−0.2347	1.27
SMN	0.0235	16.73	−0.7524	17.53	0.2069	2.48
ARP	—	—	−0.8715	13.70	−0.5956	1.50
CLV	0.0476	13.13	−0.5886	14.75	−0.9162	2.97
OLH	—	—	−1.0870	16.82	−0.0850	1.61
MRC	0.2520	7.01	−0.9502	15.57	0.3284	−3.43
BSB	—	—	−0.6569	7.97	−1.4815	2.72

Fig. 5 — Table of the coefficients; for the i-th interval the secular variation can be determined by $df = (A_i (t-t_0) + B_i (t-t_0))$ where t_0 is, respectively, 1950, 1969, 1979, t is expressed in years and df in nT.

2.2 — *The IGRF80 secular variation model*

The secular variation terms included in the IGRF80 model are not usually suitable for secular variation synthesis over long

periods of time. However, as the time interval involved in the survey is very small, both reference epochs being located in a period of known «normal» behavior of the field, it is to be expected that they would give a reasonable estimation of the secular variation of the total field.

The values obtained from the IGRF80 are compared in Fig. 6 to those that correspond to the differences previously calculated from the magnetic repeat array. It is clear that for most of the stations both values are small and there is a good agreement between them, usually within the error limits of this kind of measurements.

In the south, however, the results from the repeat magnetic array seem not reliable, as there is a difference of about 4 nT between the variation estimates of two stations (BSB and MRC) located very close to each other.

The analytic expression of the secular variation from the repeat network stations is less consistent in the south.

2.3 – *Misfit estimation*

From Fig. 1 it is clear that a small area of overlap exists around tie-line 44 allowing a check of the misfit between the two panels of the survey

Unfortunately, the azimuth of the flight lines is different for the two panels and so there are no points belonging to both panels. Consequently it is necessary to perform an adequate interpolation of the measurements points to get an estimator of the differences, free from regional variations.

In Fig. 7 we present a typical result of the observed misfit along the flight line 9.

The analysis of all lines shows the existence of a systematic north-south positive difference with an average value of 6.0 nT. This difference is probably connected to the reduction methods employed and is within the error limits of the method.

The final survey accuracy did not change significantly from one part of the survey area to the other. The cross errors and the

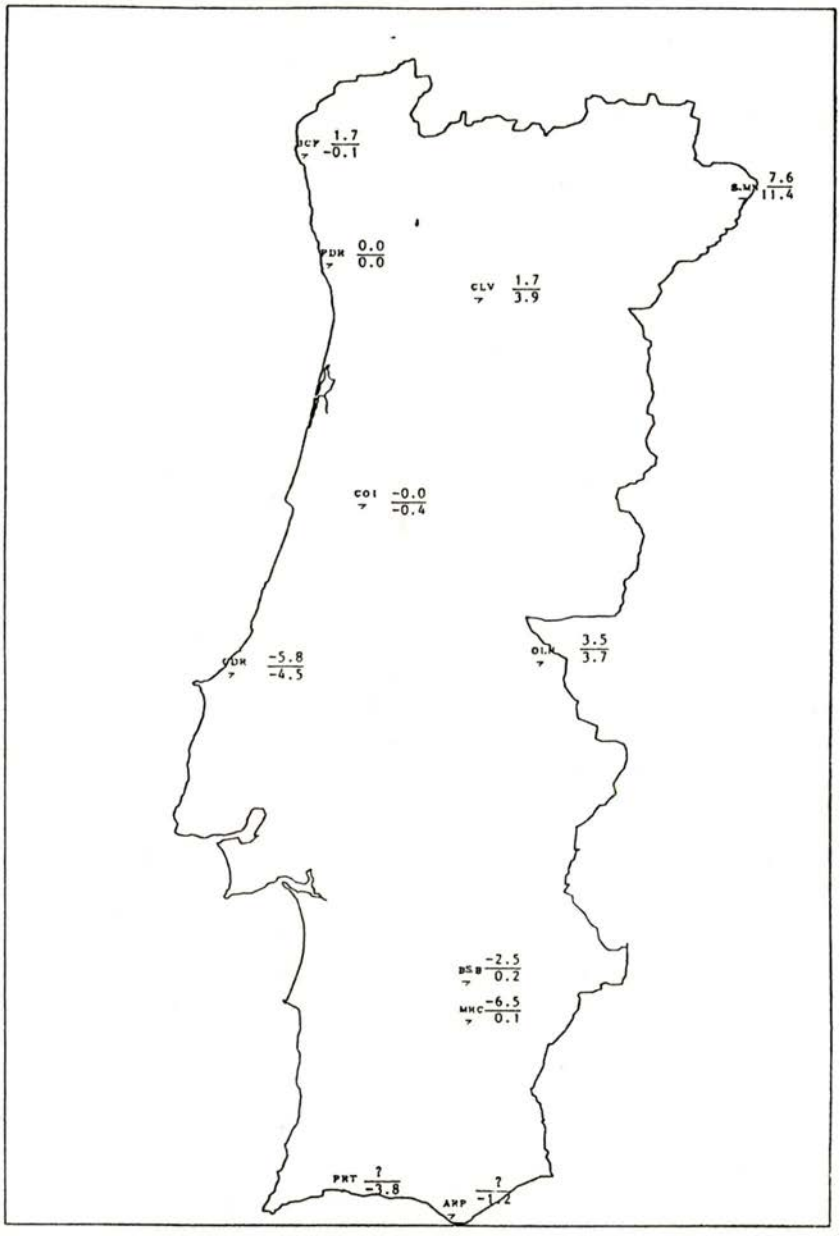

Fig. 6 — Differences between IGRF80 secular variation model (numerator) and the calculated values from INMG array of magnetic repeat stations (denominator) (nT).

uncertainty of the mean annual values for the Beja and Vila Real reference stations are quite similar. It is then justifiable to equally divide the average misfit between the two panels. This corresponds to a change of ± 3.0 nT in all field values.

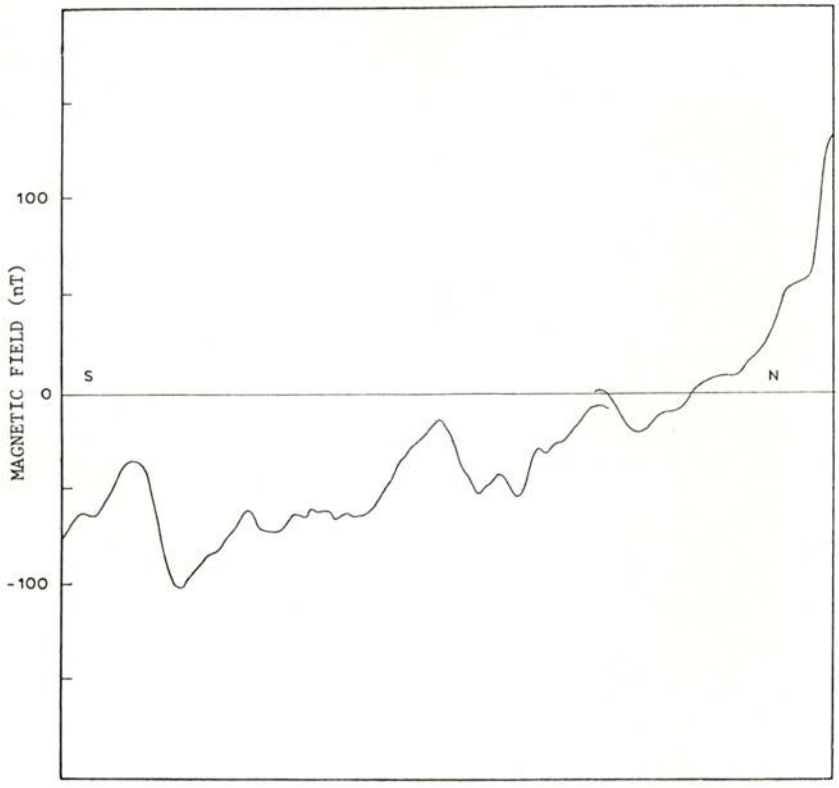

Fig. 7 — Fit of the northern and southern flight lines n.° 9.

After this translation all pairs of flight lines were slightly adjusted to assure a smooth transition along the overlapping area.

The final map is presented in Fig. 8.

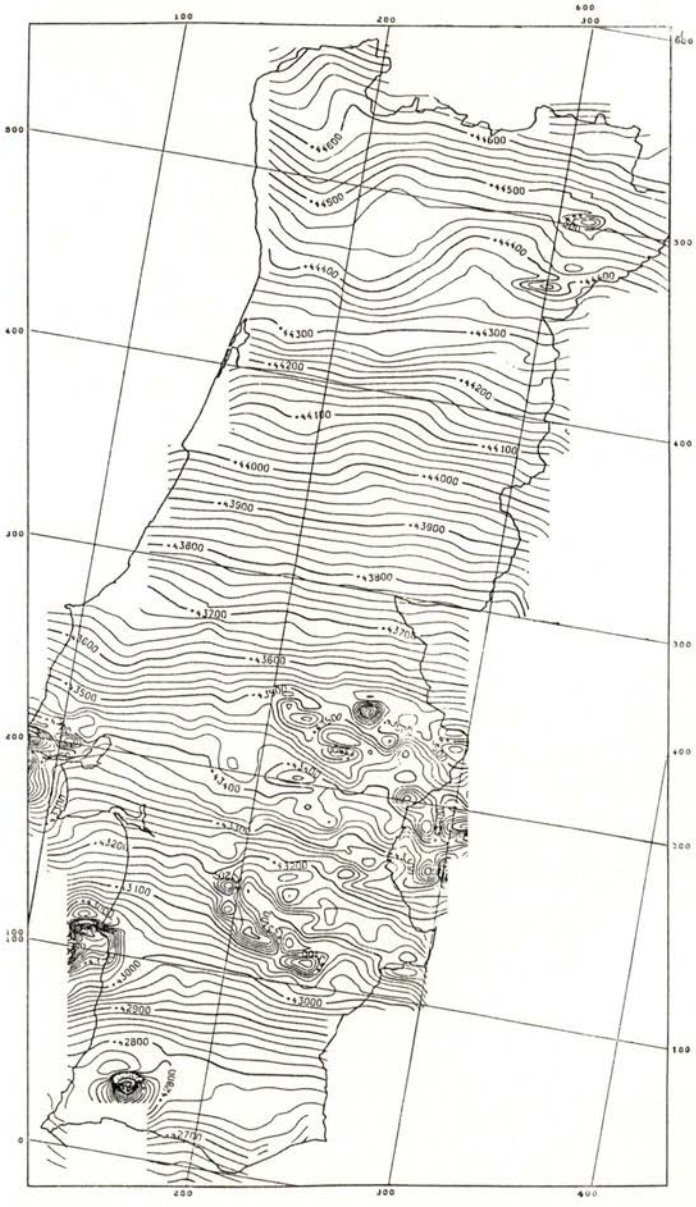

Fig. 8 — Total intensity magnetic field map for Portugal for the 1980.0 epoch and an altitude of 3000 m. Isovalues are plotted 20 nT apart.

3 – REPRESENTATION OF THE MAIN FIELD

The analysis of aeromagnetic data for the southern panel (Miranda et al.) mainly pointed out the implications of the lateral extension of the survey in the possibility of obtaining a realistic local expression for the main field. On the other hand it was assumed that the plan approximation to the measured data did not differ significantly from the IGRF80 model. Thus a slightly modified IGRF80 expression for the main field was adopted.

The addition of data for the northern panel modifies this picture: we have now a better knowledge of the north-south variation pattern of the geomagnetic field over Portugal. Now the relative importance of the southern anomalies for the numerical calculation is smaller. However, the relatively short longitudinal extension of the survey inhibits the clear description of the main field in this direction.

An orthogonal polynomial analysis of the survey data (Grant, 1957; Berezin et al., 1965) was carried out to detect the existence of a cut-off between the deep and the shallow components of the field. The normalized coefficients are partially listed in the table of Fig. 9 (a). As was already noted for the southern panel we cannot clearly identiy any gap between the two contributions.

x (E-W degrees)

0	1	2	3	4	5
0	4449441	867319	2133708	388194	150428
310364467	93932	4969347	1405616	1620564	31898
49201	702045	69534	896719	23009	1474
470723	7478	171204	459	6407	42460
10480	34459	143038	67226	55882	23398
12316	29811	4828	991	4777	11441
43965	6286	14755	1146	21874	881

(a) Normalized coefficients for the gridded data. Dimension of the matrix (55,18) corresponds a grid covering a rectangular area of 540 km by 170 km.

0	0	0	0	0
125556442	310364467	257936411	211921565	165135749
46802	49201	16146	233	12143
13361	470723	203701	72554	44151
16828	10480	30452	76732	53729
7311	12316	7306	355	6301
2859	43965	30293	781	2411
9647	10	12	4200	5
5907	31	14916	10204	3987
9611	1	945	6337	20144

(b) Values of the normalized coefficients for sucessive «windows» of dimensions (55,18), (51,18), (47,18), (43,18) and (39,18). We show only the polynominals in y (north-south) for the zero-order in x (east-west).

Fig. 9 — Table of the orthogonal polynomial analysis of the gridded data.

If we take successive nested windows of the matrix that represents the gridded data and perform again the orthogonal polynomial analysis we can detect a gradual change of the relative importance of the normalized coefficientes (see Fig. 9 (b)) avoiding the use of a high degree polynomial expression for the normal field.

The least squares first degree polynomial expression, which appears to be least sensitive to the contraints resulting from the small survey area, is:

$$F = 43770.0 - 0.14137 \times 10^{-3} \times (x - 200000) + 3.73649 \times 10^{-3} \times (y - 300000) \ \text{nT}$$

where $(x - 200000)$ and $(y - 300000)$ represent the Hayford Gauss coordinates, in meter, referred to the cartographic «central point» of Portugal.

If we compare the IGRF80 with this approximation (see Fig. 10), as we did in the southern panel processing, we arrive of a different conclusion now; in spite of the very small difference between the mean values of both fields over Portugal (1.6 nT) there is a clear difference in the north-south gradient, mainly in the north. The choice between the two models remains difficult as we have no

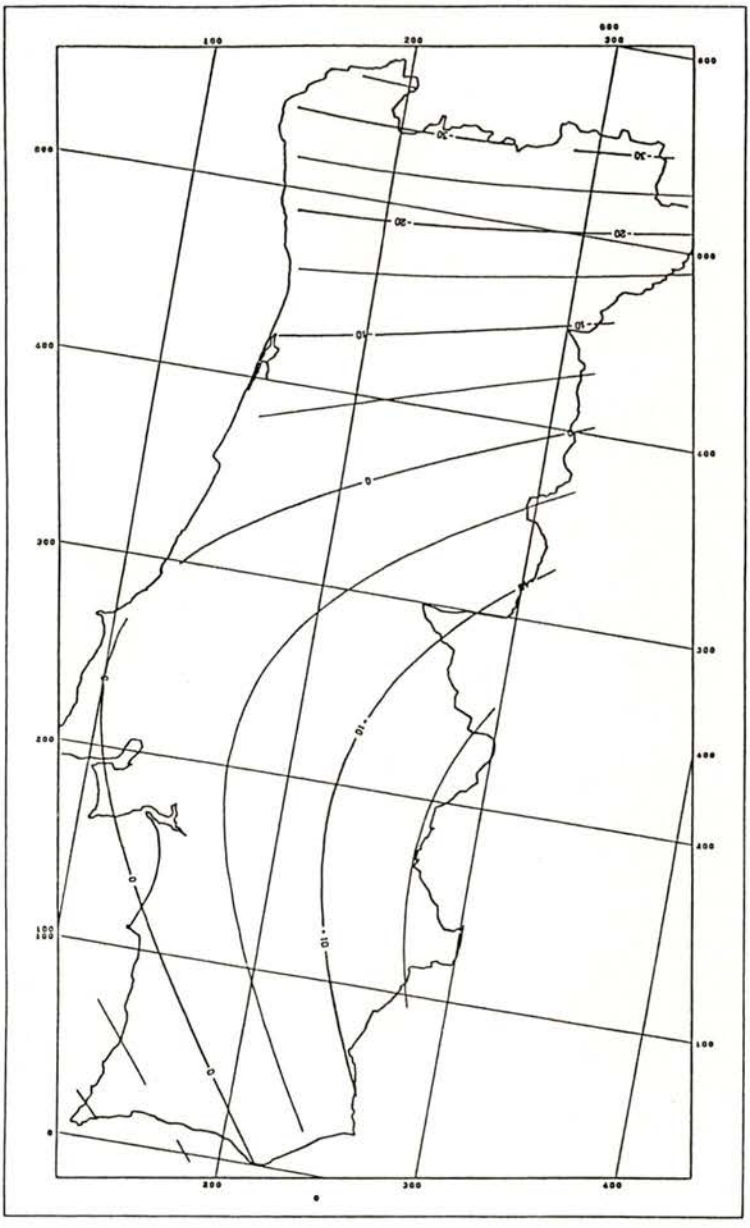

Fig. 10 — Difference between IGRF80 and a planar LS approximation of the survey data. Isovalues are plotted every 5 nT.

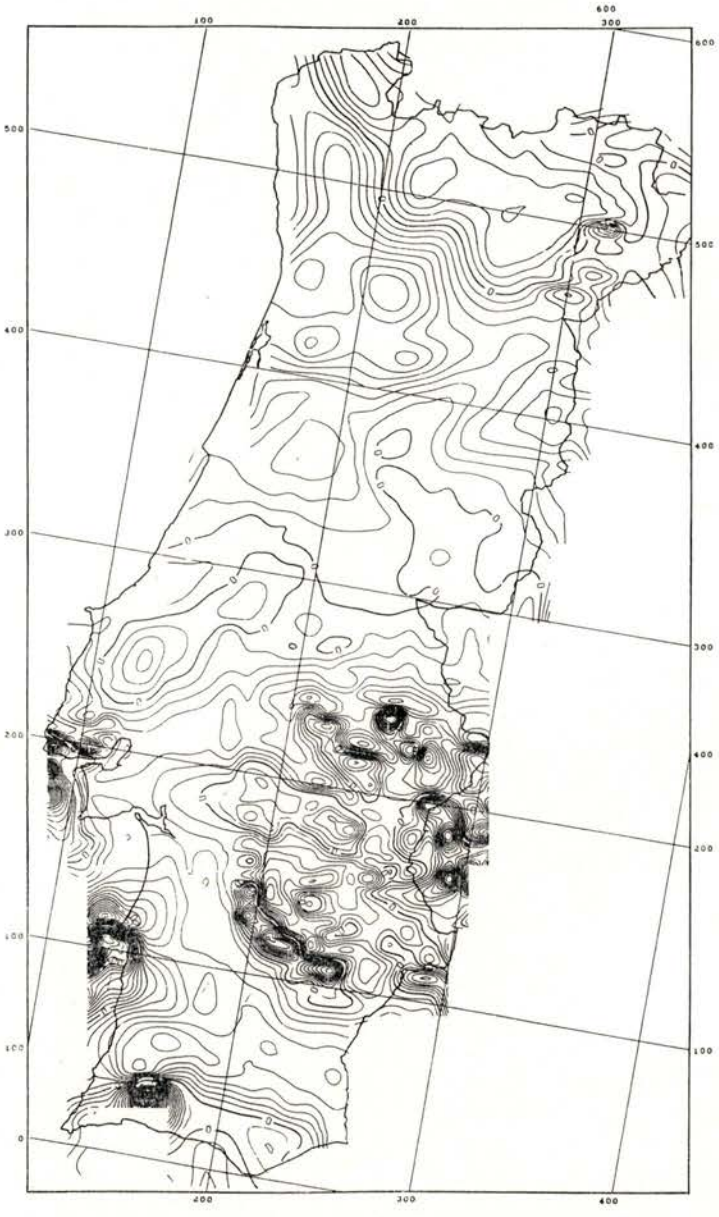

Fig. 11 — Aeromagnetic anomaly map for Portugal.

reliable information on the total intensity field over the rest of the Iberian Peninsula. While the Spanish aeromagnetic survey is not accomplished (and there is no equivalent available information from other sources, such as satellite — derived magnetic cartography) it is not possible to obtain a precise description of the main field.

The option for the IGRF80 as a normal field model appears to be the only coherent possibility as it is a well known model, also used as a reference for many other magnetic surveys. The misfit between the two models must be related in some way to the medium and large wavelength crustal anomalies that are not included in the global models (such as the IGRF) but whose wavelength (hundreds of kilometers) is of the same order of magnitude as this aeromagnetic survey.

The corresponding anomalies are presented in Fig. 11.

4 – ACCURACY OF THE SURVEY

The remarks made when discussing the accuracy of the southern panel of this survey are generally applicable now.

The proton precession magnetometer employed in the field operations has a nominal accuracy of ± 1 nT. The smoothing effect needed to filter the flight lines is similar for both panels although the distribution is a little larger for the northern panel because the field records of flight lines 25 and 27 are somehow disturbed as discussed above. The noise envelope can be so estimated as 2 by 3 nT.

Location errors over the land are not very serious where the cartography is updated, as an error of 50 meters in an area of large horizontal gradient (20 nT/km in the south but smaller in the north) causes an uncertainly of only 1 nT. There are some regions where the available cartography is old, and a greater error can be introduced because few terrain references are available for photo identification. We estimate the maximum location error as 3 nT over the land. However, this value can be greater over the sea, where the coordinates are interpolated or extrapolated.

The errors due to the variation of flight height and the non-homogeneity of the daily variation are roughly estimated from

the residual cross errors. The two panels show a similar behavior and we can take 5 nT as a standard deviation of the cross error.

The new element that can be used to judge the final accuracy of the survey is the misfit between the two panels of about 6.0 nT. This is a measure of the uncertainty in the absolute values attributed to the reference stations (taking no account of any systematic error in Coimbra mean values) to which all data are reduced.

In conclusion, all the error sources produce a net uncertainty in the absolute values that can be roughly estimated at less than 10 nT. We must emphasize that the major part of this uncertainty is a smoothly varying quantity, distributed along the flight lines during the levelling processes, or an adding constant of the survey. Thus, the interpretation of the corresponding anomalies will not be biased by spurious or systematic effects.

We thank the Instituto Nacional de Meteorologia e Geofísica, the Força Aérea Portuguesa and the Laboratoire de Géomagnétisme of the Institut de Physique du Globe de Paris for all support needed to accomplish this work.

REFERENCES

BEREZIN, I. S., ZHIDKOV, Z. P., «Computating Methods». Pergamon Press, London, 1965.

GALDEANO, A., 1980,Thesis presented to the University of Paris VII.

GRANT, F., 1957, A problem in the analysis of Geophysical data Geophysics, vol. **22**, 309/344.

LE MOUEL, J. L., 1969, Thesis presented to the Faculté de Sciences de l'Université de Paris.

MIRANDA, J., GALDEANO, A., MENDES VICTOR, L. A.,«Aeromagnetic Survey of Portugal — southern panels». Portgal. Phys, vol. 18, fasc. 1-2, pp. 77-98, 1987.

REINSCH, C. H., 1967, Smoothing by soopline functions Num. Math. **10**, 177/183.

A THREE-COMPONENT MODEL FOR THE ASSESSMENT OF THE IMPACT OF HIGH-CO_2 LEVELS AND ITS APPLICATION IN PORTUGAL

R. J. AGUIAR

LNETI — Departamento de Energias Renováveis
Estrada do Paço do Lumiar, 1699 Lisboa Codex

AND

F. D. SANTOS

Instituto Nacional de Meteorologia e Geofísica
Rua C. do Aeroporto de Lisboa, 1700 Lisboa
Portugal

(Received 30 May 1988)

ABSTRACT — A simple model is described which enables preliminary studies of the impact in Portugal of the release of large quantities of carbon dioxide to the atmosphere, due to man-related activities. The model assembles three separate previous models for i) the carbon cycle, ii) the climate system and iii) the biosphere response. Calibration and sensitivity studies are done and the results yielded by the model with suitable (conservative) estimates on the CO_2 future release leads to the identification of temperature as the main factor influencing the distribution of the bioclimatic regions in Portugal and indicates a significative impact on its biosphere, namely in the appearance of predesertification areas.

1 — INTRODUCTION

The continuous and increasing release of carbon dioxide into the atmosphere since the Industrial Revolution, due to growing industrial and agricultural activities, tends to disrupt the natural equilibrium of the CO_2 reservoirs existing on Earth.

As a consequence, it is calculated [1] that about 56 % of the CO_2 released by mankind remains in the atmosphere, leading to an enhanced greenhouse effect. The predicted rise in the average temperatures may have several important consequences on the

Earth's climate system: melting of ice covers, rise in sea levels, modifications in the general atmospheric circulation, namely in the hidrological cycle, and in the oceanic movements.

In principle, the higher CO_2 levels would also increase the productivity of the biosphere. However, detailed models are necessary, in view of the complexity of the carbon cycle and of the atmospheric circulation and also in view of the variety of responses of different plants to the conditions of temperature, soil, available radiation and available moisture.

Three areas of modelling can then be distinguished, where: i) models deal with the carbon cycle, using a CO_2 input based on some kind of economic scenario; ii) models simulate the general circulation of the atmosphere, in a way similar to the meteorological prediction models, and iii) models simulate the response of plants to different environmental conditions. In the order depicted above, each level of simulation should use the results of the anterior level, enabling then the computation of a global time response of the climate/biosphere system. However, this is seldom done in current literature.

In the present work, simplified models for the three aspects mentioned above are applied for the particular case of Portugal. Comparison is made of the results obtained with i) average past meteorological conditions and ii) meteorological conditions predicted by the model, assuming a conservative estimate for the future consumption of fossil fuels and deforestation. This will permit a first assessment of the impact on Portugal of high atmospheric-CO_2 levels.

2 — MODELLING THE CO_2 CYCLE

2.1 — *Description of the model*

The four main reservoirs of carbon on Earth are the sedimentary rocks, the oceans, the biosphere and the atmosphere. The CO_2 cycle model does not include the first reservoir, because it is known that the estimated fluxes from and to the sediments are only about 10^{-3} to 10^{-4} of the atmospheric carbon mass per year.

On the other hand, the oceanic reservoir is splitted in a superficial (mixed) layer and a deep layer, accounting in this

simplified way for the convection, diffusion and mixing processes that occur in the ocean.

Thus, the CO_2-cycle model consists of four reservoirs, connected by fluxes with each other as shown in Fig. 1. The dynamic equilibrium existing in this system is perturbed by two fluxes representing human activities: a deforestation flux and a fossil combustible flux.

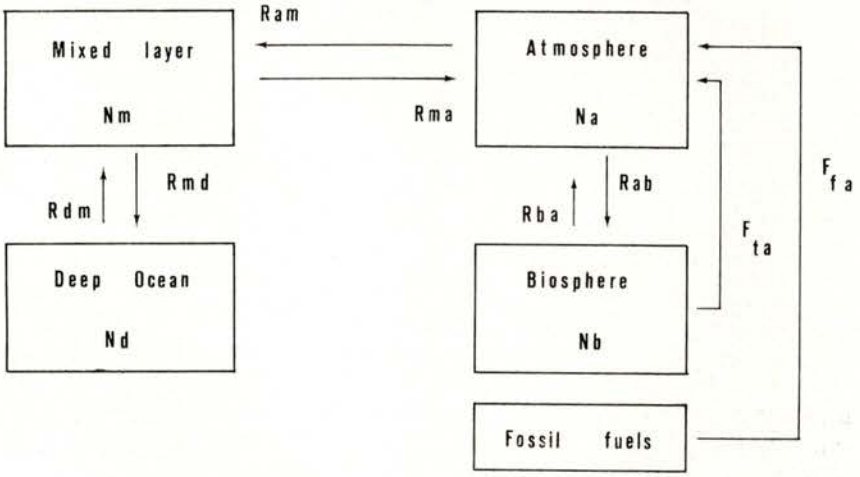

Fig. 1 — Box model for the CO_2 cycle.

It is worthwhile to note that the fossil organic matter reserves, i. e. carbon, oil and natural gas, are considered to be part of the biosphere; however, since they do not interact with other reservoirs in any way except by the man-induced flux, their mass must not be taken into account for describing the biosphere's behaviour.

The fluxes R_{ij} between carbon reservoirs with contents N_i are described by linear expressions, as follows:

$$R_{ij} = K_{ij} \times N_i \qquad (1)$$

where the K_{ij} are inverses of residence times for atoms of carbon transiting from reservoir i to reservoir j. These indexes can take the values i, j = a, b, m, d for atmosphere, biosphere, mixed and deep ocean layers, respectively.

However, since the transfer of carbon to the biosphere should depend in some way on the mass of the biosphere itself and since upper limits to growth are known to exist (eg. water, nutrient and radiation availabilities), an exception must be made for R_{ab}, in which case a logarithmic form [1] was chosen:

$$R_{ab} = K_{ab}\ (N_{ao}\ (1 + e\ \mathrm{Ln}(N_a / N_{ao}))). \qquad (2)$$

Here, N_{ao} is the pre-industrial atmospheric content of CO_2 and e is a biotic growth factor, accounting for the fertilizing effect of carbon dioxide on the biosphere.

Tests with various forms for the deforestation and fossil fuel consumption (eg. linear, logarithmic, exponencial) [2] and comparison with observed data on CO_2 atmospheric levels [1] indicate that realistic behaviour of the model is possible when a logistic form is taken for both fluxes:

$$F_{ia}(t) = U / (1 + \exp\{4B(t_m - t) / U_i\}) \quad i = f, t \qquad (3)$$

where f stands for fossil fuel consuption (t for deforestation), U is the pre-industrial total content in carbon of the known economically exploitable reserves (terrestrial living biomass) and B is the maximum production rate (deforestation rate), taking place at time $t = t_m$.

The complete set of differential equations describing the CO_2-cycle model will be then

$$\begin{aligned}
dN_b/dt &= -K_{ba}\ N_b(t) + R_{ab} - F_{ta}(t) \\
dN_m/dt &= K_{am}\ N_a(t) + N_{dm}\ N_d(t) - K_{ma}\ N_m(t) - \\
&\quad - K_{md}\ N_m(t) \\
dN_d/dt &= K_{md}\ N_m(t) - K_{dm}\ N_d(t) \\
dN_a/dt &= -K_{am}\ N_a(t) + K_{ba}\ N_b(t) + K_{ma}\ N_m(t) - \\
&\quad - R_{ab} + F_{fa}(t) + F_{ta}(t)
\end{aligned} \qquad (4)$$

with R_{ab}, F_{fa} and F_{ta} given by expression (2) and (3).

2.2 — *Calibration of the CO_2-cycle model*

With the anthropogenic fluxes set to zero, and assuming a linear form for R_{ab}, the set of equations (4) can be written in a

matricial form, $dN/dt = AN$. it can be shown that a equilibrium state exists, the one that corresponds to the eigenvalue zero of the matrix of coefficients A. The corresponding eigenvector, normalized by the atmospheric carbon content [2, 3], is $\{1, K_{ab}/K_{ab}, K_{am}/K_{ma}, (K_{am}\ K_{md})/K_{ma}\ K_{dm})\}$. Once estimates are known for the interaction constants K_{ij} and contents N_i (see for instance [1, 3]), it is possible to adjust them consistently with the stationary state eigenvector. The values found for the present model are listed in Table I.

TABLE I — Numerical constants used in the CO_2-cycle model

Reservoir content in 1975 (10^{12} Kg C)	Interaction constants (year^{-1})	
$N_a = 710$	$K_{ab} = 1/21.57$	$K_{ba} = 1/28.60$
$N_b = 815$	$K_{am} = 1/\ 6.30$	$K_{ma} = 1/\ 7.36$
$N_m = 815$	$K_{md} = 1/33.12$	$K_{dm} = 1/16.00$
$N_d = 42000$		

Pre-industrial atmospheric CO_2: $N_{ao} = 630 \times 10^{12}$ Kg C
Biotic growth factor: $e = 0.5$

For the man-induced fluxes, values of maximum rates B and corresponding times of ocurrence t_m were adjusted so that the model would fit to past trends; the values obtained are presented in Table II.

TABLE II — Numerical values for the logistic fluxes of deforestation and fossil fuel consumption

	U (10^{12} Kg C)	B (10^{12} Kg C year^{-1})	t_m
World forests:	835	9	2000
Fossil reserves:	4400	40	2070

Fig. 2 represents the predicted evolution of carbon content for the biosphere and atmosphere, according to this model, integrated with a standard Runge-Kutta method.

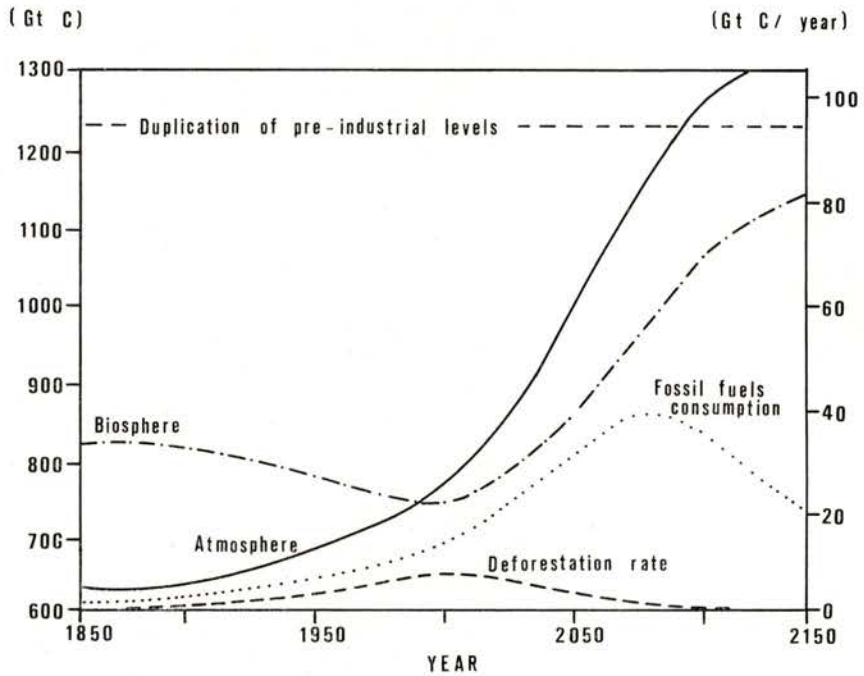

Fig. 2 — Evolution of carbon content of atmosphere and biosphere under logistic deforestation and fossil fuel consumption.

3 — VERTICAL ONE-DIMENSIONAL ATMOSPHERIC MODEL

3.1 — *Thermodinamic structure of the atmosphere*

A radiative-convective type atmospheric model is chosen in view of its relative simplicity for implementation and of the good agreement this class of models shows with more complex ones, as the GCM's (tridimensional global circulation models). In the radiative-convective models, the (unidimensional) structure of the atmosphere for average conditions is evaluated considering the equilibrium between the radiative flux and a parametrized con-

vective heat flux; the temperature profile is adjusted to be less or equal to the «stable» thermal gradient of 6.5 K/Km.

The model of Weare and Snell (1974) is chosen as it gives a more complete treatment of the atmosphere than others, both because its analytical description seems superior to the use of discrete levels or of a standard atmosphere and because it introduces a parametrization for clouds and precipitation processes [5] (instead of a fixed cloudiness).

Consider first the thermodinamic equilibrium of a vertical column of atmosphere standing over a plane surface representing Hidrosphere, Litosphere and Criosphere. A particle of humid air suffers a quasi-static expansion and rises through a stable environment, mantaining the equilibrium in the gravitational field. Using essentially the law for ideal gases, the geostrophic equilibrium aproximation and the Clapeyron-Clausis equation it is possible [2] to derive equations for the particle temperature and water content dependence on the height z:

$$\frac{\partial T}{\partial z} = - \frac{\left(1 + \frac{n_{2A}(z)\ \Delta H_i}{n_1\ R\ T(z)}\right)\left(1 + \frac{n_{2B}(z)}{n_A(z)}\right) M(z)\ g}{C + C_B \frac{n_{2B}(z)}{n_A(z)} - \frac{A}{n_A(z)} + \frac{n_{2A}(z)\ \Delta H_i^2}{n_1\ R\ T^2(z)}} \tag{5a}$$

$$\frac{\partial n_{2A}}{\partial z} = - \frac{n_A \left(C - \frac{\Delta H_i}{T(z)} + n_{2B}(z)\ C_B - A\right)}{\frac{n_1\ R\ T(z)}{n_{2A}(z)} + \Delta H_i} \tag{5b}$$

where:

- M = average molecular mass of humid air
- g = acceleration of gravity (9.8 m s^{-2})
- R = universal constant for ideal gases
- A = parameter for the convective transfer of entropy
- T = temperature
- C = average specific heat for the mixture air-water vapour
- C_B = specific heat for condensed water
- n = number of moles of component j
- ΔH_i = latent heat for: i = 1 — vapour/liquid transition; i = 2 — vapour/ice transition

and where quantities related with various components are indexed with

j = 1 for dry air,
j = 2A for water vapour,
j = 2B for condensed water (liquid and/or solid).

Under the condition of water conservation, the water condensed in a rise of δz is

$$\delta n_{2B} = - \frac{\partial n_{2A}(z)}{\partial T(z)} \frac{\partial T(z)}{\partial z} \delta z . \qquad (5c)$$

It is admited that only a very small fraction of the condensed water, 1 - f, remains in the particle, in the liquid form if $T(z) > 273.15$ K, and in the solid state otherwise. The remaining fraction, f, falls to the surface. In this way the existence of clouds and precipitation in the atmosphere is accounted for.

The set of partial differencial equations (5) was solved with a Euler method and vertical steps of one meter, with the averaged (annual, global) boundary conditions $T(0) = 288$ K, $n_{2B}(0) = 0$ and a value for $n_{2A}(0)$ deduced from a surface average pressure of $P(0) = 1013$ hPa and a relative humidity of $U(0) = 0.75$.

The atmosphere was found to be stable (i. e. thermal gradient less or equal to 6.5 K/Km) when $A = -14.5$ J/mol K. The value of f that yielded average total precipitable water compatible with actual conditions was f = 99.589 %. The vertical distribution of temperature, water vapour and density of condensed water for a set of surface temperatures are representd in Figs. 3 through 5.

While temperature and water vapour seem to follow a realistic pattern, it is clear that no cloud has the vertical extent and the vertical distribution of water shown in Fig. 5. However, note that this «diffuse» cloud is not a model of real clouds, but rather a representation of average conditions of clear and overcaste skies throughout the year.

3.2 — *Particulate constitution of clouds*

The distribution of condensed water in the form of droplets or ice cristals (depending on temperature) is assumed to be given

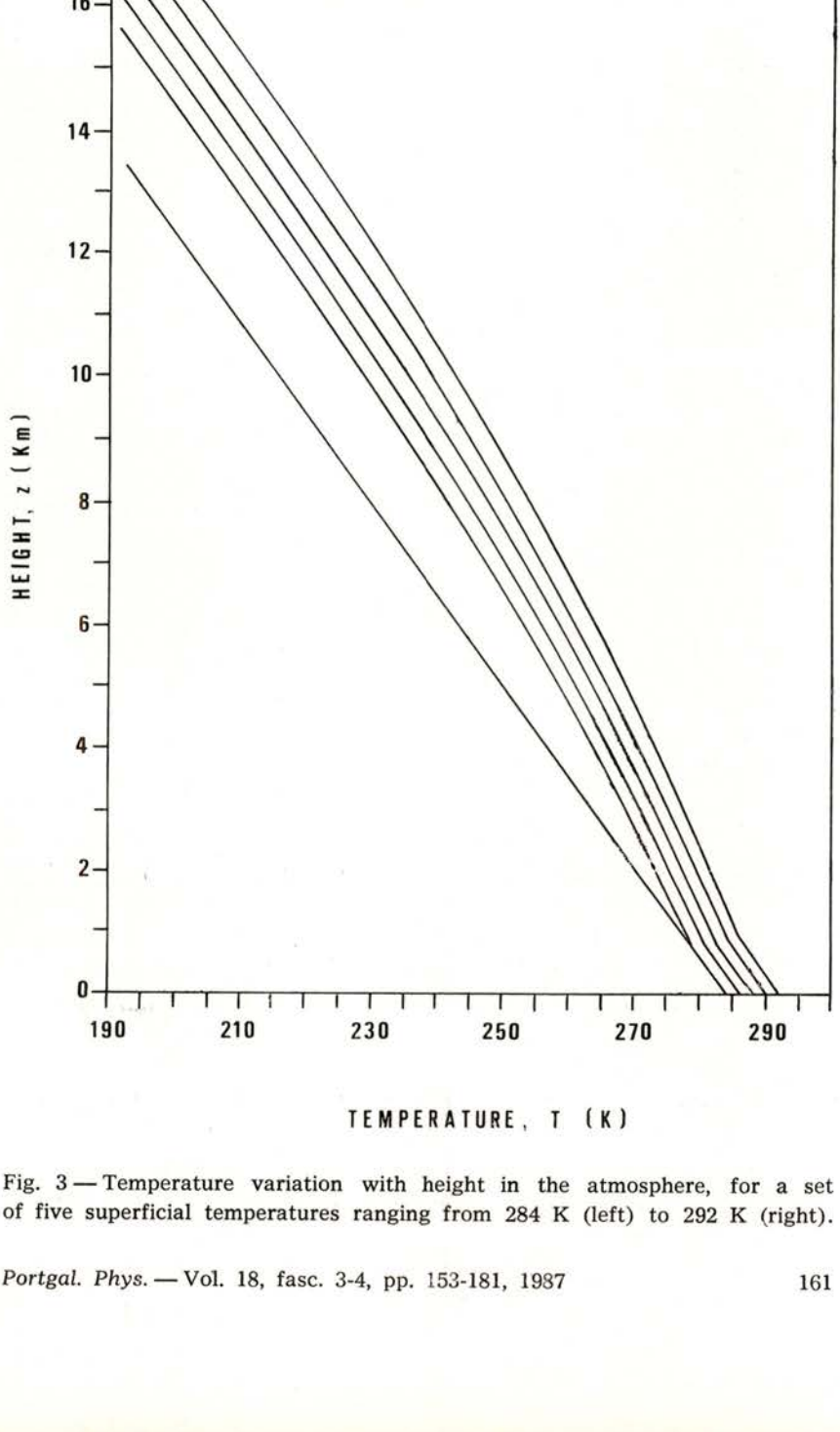

Fig. 3 — Temperature variation with height in the atmosphere, for a set of five superficial temperatures ranging from 284 K (left) to 292 K (right).

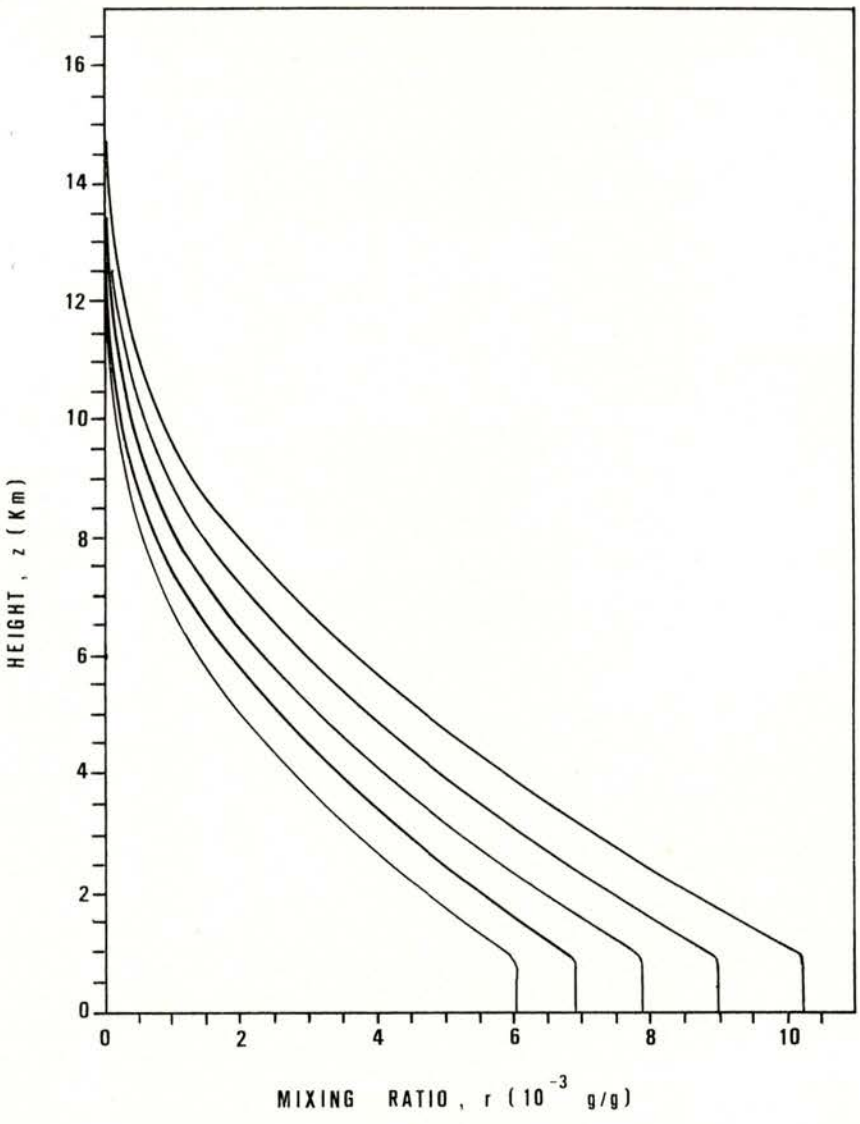

Fig. 4 — The same as in Fig. 3, for water vapour content.

by a size-distribution law similar to that used by Deirmendjian (1964)

$$n(r) = ar^{\alpha} \exp(-br^{\gamma}) \qquad (6a)$$

where n (r) is the volumic concentration of particles — assumed sphearical — with radius r. The constant a is related with the

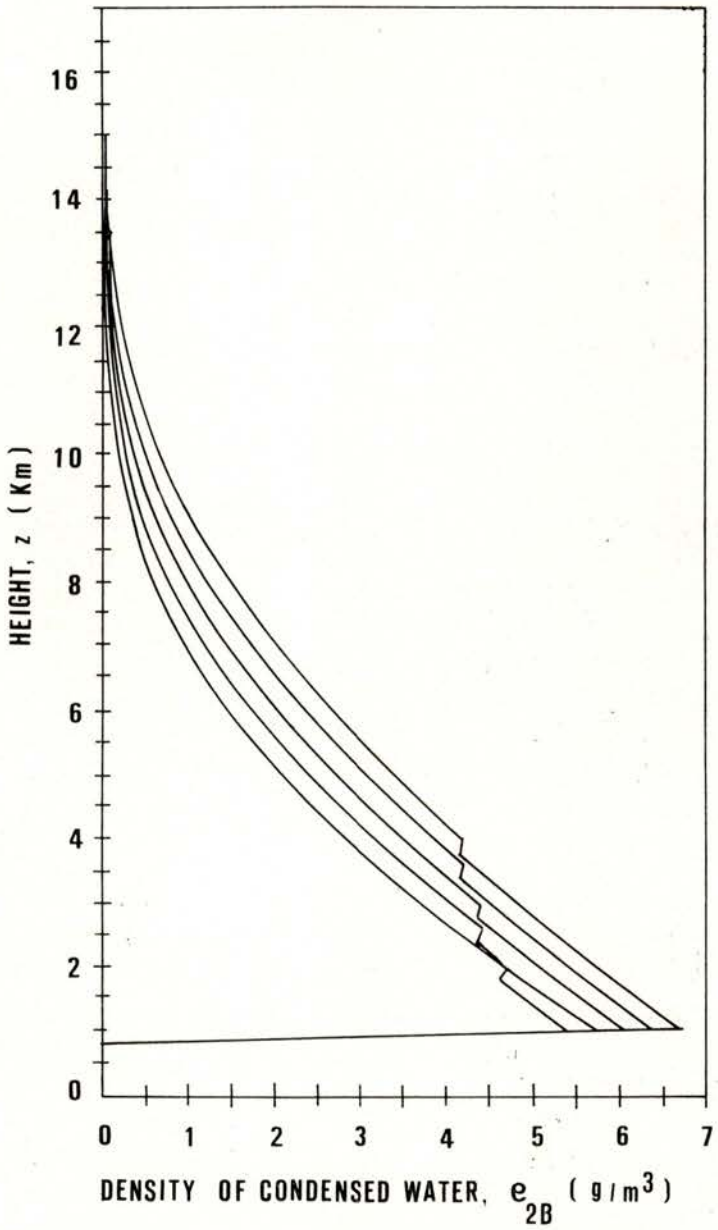

Fig. 5 — The same as in Fig. 3, for condensed water content.

total number of particules per unit volume and b to a modal droplet radius, $r = 4\ \mu m$. The positive constants α and γ can be fitted so that the function n (r) will follow the experimental distributions for cumulus clouds, yielding $\alpha = 6$, $\gamma = 1$. Generalizing n (r) to n (r, z), for each level z, it is possible to relate a (z) to the condensed water volumic mass ρ_{2B} (z) :

$$n(r, z) = \frac{3 \times 1.5^{10}\ r_2}{4 \times 9!\ \pi \rho}\ \rho_{2B}(z)\ r^6\ \exp\{-1.5\ r\}\ \mu m\ m^{-3} \quad (6b)$$

Here ρ is the volumic mass of the droplets, $r_2 = 12\ \mu m$ is a superior limit to the particle radius and both ρ_{2B} and ρ are expressed in g/m^3.

3.3 – *Downward radiative flux*

The analytic solution derived by Sagan and Pollock (1967) for the radiative transfer equation of Chandrasekar in the case of a plane-stratified atmosphere is used. Some assumptions for this solution are i) anisotropic non-conservative diffusion occurs because of the dielectric particles suspended in the atmosphere ii) Mie theory is valid (particle size much smaller than radiation wavelenght) iii) the Schuster-Schwartschild two-flux aproximation, modified by the use of an assimetry factor B (see Fig. 6), is

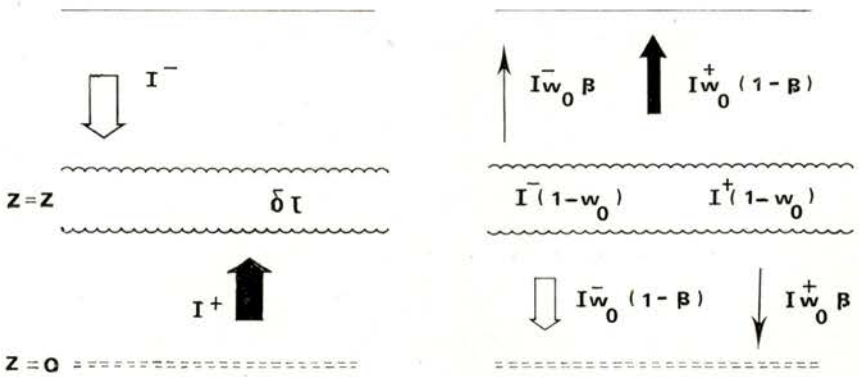

Fig. 6 — Scheme of the two-flux approximation (for visible radiation).

assumed. With the boundary condition $t(\tau) = 1$ for a null optical depth $\tau = 0$, the fractions of absorbed, a, reflected, r and transmited energy by the atmosphere, t, can be written [7]:

$$a = 1 - r - t \tag{7a}$$

$$r = \frac{(u+1)\ (u-1)\ (\exp\{\tau'\} - \exp\{-\tau'\})}{(u+1)^2\ \exp\{\tau'\} - (u-1)^2\ \exp\{-\tau'\}} \tag{7b}$$

$$t = \frac{4u}{(u+1)^2\ \exp\{\tau'\} - (u-1)^2\ \exp\{-\tau'\}} \tag{7c}$$

where $u = (1 - w_0 + 2Bw_0)/(1 - w_0)$ and $\tau' = \sqrt{3}\ u\ (1 - w_0)\ \tau$. The parameter w_0 is called the albedo for single diffusion and takes the values $w_0 = 0.999$ for water and $w_0 = 0.95$ for aerosols. Also, the assimetry factor is $B = 0.078$ and $B = 0.18$ for water and for aerossols respectively.

For the aerosols a value of $\tau = 0.1$ is assumed. The determination of τ for the case of water is somewhat complicated. Using experimental data for the extintion coefficients in the case of water droplets [8] and the Planck equation for the spectral energy density, a very simple relation could be obtained [2] with the help of numerical integrations:

$$\tau(z) = 0.074815\ W(z) \tag{8}$$

where W(z) is the water content of the cloud from its base to level z.

Since the reflectivity R_{AB} of two superposed layers A and B overlying a plane surface of refllectivity r_C can be given by [5]

$$R_{AB} = r_A + \frac{t_A^2\ [r_C t_B^2 + r_B(1 - r_B r_C)]}{(1 - r_B r_C)\ (1 - r_A r_B) - r_A r_C t_B^2} \tag{9}$$

the total terrestrial albedo α will be calculated as a simple average between the case of a cloud layer on the top of an aerosol layer and the case corresponding to the inverse situation. The transmissivities and reflectivities of cloud and aerosol are known from the respective optical depths and from the equations (7), but a

parametrization for the ground average reflectivity r_C depending on temperature must be obtained. The empirical equations of Hollin [9] and of Morner [10] are used, giving:

$$\langle\Theta_S\rangle = 65 - 0.1\ [T(O) - 288.] \quad (10a)$$
$$\langle\Theta_N\rangle = 65 - 2.0\ [T(O) - 288.] \quad (10b)$$
$$\langle\Theta\rangle = (\langle\Theta_N\rangle + \langle\Theta_S\rangle)/2 \quad (10c)$$

$$r_C = (1 - \sin\ (\langle\Theta\rangle))\ r_i + \sin\ (\langle\Theta\rangle)\ r_o \quad (11)$$

where the equations (10a, b) correspond to the amplitudes Θ, in degrees, of the southern and northern ice caps, respectively. In equation (11) the reflectivity of ice r_i and of a weighted average of other surfaces (including ocean water) r_o are given by $r_i = 0.60$ and $r_o = 0.07$.

3.4 — *Upward radiative flux*

In this section the infrared radiation absorption is modelled for the main absorbers in the atmosphere: water, carbon dioxide and ozone. The approach of Rodgers [11, 12], which avoids the integrations through the complicated spectrum lines, is followed. An emissivity function ε is parametrized: for the whole spectrum in the case of water; of the 667 cm^{-1} band in the case of CO_2.

The upward radiation flux at level z, F (z), can be written

$$F(z) - F(O) = \int_0^{U(z)} (B(u) - B(U))\ (d\varepsilon / du)\ du \quad (12a)$$

where B stands for the total Planck function, i. e. B_ν for each wave number ν integrated over all the wave numbers. An integration in altitude was substituted in Eq. 12a by an integration over total absorber quantities u, from the surface up to the height z, using the formula [12]:

$$u(z, 0) = 1.66\ (M_1/R) \int_z^0 (r_B(z)/T(z))\ P^2(z)\ \exp\ [\beta(T(z) - 250)]\ dz \quad (12b)$$

which includes the correction due to the variation of absorption with temperature (exponencial term with $\beta = 0.005$) and Elssasser's factor 1.66 to account for integration over all zenithal angles. In Eq. 12b, P stands for pressure, M_1 for molecular mass of dry air and r_B for mixing ratio of the condensed water. The definition and parametrization of water emissivity ε is as follows:

$$\varepsilon = \int_0^{\infty} A_\nu \, (dB/dB_\nu) \, d\nu_\nu = \begin{cases} \sum_{n=1}^{N} a_n \, u^2 & u < v \\ \sum_{n=0}^{N} b_n \, (\log u) & u \geqslant v \end{cases} \quad (12c)$$

where A is the absorvity at wave number ν (see Table III for the numerical values of constants a_n and b_n).

TABLE III — Numerical constants for water and CO_2 emissivity parametrizations

	H_2O	CO_2		H_2O	CO_2
v	0.001 Kg/m	0.1 atm/cm	b_0	0.5983	74.103
a_1	9.329	160.87	b_1	0.15068	19.632
a_2	— 446.4	— 326.50	b_2	0.034041	0.821
a_3	824.0	— 158.22	b_3	0.0065535	— 0.11834
a_4	259700.	—	b_4	0.0004887	—

This type of calculation differs from most radiative-convective models as it does not consider the clouds to be black bodies for infrared radiation. In fact, in this model there are no massive clouds and clear sky zones but rather a diffuse cloud, as already explained.

For the carbon dioxide, only the emissivity for the strongest band is parametrized: all the radiation absorbed by this gas will be assumed to lay in an interval of 200 cm^{-1}. In this spectral region there is superposition between the absorption bands of water and carbon dioxide.

The transmissivity of the water T_{H_2O} in this region, evaluated with a Goody type randob-line spectrum, was accounted for [11] in the expression for the CO_2 absorbed infrared flux:

$$F_{CO_2}(z) = 200 \left(\int_z^0 B_{667}(z') \; [d(\varepsilon_{CO_2}(z, z') \; T_{H_2O}(z, z'))/dz] \; dz' - B_{667}(0) \; \varepsilon_{CO_2}(z, 0) \; T_{H_2O}(z, 0) \right) \quad (13a)$$

The emissivity ε_{CO_2} is of the same form as discussed for water (see Table III), and

$$T_{H_2O}(z, z') = \exp^{r} - (km/\delta) \; (1 + km/\pi a\phi)^{1/2}] \quad (13b)$$

where m and m/ϕ are quantities similar to u (ie. absorber quantities corrected for temperature effects [2]. The remaining variables, adjusted for the region of interest, take the values $k/\delta = 7.345$ and $k/\pi a = 142.47$, already corrected with Elssasser's factor.

3.5 — *Calibrations and sensitivity study*

Figure 7 shows total, H_2O-related and CO_2-related infrared absorption from the surface, in the model's atmosphere. Comparison of simulated upward radiation flux and satellite measurements indicates some underestimation of this value. The thermodinamic equilibrium of the Earth-Atmosphere system is preserved by adjusting the emissivity of ozone, following Staley and Jurica [13]:

$$F_{O_3} = \varepsilon_{O_3} \sigma T_t^4 \quad (13c)$$

where T_t is the temperature at the top of the atmosphere and σ the Stefan-Boltzmann constant. The value obtained in this way is $\varepsilon_{O_3} = 0.008345$.

Augustsson and Ramanathan [14] found that the weak bands of CO_2 are responsible for only a small part of the greenhouse effect and that its importance rises with increasing temperatures. A percentage correction in the final temperature predictions of

the present model will be taken from their work. The effects of other greenhouse gases (N_2O, CH_4 and clorofluorcarbons) are included in the emissivity ε_{O_3}.

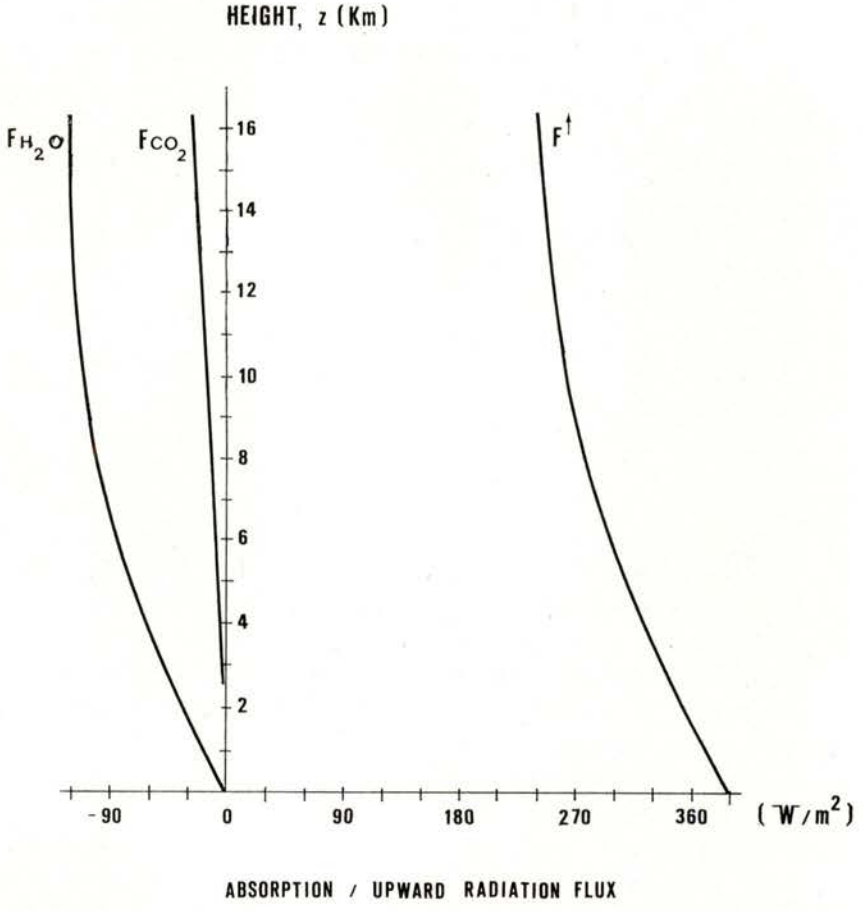

Fig. 7 — At left side, cumulative absorption of infrared radiation by H_2O and CO_2; at right, total upward infrared radiative flux in the atmosphere.

It is now important to stress that:

i) since the equations for the optical depth depend only on T(0), the total downward radiative flux (given by $S_0(1-\alpha)/4$, where S_0 is the solar constant, 1360 W/m^2) is an (implicit) function of the superficial temperature;

ii) since absorber quantities and temperatures throughout atmosphere depend only of T(0), therefore the total infrared flux E is also a function of the superficial temperature. These facts are illustrated on Fig. 8, where one can see both fluxes as a function of T(0); as required, they are equal at the present globally averaged superficial temperature, 288 K.

The stability of this climatic system can be readily investigated through the equation that describes its energy balance,

$$dQ / dt = (S_0 / 4) \ (1 - \alpha) - E \tag{14a}$$

A small change $\delta T(0)$ in the superficial temperature gives:

$$\delta (dQ / dt) = [- (S_0 / 4) \ (d\alpha / dT(0)) - - (dE / dT(0)] \ \delta T(0) \tag{14b}$$

The numerical results indicate a value of -2.0 W / (m^2 K) for δ (dQ / dt), showing that the model is quite stable, fundamentally as a consequence of strong negative feedbacks introduced by the diffuse cloud. It is therefore not suprising that (see Fig. 9) the predicted rise in superficial temperature for, say, a duplication of current atmospheric CO_2 content is of only 0.7 K, or 0.8 K if one accounts for the weak bands.

The predicted changes in temperature are smaller than those predicted by other radiative convective models and by more complex tri-dimensional GCM's. A simple modification of the present model is to consider constant the amount of water in the cloud. This is equivalent to consider the fraction of condensed water remaining in the atmosphere at each level as a temperature-dependent function. In this way, the increase in superficial temperature for $2 \times Co_2$ levels is of 2.4 K. Note that in most models of the same type, modifications in cloudiness produce only insignificant effects.

In this final form, the model is assumed to represent well the atmospheric behaviour. The biospheric response to the modifications in temperature and precipitation shall now be considered.

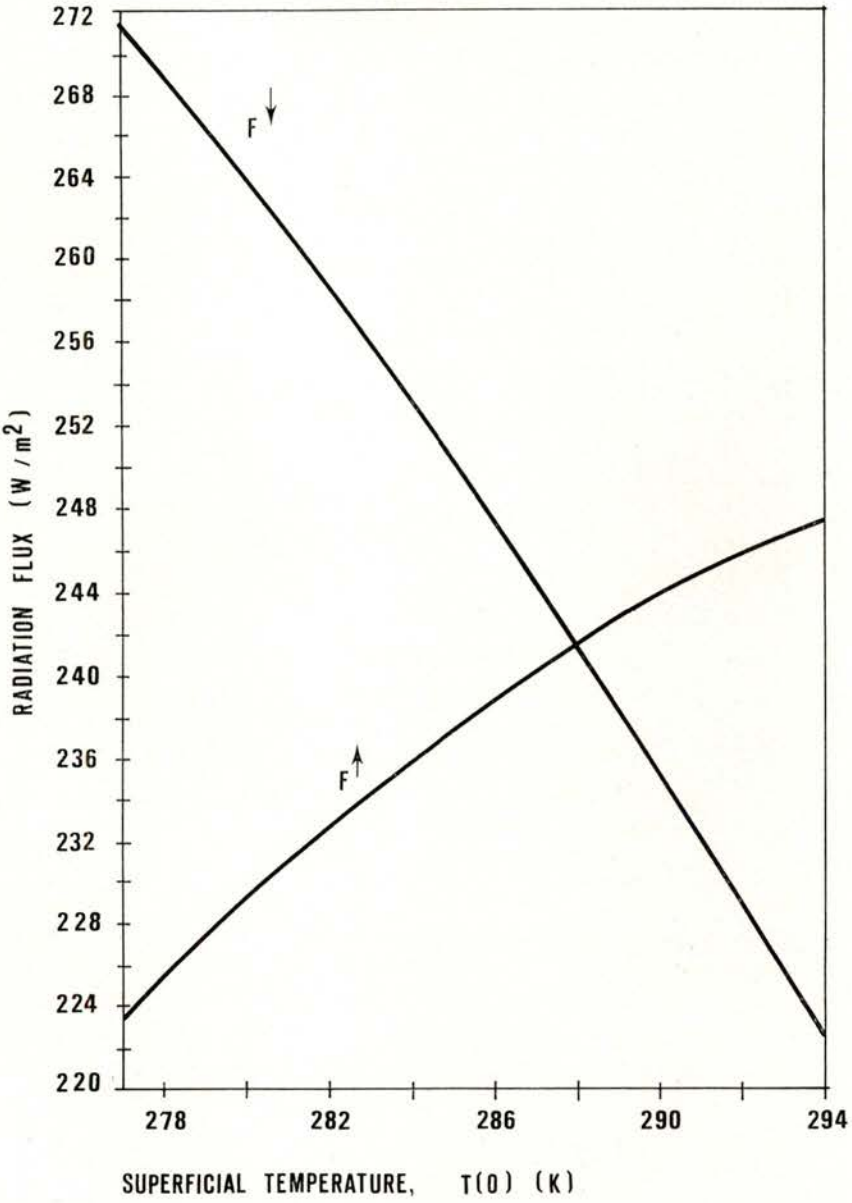

Fig. 8 — Upward and downward radiative fluxes in the atmosphere, as a function of superficial temperature.

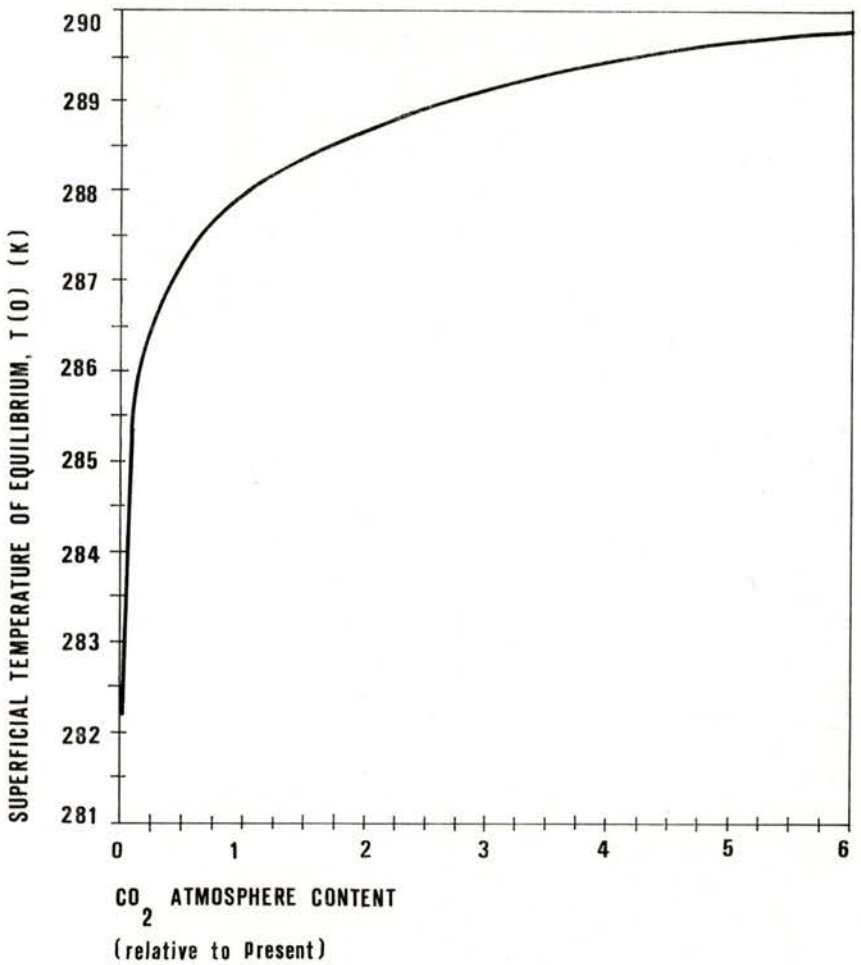

Fig. 9 — Evolution of superficial temperature as a function of CO_2 content of the atmosphere.

4 – MODELLING THE BIOSPHERIC RESPONSE

The use of a biozone classification system, depending on basic climatic indices only, was considered sufficient for the main purposes of this work, namely a preliminary impact assessment. With such a model it is possible to verify which are the changes in the boundary of the main biological-climatological regions,

resulting from the atmospheric and climatic modifications predicted by the two preceding sub-models; on this basis one can already produce (qualitative) impact estimates.

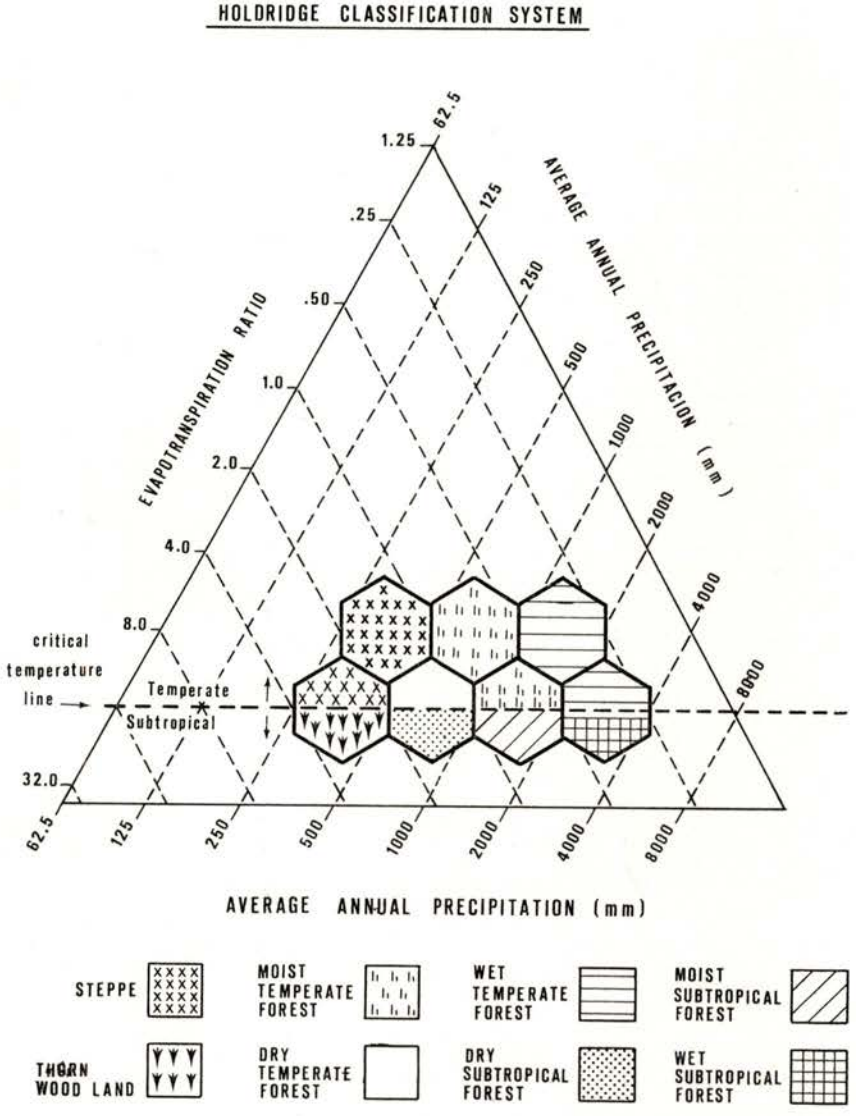

Fig. 10 — Holdridge Classification System; only some bioclimatic intervals are shown, the ones with pertinence for the present work.

The model selected is the Holdrige Bioclimatic Classification System [15] where the biozones are characterized only by annual averages of precipitation and temperature. The identification of the biozones can be made in a triangular diagram (see Fig. 10), where two sides of the triangle are precipitation axis and the left side is a potential evapotranspiration ratio axis, which is the ratio of potential evapotranspiration to annual average precipitation.

The potential evapotranspiration is defined to be equal to the quantity of water released by plants to the atmosphere, when the water available for plant growth is sufficient, but not excessive. Holdridge concluded, through the study of several ecosystems, that the average annual potential evapotranspiration can be considered proportional to the average annual biotemperature with a proporcionality constant of 58.93. The average annual biotemperature is calculated simply by setting all (monthly or daily) negative temperatures in the data to 0°C and averaging over the year.

A further subdivision of biozones results from the aplication of the criterium of existence of killing frost, due to its strong effects on the growth of plants. A critical temperature line at 18°C was assigned by Holdridge and divides Subtropical and Warm Temperate zones. However, this critical temperature can be regionally adjusted on the basis of information about real conditions.

5 — APPLYING THE THREE-COMPONENT MODEL: DISCUSSION AND RESULTS

With the sub-models discussed in sections 2., 3. and 4. for each aspect of the CO_2 problem one can finally evaluate a joint response of the earth-atmosphere-biosphere system to the man--made perturbation and apply it to the case of Portugal.

The time evolution of carbon levels in the atmosphere, under the predictions of the CO_2-cycle model and the expected evolutions of deforestation and fossil fuel consumption (Fig. 2) is introduced in the atmospheric model. For each CO_2 level, the steady-state superficial temperature is evaluated. Fig. 11 shows the time evolution of the increase in average superficial temperature. It is

seen that the temperature increase is not a linear function of carbon atmospheric levels since it slowers in time, due to the saturation of the CO_2 667 cm^{-1} absorption band. Duplication of carbon levels by the year 2080 yields an increase of 2.5 in average annual temperature.

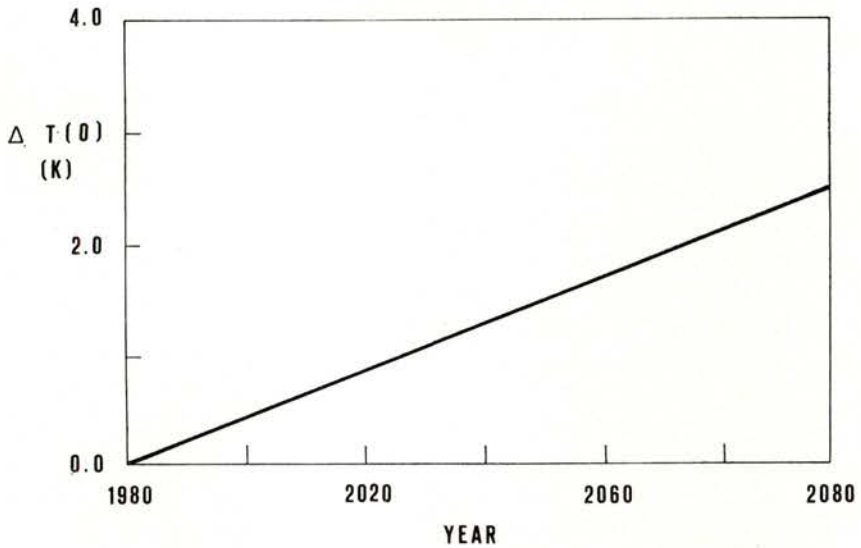

Fig. 11 — Time evolution of superficial annual average temperature, as computed from the CO_2 cycle and radiative-convective models.

An increment of 2 K seems therefore likely (in the present model, around year 2065) but the associated change in precipitation, that must also be provided for the bioclimatic model, is dubious. There are at present discrepancies between the numerical models that (as the present one) predict an increase in precipitation and some paleoclimatic analysis and empirical studies. From another point of view, the expected response of the atmosphere to higher CO_2 levels must be strongly regional-dependent, due to shiftings of the convective longitudinal cells. Indeed, the GCM's predict increments of superficial temperature for $2 \times CO_2$ levels higher than 5 K at polar regions and about only 1 K at equatorial regions. The reduced latitudinal temperature gradient induces weaker atmospheric movements, but evaporation and precipitable water would increase more than 6 %.

It is clear that one could employ the results of the radiative-convective model directly but, in view of the uncertainities explained above, it is felt that a comparative analysis can provide in this first study a better understanding of the bioclimatic response in Portugal. Therefore, when performing a comparison with average past conditions, two situations will be considered: an increment of 2 K in average annual temperature with i) an increment of 6 % in average annual precipitation in the «favourable» case; ii) a precipitation decrease of 6 % in the «unfavourable» case.

With climatological data from the 25-year period ranging from 1950 to 1975 [16], in locations providing a good coverage of the continental portuguese region, the Holdrige System was applied to yield a reference biozone distribution. This study is reflected on Fig. 12a and despite the substitution of natural vegetation, mainly by agricultural land and pine and eucalliptus forests, one can in fact see that the greater bioclimatic regions are well identified. It is speculated that consideration of seasonal precipitation oscillations and/or a finer data coverage could further separate the dryer southern and south-eastern regions from the more fertile regions of the west-atlantic coast and from the north-eastern mediterraneum micro-climates. The results yielded in the two case studies are shown in Figs. 12b and 12c.

The difference between the modified bioclimatic distributions and the reference distribution is considerable. By order of importance, the main modifications (which can be considered unfavorable from the agricultural and human point of view) are as follows:

i) substitution of the central and southern Warm Temperate Dry Woods for Subtropical Dry Wood,
ii) about a half-reduction in the Wet Mountain Forest located in the central-eastern region (around the Estrela mountain chain),
iii) appearance of a region of Subtropical Wood in the middle of the northern region.

It is important to notice that the difference between the favourable and unfavourable cases is not very important. Therefore, one can identify the average annual temperature as the decisive factor in a distribution of the bioclimatic regions in the continental Portuguese region. In fact, reduction of precipitation

instead of increment has its influence only in the moderate reduction of the nort-eastern low-mountain temperate dry woods and in

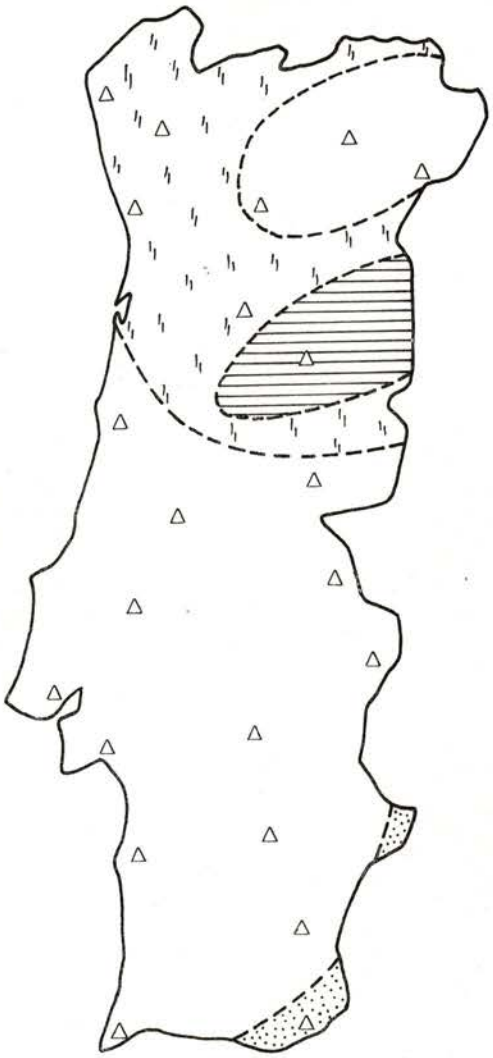

Fig. 12a — Reference bioclimatic distribution for Portugal, computed with climatological data from 1950 to 1975 observed in the locations indicated with triangles.

the appearance of small areas of dry subtropical woodlands. The latter effect indicates a desertification enhancement in those areas and nearby regions.

FAVOURABLE CASE STUDY
(+2 K, + 6% Precipitation)

Fig. 12b — Same as Fig. 12a, but with an increase of 2 K in the annual biotemperature at each station and an increase of 6 % in the annual precipitation.

This first preliminary study indicates important potentially unfavourable consequences for the portuguese biosphere. It was also shown that the uncertainity in the precipitation has little

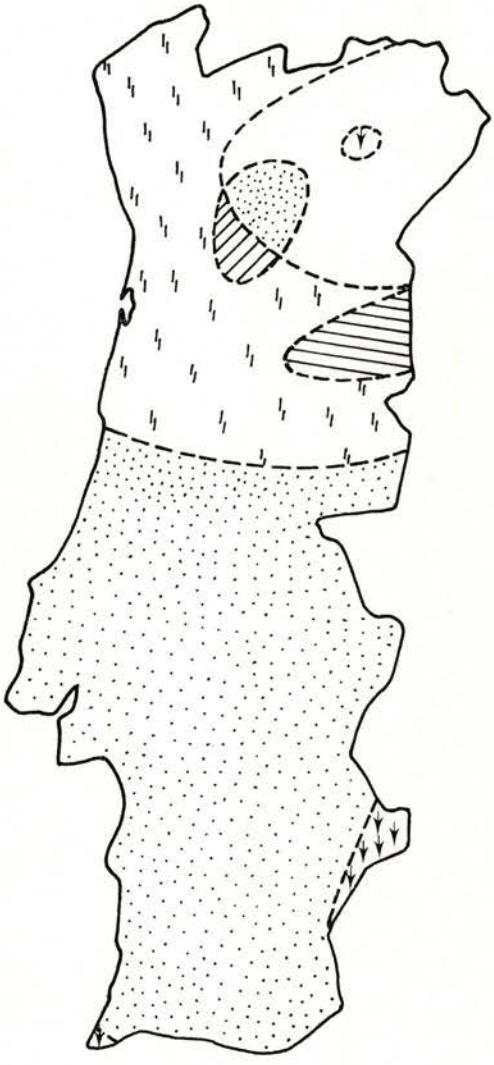

Fig. 12c — Same as Fig. 12b, but with a 6 % decrease in annual precipitation.

influence on the biozone distribution. Therefore, in further studies of CO_2 impact in the portuguese biosphere, the precipitation predicted by atmospheric models can be taken directly as input to biospheric models.

7 – CONCLUSIONS

A model that integrates the three main aspects of the CO_2 problem, namely the modelling of the carbon cycle, the atmospheric behaviour and the biosphere response was developed, calibrated and shown to be able to produce estimates of the time evolution of the earth-atmosphere-biosphere system. This model was applied to the case of Portugal and the results show that the temperature is the main factor influencing biozone distribution and that significative and potentially unfavourable changes in the portuguese bioclimatology are expected as a consequence of maninduced introduction of carbon dioxide in the atmosphere.

The present work can be extended along two directions:

i) using the fact that the described three-component model is simple and that the steady-state for each different set of boundary conditions is obtained from a single computation, it is possible to evaluate the transient response of the earth-atmosphere-biosphere system. In fact, feedbacks can be established among the various subcomponents: for instance, temperature-dependent absorption coefficients for the ocean take-up of carbon, and biospheric mass evolving with temperature, precipitation and CO_2 atmospheric levels.

ii) more detailed impact analysis of the climatologic changes predicted for the portuguese zone with GCM's can be made through the use of biospheric productivity models, yielding quantitative estimates for the modifications of the biosphere. Other aspects of the CO_2 problem as sea level rise, impact in specific agricultural species, or fisheries, must also receive attention, preferably through a sensitivity analysis in absence of reliable predictions for both long-term and seasonal meteorological and oceanic conditions under high CO_2 levels.

REFERENCES

[1] H. I. SCHIFF, A review of the carbon dioxide greenhouse problem. Plan. Space Sci., **29**, 935-950 (1981).

[2] R. J. AGUIAR, Efeitos Antropogénicos Sobre o Clima da Terra. Final-year Research Project, Lisbon University, F. C. L. (1985).

[3] R. AVENHAUS, S. FENYI and H. FRICK, Mathematical treatment of box models for the CO_2 cycle of earth. In «CO_2, Climate & Society» (1978).

[4] G. H. KHOLMAIER *et al.*, A non-linear interaction model between land biota and atmosphere. In «CO_2, Climate & Societè», J. Williams Ed., IIASA Series 1 (1978).

[5] B. C. WEARE and F. M. SNELL, A diffuse thin cloud atmospheric structure as a feedback mechanism in global climatic modelling. J. Atmos. Sci., **31**, 1725-1734 (1974).

[6] C. SAGAN and J. B. POLLACK, Anisotropic, nonconservative scattering and the clouds of Venus. J. Geophys. Res., **72**, 467-477 (1967).

[7] D. DEIRMENDJIAN, Scattering and polarization properties of water clouds and hazes in the visible and infrared. Appl. Opt., **3**, 187-196 (1964).

[8] S. TWOMEY and H. B. HOWELL, The relative merit of white and monocromathic light for the determination of visibility and backscattering measurements, Appl. Ppt., **4**, 501-506 (1965).

[9] J. T. HOLLIN, On the glacial history of Antartica, J. Glaciology **4**, 173-195 (1962).

[10] N. A. MORNER, Climatic changes during the last 35 000 years as indicated by land, sea and air data, Boreas, **2**, 34-53 (1973).

[11] C. D. RODGERS, The use of emissivity in atmospheric radiation calculations. Quart. J. R. Met. Soc. 43-54 (1966).

[12] C. D. RODGERS and C. D. WALSHAW, The computation of infrared cooling rate in planetary atmospheres, Quart. J. R. Met. Soc., **94**, 67-72 (1967).

[13] D. O. STALEY and G. M. JURICA, Flux emissivity tables for water vapour, carbon dioxide and ozone, J. Appl. Met., **11**, 241-254 (1970).

[14] T. AUGUSTSSON and V. RAMANATHAN, A radiative-convective study of the CO_2 climate problem, J. Atmos. Sci., **34**, 448-451 (1977).

[15] L. R. HOLDRIDGE, Determination of world plant formation from simple climatic data. Science, **105**, 367-368 (1947).

[16] Anuário Climatológico de Portugal, Instituto Nacional de Meteorologia e Geofísica, Lisbon, Portugal (1950 to 1975).

CONTENTS

FASCÍCULO 1-2

CONTENTS

FASCÍCULO 3-4

AUTHOR INDEX

Composição, Impressão e Acabamento
na
Imprensa Portuguesa • Rua Formosa, 108-116 • 4000 PORTO

PORTUGALIAE PHYSICA

VOL. 18 · NUMB 3/4 · 1987

CONTENTS

ISSN 0048-4903 POPYA4 18 (3/4) 99-186 (1987)

SOCIEDADE PORTUGUESA DE FÍSICA

AV. REPÚBLICA 37-4.º, 1000 LISBOA, PORTUGAL

PORTUGALIAE PHYSICA publishes articles or research notes with original results in theoretical, experimental or applied physics; invited review articles may also be included.

Manuscripts, with an abstract, may be written in English or French; they should be typewritten with two spaces and in duplicate. Figures or photographs must be presented in separate sheets and be suitable for reproduction with eventual reduction in size; captions should make the figures intelligible without reference to the text. Authors are requested to comply with the accepted codes concerning references.

There is no page charge. Author(s) will get 50 free reprints (without covers); these are to be shared among all the authors of the article. Authors interested in more reprints should say so when sending their manuscripts; quotations shall be sent with the proofs.

Subscription rates for volume 18:

3.600 Escudos (US$24) — individuals

9.000 Escudos (US$60) — libraries

PORTUGALIAE PHYSICA may also be sent on an exchange basis; we wellcome all suggestions to such effect.

All mail to be addressed to

PORTUGALIAE PHYSICA

C/O LABORATÓRIO DE FÍSICA, FACULDADE DE CIÊNCIAS
PRAÇA GOMES TEIXEIRA
4000 PORTO PORTUGAL